Shallow-water wave models and ocean-depth measurement

A thesis

Submitted to the

Tata Institute of Fundamental Research, Mumbai

for the degree of Doctor of Philosophy

in Subject Board of Mathematics

by

Manisha

International Centre for Theoretical Sciences, Bengaluru

Tata Institute of Fundamental Research

Mumbai

July, 2024

[Final Version Submitted in November, 2024]

Declaration

This thesis is a presentation of my original research work. Wherever contributions of others are involved, every effort is made to indicate this clearly, with due reference to the literature, and acknowledgment of collaborative research and discussions.

The work was done under the guidance of Professor Vishal Vasan at the Tata Institute of Fundamental Research, Mumbai.

Manisha

In my capacity as the formal supervisor of record of the candidate's thesis, I certify that the above statements are true to the best of my knowledge.

Vishal Vasan

Date: November 2024

Dedicated to my parents, Veena Goyal and Rajkumar Goyal

and my siblings Seema, Manju, Ritu, Vanita, Vipul

and my teacher Tarun Goyal

Acknowledgments

I would like to thank my advisor Prof. Vishal Vasan for his guidance, support, patience and believing in me throughout the course of my PhD journey. His expertise in the topic of this thesis is invaluable and I am truly thankful to him for introducing me to this fascinating area. I am also indebted to him for all the support he provided me during my France visit when I lost my passport. I am also thankful to Prof Vishal, Prof Amit Apte, and Prof Didier Auroux for providing me the opportunity to visit the University of Côte d'Azur for a collaboration. I would also like to thank my thesis monitoring committee Prof Vishal, Prof. Amit, (thanks for being my co-advisor as well), Prof. Vijay Krishnamurthy and Prof. Venky Krishnan for patiently listening to my talks, providing feedback and supporting me even during the difficult times. I am also thankful to Prof. Mythily for some discussions and also for listening to me patiently.

I think acknowledgement section in PhD thesis is the only time when we get to thank the people in our life officially. I have a huge list, that is difficult to start, and keep track of. My family is perhaps where I can start from. I am very lucky to be a daughter of my parents, Raj Kumar Goyal and Veena Goyal. Despite having 5 daughters and a son, my parents were not worried about their daughters' marriages, but their education and their careers, especially given the environment around them, where people don't send their daughters outside the town for education. Successfully achieving higher education and a good career by their children is what they like to brag about. My siblings, Seema, Manju, Ritu, Vanita and Vipul are beats of my heart. Their love and support, during my PhD journey, was immense. My siblings and the little ones, my nephews and niece, Aarush, Janhavi and Raghav, are the reasons for me to keep going back home and bring a lot of energy back to complete this journey.

I am grateful to my teacher Tarun Goyal, who inspired me to chase this dream. I am also thankful to Ashok sir for teaching me to look at math problems deeply. It can never be enough to thank my friends, classmates and teachers from my undergraduate college (Govt. College, Hisar) for all the fun and also building the base for my interest in mathematics. I am also thankful to some of my friends (especially Pooja Garg) for encouraging me to travel alone (which I had not done before in my life) to attend the ICTS interview. That flight, I took that day, is what I call 'my first flight': not just in terms of travelling by flight for the first time, but also because it gave me confidence, the feeling of being independent. After this is the journey (the PhD journey), which has changed my life (definitely for the better, to be clear). I am also thankful to Prof. Vanita Verma for supporting and encouraging me. I am grateful to Prof. Baljeet Singh for giving me the opportunity to work with him and giving me my first research project.

The people, I first met and hung out with, my friends Sowrabh, Mohit, Joydeep, Akhil, are the reason that it became so easy to stay away from home. So many fun

moments, long conversations, random activities, hanging out, cycling, the list goes on. My life at ICTS was also made memorable by Kusum, Sajini, Monica, Srashti, Uddeepta, Kohinoor, Jemseena, Priyanka, Arghya, Jigyasa, Sharath, Sarada, Omkar, Shashank, Pinak, Basudeb, Nachiketa, Animesh, Santhosh, Varun, Prashant, Srikanth, Soummyadip and the football gang (I sincerely apologize if I have missed out anyone). A lot of these people are very important to me, but mentioning everyone separately will just be too long. I would also like to thank Sharath for various discussions during the writing phase of this thesis and helping me in rewriting some parts of this thesis. I am also thankful to Prof. Rukmini, Prof. Rama, and Prof. Pallavi for encouraging me in my difficult times, they all are an inspiration for the female students in ICTS. I would like to thank Prof. Loga and Prof. Ajith for their advise to follow my heart and complete my PhD.

I would also like to thank Kasi for introducing me to V-labs. I am also grateful to Siddharth Khare for encouraging and supporting me. He is an inspiration to me.

I would also like to thank IISc for give me the opportunity to attend many courses in various departments. I am also grateful to Prof. Sivaram Ambikasaran for believing in me and offering me the chance to work in his research group and his teaching, working with him was fun (unfortunately, it did not work out). I am also thankful to all my friends, I made in IISc during those 2 years, Deepa, Navchetan, Vaishnavi, Ujjval, Khusboo (extremely sorry if I forgot to add someone else) for all their help and inspiration.

A special thanks to my love (and my husband now) Sowrabh, who has always encouraged and supported me throughout this journey. He has also helped me during various phases of this journey and kept me going on. Listening to him about so many different topics/stories/research and having him in my life is a blessing. I have learnt so much from him.

List of Figures

Publications relevant to the thesis

- Vishal Vasan, Manisha, and D Auroux. Ocean-depth measurement using shallow-water wave models. Studies in Applied Mathematics 147, 4 (2021), pp. 1481--1518.

Contents

Abstract

This thesis tackles the challenge of reconstructing the unseen bottom topography of ocean basins. Inspired by real-world applications, it focuses on estimating the impermeable boundary of an inviscid, incompressible, irrotational fluid within the framework of dispersive shallow-water wave models. The emphasis on shallow water is driven by prior research and the inherent difficulty of the reconstruction problem in deeper water. The proposed algorithm reconstructs both the fluid velocities and the true bottom profile, even with an inaccurate initial guess for the bottom depth. It achieves this by solving two interconnected inverse problems: one using known velocities and surface displacement to estimate the bottom, and another leveraging the observer framework to determine velocities from surface data and an approximate bottom profile. Combining the two inverse problems leads to our reconstruction algorithm. The thesis highlights the importance of model selection in the algorithm design and the accuracy of the reconstructed bottom topography.

Chapter 1

INTRODUCTION

The ocean, encompassing over 70% of Earth's surface, remains a realm of mystery. Its depth holds not only captivating beauty but also crucial information about our planet's history and its future. One key aspect of this hidden landscape is bathymetry, the shape of the ocean floor. Understanding bathymetry is critical for numerous applications, ranging from predicting the impact of tsunamis to ensuring safe submarine navigation and designing effective coastal defences. Traditionally, bathymetry data has been collected through ship-based surveys, a time-consuming and expensive process. However, water waves themselves hold the potential to reveal the secrets of the ocean floor. In this thesis, our focus is the inverse problem of detecting the bottom boundary of the ocean, given measurements of the surface displacement, and a rough estimate of the bottom profile. By addressing this inverse problem, we aim to enhance our understanding of the ocean environment and its dynamics, leading to various practical applications.

Mapping the shape of the oceanic bottom boundary is a critical aspect of oceanography research. From abyssal plains stretching for thousands of kilometres to towering seamounts, rugged canyons, and continental shelves, the underwater topography plays a critical role in shaping our planet's health [13]. This intricate dance floor of the deep sea is a key driver of ocean circulation patterns and mixing processes [41]. These, in turn, have a profound impact on global climate regulation and the rich tapestry of marine life [40]. Understanding the shape of the ocean bottom is not just a scientific problem, but one with far-reaching consequences for humanity.

Determining the exact topography of the ocean floor presents a formidable challenge for oceanographers, both theoretically and practically. While echo sounders, which rely on underwater acoustics, have been a traditional method for mapping the ocean floor [20, 55], they come with significant drawbacks. These surveys are time-consuming and expensive, requiring extensive effort and specialised equipment to cover large areas. Additionally, they can be dangerous, especially in deep waters or challenging weather conditions. More importantly, this technique has limitations in shallow continental margins, often leaving these crucial areas under-surveyed.

One promising approach utilises satellite-based gravity models [10]. These innovative methods leverage the subtle deviations in Earth's gravitational field caused by variations in ocean floor topography. The principle is simple: the additional mass of a seamount increases the local gravitational pull, causing a slight bulge in the water surface directly above [51, 52]. While these satellite-based approaches have shown promising results, particularly for large-scale features, recent studies suggest limitations. Ship-based surveys, with their higher resolution, remain more reliable for detecting sharp features, especially those with characteristic length-scales less than 25km [59]. These surveys provide crucial data for understanding complex coastal regions and other areas where high-resolution bathymetry is essential. Ship-based surveys, therefore, remain a vital tool for high-resolution bathymetry, particularly for applications like coastal management [30] and tsunami inundation prediction [45, 62]. Fluid dynamical methods also offer a way to survey large parts of the coastlines and oceans using satellite imagery.

The fluid dynamics approach models the motion of an incompressible fluid with a solid, impermeable surface as the boundary below. The increased availability and quality of satellite imagery have made these fluid dynamical methods particularly attractive for surveying vast coastal and ocean regions.

The simplest fluid-mechanical methods focus on analysing the dispersion relation of shoaling waves [50]. The dispersion relation describes the relationship between wave frequency and wavenumber, and it is influenced by water depth. By analysing variations in the dispersion relation of waves as they propagate towards the shore (shoaling), one can infer information about the underlying bathymetry (seabed shape). These methods can be further refined by incorporating nonlinear corrections to the dispersion relation [31]. Nonlinear effects become more significant for larger wave amplitudes, and including these corrections can improve the accuracy of bathymetric estimates.

A fundamental concept underlying all fluid dynamical methods for ocean depth measurement is the kinematic boundary condition at the free surface:

$$\eta_t = w - \bar{u}_s \cdot \nabla \eta,$$

where w and $\bar{u}_s$ are the vertical and horizontal velocities evaluated at the free surface η. The key point is that the free surface elevation η and the surface velocities (w and $\bar{u}_s$) are not independent quantities. They are functionally dependent on the bottom boundary profile (bathymetry) through the full equations of motion governing the fluid flow and the associated boundary conditions.

In the context of fully non-hydrostatic irrotational flow, the kinematic boundary condition may be rewritten in terms of a surface potential q:

$$\eta_t = G(\eta, \zeta) q \tag{1.1}$$

where G is the Dirichlet-Neumann operator. In simpler terms (mathematically defined in Chapter 2), it maps the tangential fluid-velocity at the free surface (horizontal movement along the surface) to the normal fluid-velocity (vertical movement into or out of the surface). Importantly, $G(\eta, \zeta)$ is directly influenced by the shape of the bottom boundary. The task of inferring the bottom boundary profile ζ from surface wave data has been explored in previous works. In [48], Nicholls and Taber attempted to estimate the operator G (and subsequently inferring ζ) using the frequencies and profiles of standing waves. Despite the inherent ill-posed nature of the problem, the authors demonstrate successful reconstruction of the bottom profile using this method. Alternatively, Fontelos et al. [29] considered that η, η_t and q are known at a specific instant in time. Under this assumption, the authors proved the existence of a unique solution for ζ satisfying equation (1.1). They further introduced a minimisation problem that allows for bottom profile recovery. However, they also acknowledge the ill-posed nature of the problem, emphasising the sensitivity of the reconstruction procedure to noise in the input data.

A fundamental aspect of ocean depth measurement lies in the defining property of the bottom boundary: the normal component of the fluid velocity vanishes at this surface (i.e., no fluid flows perpendicularly into the seabed). In simpler terms, the fluid doesn't penetrate the bottom. Building upon this principle, Vasan and Deconinck [58] employed harmonic continuation technique to derive a nonlinear, non-local equation which vanishes exactly at the true bottom boundary. This equation offered a powerful tool for bottom boundary reconstruction. However, a significant challenge arises: the dependence of this equation on the surface velocities. While satellite measurements can indeed infer both sea-surface displacements and, to some extent, sea-surface velocities, the accuracy of the latter often relies on a good estimate of the bottom boundary profile itself [16, 37]. Thus to successfully estimate the bottom boundary from surface displacement measurements, we need to determine the surface velocities simultaneously.

A complete understanding of fluid motion necessitates incorporating the fluid momentum balance equation along with equation (1.1). In the context of inviscid, irrotational, and incompressible flow, the momentum equation governs the time evolution of the surface potential q. By incorporating this equation into the analysis, Vasan and Deconinck [58] were able to deduce a system of two equations with two unknowns: the bottom boundary profile and the surface velocities. A significant advantage of this approach is the ability to reconstruct the bottom boundary based solely on surface data ($\eta(x,t)$, measurements of the surface displacement). This eliminates the need for any direct measurements (e.g., mean depth) of the bottom profile. The authors also noted the ill-posed nature of the problem. The reconstruction was shown to be more reliable in the shallow-water regime.

The Saint−Venant equations are a specific model for shallow-water waves widely used in modelling inundation of coastal regions. Upon averaging the incompressibility

condition in the vertical and taking into account the kinematic boundary condition, one obtains

$$\eta_t + \nabla \cdot ((\eta + h + \zeta)\bar{u}) = 0,$$

where $(\eta + h + \zeta)$ represents the height of the fluid column and $\bar{u}$ is the depth-averaged horizontal velocity. The authors of [38] leverage the Saint−Venant equations as a hyperbolic partial differential equation for bathymetry detection. The method of [38] involves scaling and time-averaging the equation, assuming knowledge of the mean water depth, and utilising satellite data for surface displacement and velocities. However, it requires a non-zero Coriolis parameter. This restricts its applicability in coastal regions where Coriolis effects are weak, which is a common occurrence. While existing methods primarily focus on long-scale and inviscid flow models, bathymetry detection can extend beyond these scenarios. Although the fluid dynamical models considered thus far all involved long length-scales and inviscid flow, domain identification is not limited to such scenarios. Indeed one can pose the problem in the context of creeping flows [34].

This thesis builds upon existing bathymetry reconstruction methods using fluid dynamics [29, 58]. However, we introduce a crucial difference: we frame the problem within the shallow-water regime. We derive simplified equations specifically applicable to shallow-water flows, aiming to achieve two key goals. Firstly, we investigate whether restricting the analysis to the shallow-water regime leads to more robust and well-behaved reconstructions. This includes exploring the effectiveness of reconstruction over a wide range of values for the shallowness parameter. Secondly, similar to [58], we aim to recover the bottom profile solely from surface displacement measurements η, eliminating the need for direct velocity measurements which can be challenging to obtain. Our approach diverges from shallow-water reconstruction method of [38] by focusing on dispersive shallow-water wave models. These models offer advantages in terms of mathematical properties and solution regularity. Importantly, incorporating dispersion aligns with established theoretical and experimental evidence highlighting its significance in shallow-water flows with varying bottom topography [22, 24, 32, 14].

Another distinguishing facet of our work is the adoption of observers. Observer theory provides a framework for designing mathematical constructs, called observers, that can estimate the unmeasured state of a system based on available measurements and knowledge of the system's dynamics. When partial knowledge of a system's state y is available, we can construct an observer system $\tilde{y}_t$ that closely mimics the full system $y_t = f(y)$. This observer, driven by available measurements and an internal dynamics, aims to converge to the actual state as time progresses i.e., $\tilde{y} \to y$ as $t \to \infty$. The observer design involves constructing the observer dynamics $\tilde{y}_t = \tilde{f}(\tilde{y}, Oy)$ where $\tilde{f}$ is a modification of f and O is an operator with a null-space representing the partial knowledge available of the state y. Successful convergence allows us to infer the missing state information by simu-

lating the observer problem [44, 53]. As mentioned previously, directly measuring surface velocities can be challenging or even impractical. The observer framework is popular in the geophysics community and is routinely used in data assimilation to recover the state of a dynamical system from partial or sparse measurements [5, 9, 6, 4] and motivated us to use the same for determining surface velocities for our shallow water models.

In this thesis, we have successfully accomplished the recovery of bottom profiles using surface displacement measurements $\eta(x,t)$ only. Concretely, we present an approach to detect the bottom boundary in the context of two shallow-water models. We limit ourselves to shallow-water models to reduce the ill-posed nature of the problem in the deep-water regime. We use as observations, generic time-dependent surface displacements. In principle, our work may be adapted to other shallow-water models.

Here is an outline of the key chapters in this thesis:

We begin by establishing a foundation in Chapter 2, discussing the governing equations for water-waves and the associated Hamiltonian formulation. In Chapter 3, we focus on shallow-water wave models and derive a class of bidirectional dispersive Boussinesq-type shallow-water wave models with varying bottom-boundaries. We explore two specific cases: one of which is known in the literature [36] and another which we have newly introduced in . This chapter also delves into the conservation laws associated with these models. Finally, we present analytical solutions for the linear parts of these shallow-water wave models and numerical simulations for the full nonlinear systems.

The following chapters tackle two inverse problems. In Chapter 4, we address bathymetry reconstruction, where we aim to recover the bottom profile from surface data. We introduce the reconstruction equation and showcase successful profile recovery through numerical experiments. Chapter 5 investigates velocity estimation using an observer model. Here, we employ the observer framework to determine fluid velocity based on surface displacement data, assuming a known bottom profile. We also provide numerical evidence supporting this approach.

Building upon these concepts, we combine the two inverse problems we explored earlier in Chapter 6. We present an algorithm for reconstructing the bottom profile solely from surface displacement measurements. Note that we do not need prior knowledge of mean water depth. This approach allows for bottom profile reconstruction in deeper water compared to [58], albeit remaining within the shallow-water regime. Finally, Chapter 7 summarises the key findings and methodologies developed, while also discussing potential extensions and future research directions for this work.

The main results and findings of this work appeared as a published article:

Vishal Vasan, Manisha, and D Auroux, "Ocean-depth measurement using shallow-water wave models", Studies in Applied Mathematics 147, 4 (2021), pp. 1481--1518.

Chapter 2

GENERAL BACKGROUND AND NOTATION

2.1 Governing Equation

Suppose a fluid motion is inviscid, irrotational and incompressible. Then the velocity potential, denoted by $\phi(x, y, z, t)$, satisfies the Laplace equation in the entire fluid domain. The fluid domain is bounded by the free surface displacement $\eta(x, y, t)$ and the bottom boundary profile $\zeta(x, y)$. In other words,

$$\phi_{xx} + \phi_{yy} + \phi_{zz} = 0, \quad -h - \zeta(x, y) < z < \eta(x, y, t),\ 0 < x < L,\ 0 < y < L. \tag{2.1}$$

where L is the lateral extent of the fluid and h is the typical depth. Note that we don't assume the mean of ζ to be zero. In this context, h can be regarded as an estimate for the bottom topography rather than the actual mean value of the bottom surface. We assume the domain is periodic along the horizontal directions, namely the x and y axes, with period L. The fluid velocity is given by (ϕ_x, ϕ_z). Here and throughout the thesis, subscripts will denote partial derivatives. The gradient will always refer to the gradient in the horizontal directions. Thus in 3D, $\nabla\phi = (\phi_x, \phi_y)$ whereas in 2D $\nabla\phi = \phi_x$. The boundary conditions are as follows:

1. Kinematic boundary condition: The free-surface fluid-particles are constrained to remain on the free surface, that is, the rate of displacement of the fluid surface $z = \eta(x, y, t)$ is determined by the the velocity in the direction of the local normal. Thus, we have
$$\eta_t = \phi_z - \nabla\phi \cdot \nabla\eta, \quad z = \eta(x, y, t). \tag{2.2}$$

2. Solid-wall boundary condition: The bottom boundary is fixed in time and fluid cannot penetrate through the solid boundary. This leads to the boundary condition that the velocity of the fluid at the bottom boundary $z = -h-\zeta(x, y)$ in the normal

direction vanishes:

$$\phi_z + \nabla\phi \cdot \nabla\zeta = 0, \quad z = -h - \zeta(x, y). \tag{2.3}$$

3. Bernoulli equation: The pressure on the surface is the same as the atmospheric pressure and using the conservation of momentum (in the absence of any fluid above the free surface), we get the following dynamic boundary condition on the free surface:
$$\phi_t + \frac{1}{2}\left(\phi_x^2 + \phi_y^2 + \phi_z^2\right) + g\eta = 0, \quad z = \eta(x, y, t), \tag{2.4}$$
where g is the acceleration due to gravity.

We have assumed zero surface tension in the equations described above. For the length scales we have in mind for the problems addressed in this thesis, one may safely neglect surface tension. A detailed derivation of the water wave equations (2.1-2.4) can be found in the book by Cohen and Kundu [17]. In this thesis, we only work with periodic boundary conditions, although it's worth noting that other boundary conditions, such as decay at infinity, are also possible. Subject to the derivation of appropriate models which capture the effects of inflow/outflow, the main ideas in this thesis may be generalised to different boundary conditions.

2.2 Hamiltonian Formulation

The set of water-wave equations described in the previous section can be formally regarded as a Hamiltonian system. Zakharov [64] was the first to provide a Hamiltonian formulation of the water-wave equations. This Hamiltonian structure is established entirely in terms of the surface variables, namely, $\eta(x, y, t)$, and a new variable

$$q(x, y, t) = \phi(x, y, z = \eta, t),$$

representing the velocity potential at the free surface. This approach is reasonable because, even though the entire system exhibits time dependence, the time derivatives only appear in the boundary conditions at the free surface. In other words, if at a specific time $t = t_0$, we know $\eta(x, y, t_0)$ and $q(x, y, t_0)$, then the solution in the remaining fluid domain is uniquely determined by the boundary conditions and Laplace's equation. As a result, the functions η and q are plausible conjugate variables for the Hamiltonian. The Hamiltonian for the system (equations 2.1-2.4) is given by

$$\mathcal{H} = \frac{1}{2}\int_0^L \int_0^L \left[\int_{-h-\zeta}^{\eta} \left(\phi_x^2 + \phi_y^2 + \phi_z^2\right) dz + g\eta^2\right] dy\, dx,$$

and the corresponding Hamiltonian equations are

$$\frac{\partial \eta}{\partial t} = \frac{\delta \mathcal{H}}{\delta q}, \quad \frac{\partial q}{\partial t} = -\frac{\delta \mathcal{H}}{\delta \eta}, \tag{2.5}$$

where the right-hand sides are functional derivatives of the Hamiltonian $\mathcal{H}$ with respect to the canonical variables $\eta(x, y, t)$ and $q(x, y, t)$. That is, the temporal evolution is stated in terms of these two quantities $\eta(x, y, t)$ and $q(x, y, t)$ defined on the boundary. Craig and Sulem [21] used Dirichlet-Neumann operator to write down the Hamiltonian in a simpler form which is easy to approximate. One of the first simulations of the water-wave problem to directly employ the Hamiltonian equations was also done by Craig and Sulem [21]. The Dirichlet-Neumann operator (DNO) is defined via the following boundary-value problem which specifies a function ψ uniquely.

$$\begin{aligned} \psi_{xx} + \psi_{yy} + \psi_{zz} = 0, \quad & -h - \zeta(x, y) < z < \eta(x, y, t),\ 0 < x < L, 0 < y < L, \\ \psi_z + \nabla\psi \cdot \nabla\zeta = 0, \quad & z = -h - \zeta(x, y), \\ \psi = q(x, y, t), \quad & z = \eta(x, y, t). \end{aligned}$$

The DNO $G(\eta, \zeta)$ is then defined as the map from the Dirichlet condition $q(x, y, t)$ to the associated Neumann condition at $z = \eta(x, y, t)$. Thus

$$G(\eta, \zeta)q = \psi_z - \nabla\psi \cdot \nabla\eta, \quad z = \eta(x, y, t).$$

Thus DNO maps the Dirichlet data of a harmonic function along a surface to the associated normal derivative at that same surface. With the help of Green's identity, one can express the Hamiltonian in terms of canonical variables alone [64, 21] given by

$$\mathcal{H} = \frac{1}{2}\int_0^L \int_0^L \left(qG(\eta, q)q + g\eta^2\right) dydx, \tag{2.6}$$

and the Hamiltonian equations can be written as

$$\frac{\partial \eta}{\partial t} = G(\eta, \zeta)q, \tag{2.7}$$

$$\frac{\partial q}{\partial t} = -g\eta - \frac{1}{2}|\nabla q|^2 + \frac{(\nabla q \cdot \nabla\eta + G(\eta, \zeta)q)^2}{2(1 + |\nabla\eta|^2)}. \tag{2.8}$$

The first equation can be derived either directly from the Hamiltonian or, more straightforwardly, by recognising that the right-hand side of equation (2.2) corresponds to the Dirichlet-Neumann operator's definition. The equation for the evolution of q can be obtained from equation (2.4) and the relations

$$q_x = \phi_x + \eta_x\phi_z, \quad q_y = \phi_y + \eta_y\phi_z,$$

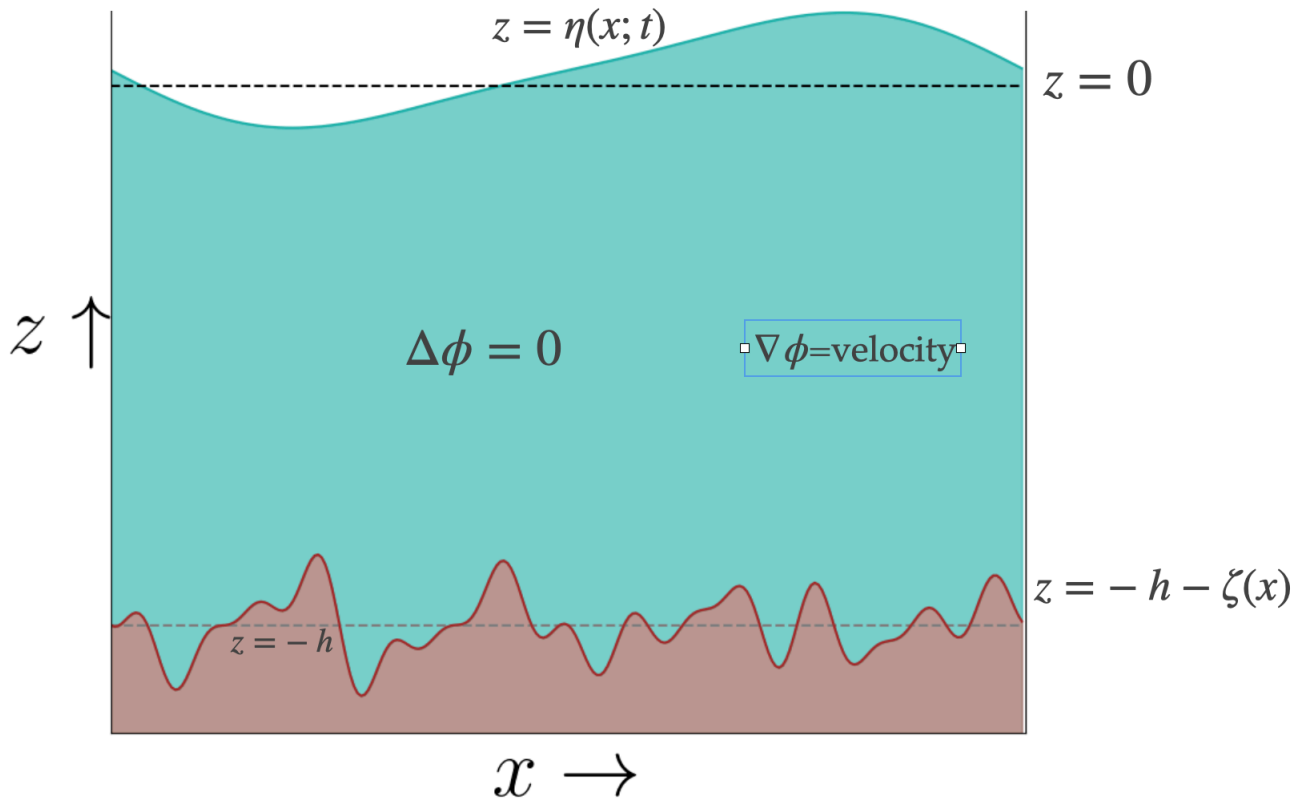

Figure 2.1: Domain in 2D for the water-wave problem

which are consequences of the definition of q and the chain rule. But for somewhat abstract nature of the Dirichlet-Neumann operator, equations (2.7-2.8) offer a seemingly straightforward set of equations for evolution of surface quantities. In equation (2.5) or equations (2.7-2.8), it is evident that the dynamically relevant quantities reside on the boundary: the shape of the free surface $\eta(x,t)$ and the value of the potential at the surface $q(x,t) = \phi(x,\eta,t)$. Note that although these equations resemble typical partial differential equations, $G(\eta,\zeta)$ is not a local operator. However, it is known that the Dirichlet-Neumann operator $G(\eta,\zeta)$ is a self-adjoint operator and analytic in both its parameter η and ζ [18, 35, 47]. Craig and Sulem [21], in their foundational work on numerical water wave simulation, present an alternative characterisation of G, expressing it as a Taylor series expansion in powers of η. Truncating this series of the Dirichlet-Neumann operator in powers of η yields an approximation to the overall operator, efficiently computable using fast Fourier transforms for problems on periodic domains [21, 33, 46]. This perspective elucidates one approach to constructing approximate models for water wave equations. Another method, which we will employ in the next chapter, involves following the technique put forward by Ablowitz et al. [1].

2.3 2D formulation and Solution to the Linear System:

In this thesis, we primarily focus on the two-dimensional system, i.e., when there is only one horizontal direction. However, it's worth noting that the methods and findings presented here can readily be extended to a three-dimensional system. Figure 2.1 is a cartoon of a two-dimensional fluid. The complete water wave model in two dimensions with periodic boundary condition (period L) along lateral dimension is expressed as follows:

$$\phi_{xx} + \phi_{zz} = 0, \qquad -h - \zeta(x) < z < \eta(x,t),\ 0 < x < L, \tag{2.9}$$

$$\phi_z + \zeta_x \phi_x = 0, \qquad z = -h - \zeta(x), \tag{2.10}$$

$$\eta_t = \phi_z - \eta_x \phi_x, \qquad z = \eta(x,t), \tag{2.11}$$

$$\phi_t + \frac{1}{2}\left(\phi_x^2 + \phi_z^2\right) + g\eta = 0, \qquad z = \eta(x,t). \tag{2.12}$$

A fundamental problem in the theory of water waves is understanding how the fluid evolves over time. Equations (2.9-2.12) are typically supplemented with initial conditions for the velocity potential ϕ and the surface elevation η at some initial time $t = t_0$, and the objective is to describe how the surface evolves over time, often referred to as the "Forward Problem". Equation (2.9) indicates that the velocity potential is a harmonic function, while the other equations specify boundary conditions at both the free surface and the bottom boundary.

The water-wave equations represent a unique combination of linear and nonlinear partial differential equations (PDEs). One of the unknowns, ϕ, satisfies a linear PDE within the bulk of the fluid. In contrast, the free surface η is governed by nonlinear evolution equations at the boundary. At each moment in time, with a given boundary η and potential ϕ at $z = \eta(x,t)$, we solve the Laplace equation, which, in turn, governs the evolution of the surface and the potential through equations (2.9-2.12).

Assuming a bottom profile $\zeta = 0$ and unidirectional wave propagation in the x-direction with wavelength L, we consider small-amplitude waves, i.e., a/L and a/h are much smaller than 1, where a represents the amplitude of the wave. Under these conditions, the water-wave equations (2.9-2.12) can be linearised, resulting in the following system:

$$\phi_{xx} + \phi_{zz} = 0, \tag{2.13}$$

$$\phi_z = 0, \quad z = -h, \tag{2.14}$$

$$\phi_z = \eta_t, \quad z = 0, \tag{2.15}$$

$$\phi_t = -g\eta, \quad z = 0. \tag{2.16}$$

Note that the last two equations are on the surface $z = 0$ because for small-amplitude waves, the terms ϕ_t and ϕ_z can be evaluated at $z = 0$ rather than at $z = \eta$ to simplify these conditions. For the details, we refer the reader to the book by Kundu and Cohen [17]. Assuming the form for $\eta(x, t)$ in terms of sinusoidal component with wavenumber k and frequency ω for which $\eta = a\cos(kx + \omega t)$, a solution to this linearised system is given by:

$$\phi = \frac{a\omega}{k}\frac{\cosh\left(k(z+h)\right)}{\sinh(kh)}\sin(kx + \omega t) \text{ for each } k = \frac{2n\pi}{L}, n = 0, 1, 2, \ldots. \tag{2.17}$$

Here, the dispersion relation is expressed as:

$$\omega(k) = \sqrt{gk\tanh(kh)}. \tag{2.18}$$

We refer the reader to the book by Kundu and Cohen [17] for the above solution of the linear equations and the dispersion relation. Also, for a discussion on the governing equations of water-waves, their derivation, the different types of approximations and the solutions associated with approximate models, we refer the reader to [2, 17, 23, 37, 43]. It's important to note that general explicit closed-form solutions for this nonlinear, free-boundary value problem do not exist. Nevertheless, equations (2.9-2.12) are known to possess unique solutions that depend continuously on the initial data, as shown by Lannes [42] and Wu [60].

Chapter 3

SHALLOW WATER WAVE MODELS

In this thesis, our primary focus centres on solving the inverse problem of discerning the ocean's bottom boundary. This involves utilising measurements of surface displacement and an initial estimate of the bottom profile. By delving into this inverse problem, our objective is to deepen our comprehension of the oceanic environment and its dynamics, offering insights into various practical applications. Our methodology aligns closely with the approaches presented in the works of [58, 29], but we distinguish our work by looking into shallow-water regime from the outset. Specifically we derive the shallow-water analogue of the equations in [58, 29]. Now, let's explore the reasons behind choosing shallow-water modelling.

3.1 Causes of Ill-posedness

As noted in Vasan and Deconinck [58], the choice of the shallow-water model stems from the inherent ill-posed nature of the problem, primarily attributed to two factors: 1) Deep water conditions (characterised by a large ratio of depth, h, to wavelength, L), and 2) Still water conditions (zero surface displacement and surface velocities).

Let's look into the first reason: Solving the inverse problem of deducing the ocean floor from surface wave measurements encounters a significant obstacle due to the rapid decrease in the velocity field with depth. As an example, consider the linear model equations (2.13-2.16) with a flat bottom boundary at $z = -h$. By differentiating the solution given in equation (2.17), we get

$$\phi_z(x, z = -h) = 0, \quad \phi_x(x, z = -h) = \frac{a\omega \cos(kx + \omega t)}{\sinh(kh)}.$$

Note that ϕ_x decreases uniformly to zero as the depth h becomes larger. Thus there is an exponential drop in the vertical direction in the gradient of velocity potential. Now, when we aim to determine the ocean floor, which is essentially where the fluid velocity

becomes zero, there's a computational challenge. For a sufficiently deep fluid-flow, there is a depth h_0 and a number ϵ such that for all depths below h_0, the magnitude of the fluid velocity is smaller than ϵ. As the depth of the fluid is made larger, ϵ can be taken smaller. As a consequence, by considering sufficiently deep water, the change in the surface velocities due to a change in the bottom boundary, is arbitrarily small. This implies the inverse problem of bathymetry detection is ill-posed in the sense that the reconstruction of the bottom profile is highly sensitive to the surface velocities. This ill-posedness was recognised by Fontelos et al. [29] and Vasan and Deconinck [58]. Both suggested that the reconstruction was more stable in shallower water. Note that this ill-posedness is essentially the same that is associated with the Cauchy problem for the Laplace equation. The Laplace equation in non-dimensional form is

$$\mu^2\phi_{xx} + \phi_{zz} = 0,$$

where $\mu = h/L$ is the aspect ratio defined in terms of a typical depth h and the horizontal period L. In the shallow-water regime where $\mu \ll 1$, we see that the vertical derivatives of ϕ (and hence the vertical velocities) do not vary much from their free surface value. This motivates us to look for water-wave models in the shallow-water regime rather than try to work with the full water-wave equation.

Note that the shallow-water assumption does not remove the cause of ill-posedness due to still water. Let's look into this reason: Still water can conform to any bottom surface. Intuitively, a quiescent water body, in equilibrium, adopts the shape of its container or the confined bottom profile. [58] explicitly demonstrated the lack of uniqueness in inferring the bottom profile when surface displacement is zero. Figure 3.1 from [58] presents bottom profile reconstruction using localised free-surfaces, revealing better recovery in regions with non-negligible free-surface displacement and poorer in the region where free-surface displacement is close to zero. Figure 3.1 illustrates three positions of localised surface displacement. The left column showcases the free surface (bold solid line), reconstructed bottom surface (dashed line with dots), and true bottom surface (thin solid line). The right column compares computed tangential velocity (dots) with true tangential velocity (solid line). The right column of Figure 3.1 distinctly illustrates negligible velocities away from the localised disturbance and on the left column, it's obvious that the recovery is much better in places where the surface is noticeably disturbed and gets worse as you move away. So, in this thesis, we'll assume that both the surface disturbance η and the surface velocity η_t do not vanish identically in any open region of space or open interval of time.

The problem of small surface velocities remains an issue despite shallow-water modelling assumption. The way in which it arises in our work is discussed in Chapter 4 and motivates the need for a regularisation scheme (also discussed in Chapter 4).

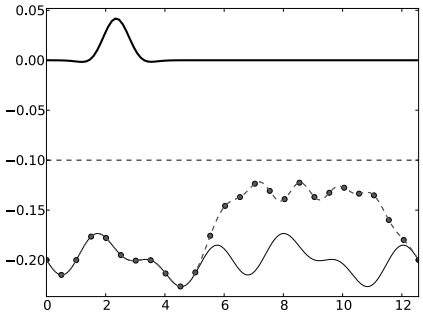

(a) True (thin solid line) and computed (dots) bottom surface.

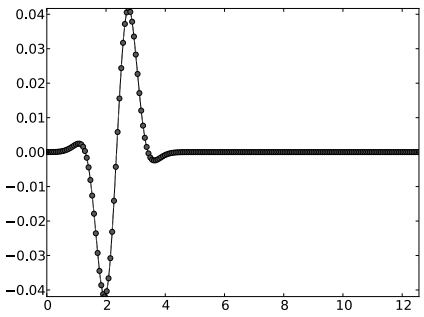

(b) True and computed tangential velocity at surface.

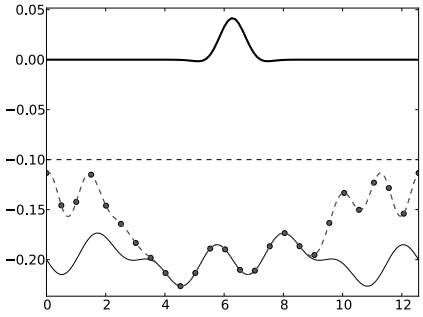

(c) True (thin solid line) and computed (dots) bottom surface.

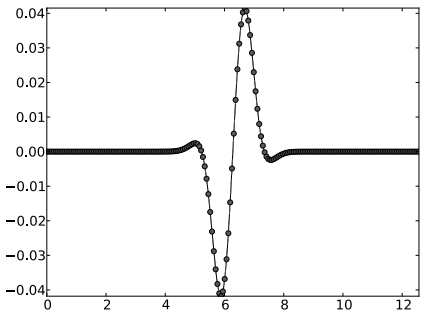

(d) True and computed tangential velocity at surface.

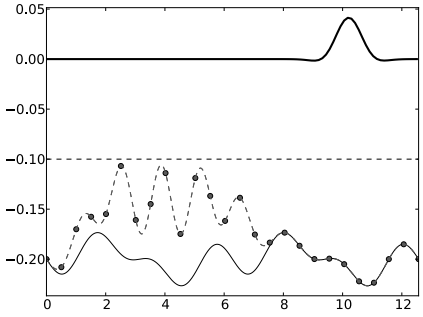

(e) True (thin solid line) and computed (dots) bottom surface.

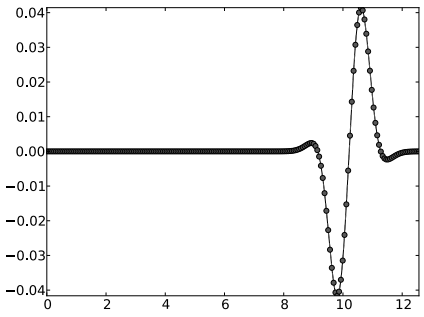

(f) True and computed tangential velocity at surface.

Figure 3.1: Figure taken from Vasan and Deconinck [58]: Recovering the bottom surface using localised surface displacements. Each row presents a reconstruction based on a different localised surface elevation profile (bold solid line in the left column). The left column shows true and computed bottom surfaces and the right column depicts the computed tangential velocity at the surface.

We will further assume that the free surface is consistently well-separated from the bottom boundary. Specifically, we assert that the bottom boundary does not breach the free-surface, expressed as $\eta(x,t) > -h - \zeta(x)$ for all time t. This criterion is sometimes referred as the non-cavitation or no-island condition. Lannes [42] also uses similar condition in proving the well-posedness of the water-wave equations. Vasan and Deconinck [58] and Fontelos et al. [29] needed a similar condition for their formulation to reconstruct the bottom boundary.

3.2 Derivation of Models

When considering approximations, our initial tools often involve Taylor expansions or perturbation theory. Numerous models, such as KdV-type equations, nonlinear Schrödinger models, KP equations, Boussinesq-type equations, among others, have been derived in [2] from Euler's water wave equations by employing Taylor expansions of the velocity potential and free-surface, assuming small amplitudes in different asymptotic regimes. From the Hamiltonian formulation of the water wave equations, it becomes evident that, for any approximation, the focus should be on approximating the Dirichlet–Neumann operator $G(\eta,\zeta)$, as the complexity lies primarily in $G(\eta,\zeta)$. Utilising the fact that DNO is an analytic function of η, proven by [19], a convergent Taylor expansion of $G(\eta)$ is employed in [21] to obtain different orders of approximation for the DNO. In [42], several shallow water asymptotic models are derived using different orders of approximations of the DNO.

In this work, we follow [1] to derive a non-local formulation for a varying bottom (where "varying bottom" implies a dependence on x, not t). Let $\phi(x,z)$ be the solution of the Laplace equation (2.9), and $\psi^{\pm}(x,z) = \exp(ikx \pm kz)$. Note, $\psi^{\pm}$ are particular solutions to the Laplace equation for all $k \in \mathbb{C}$. Subsequently, using Green's identity,

$$\int_D \phi \Delta \psi^{\pm} = -\int_D \nabla\phi \cdot \nabla\psi^{\pm} + \int_{\partial D} \phi \frac{\partial \psi^{\pm}}{\partial n},$$

and

$$\int_D \psi^{\pm} \Delta \phi = -\int_D \nabla\psi^{\pm} \cdot \nabla\phi + \int_{\partial D} \psi^{\pm} \frac{\partial \phi}{\partial n},$$

where $D = \{(x,z) : -h - \zeta(x) < z < \eta(x,t),\ 0 < x < L\}$ is the domain and n represents the outward unit normal of the surface element ∂D.

Subtracting the first equation from the second yields:

$$\int_{\partial D} \psi^{\pm} \frac{\partial \phi}{\partial n} - \int_{\partial D} \phi \frac{\partial \psi^{\pm}}{\partial n} = 0.$$

Assuming periodicity of ϕ and ψ in x-direction with period L, choosing $k = 2\pi n/L$ where

$n \in \mathbb{Z} \setminus \{0\}$, and noting that ∂D is a boundary with four sides where two sides are along the horizontal direction at $z = \eta$ and $z = -h - \zeta$ and the other two sides are along vertical direction at $x = 0$ and $x = L$, we need to compute the integration along all four sides. However, it's crucial to recognise that integrations along the vertical lines will have identical values but with different signs, leading them to cancel each other out. As a result, we are left with integration with respect to x only along horizontal direction, simplifying the above expression to

$$\int_0^L \left(\psi^{\pm}\frac{\partial \phi}{\partial n} - \phi\frac{\partial \psi^{\pm}}{\partial n}\right)\Big|_{z=\eta} \mathrm{d}x + \int_0^L \left(\psi^{\pm}\frac{\partial \phi}{\partial n} - \phi\frac{\partial \psi^{\pm}}{\partial n}\right)\Big|_{z=-h-\zeta} \mathrm{d}x = 0.$$

Let's denote n_η and d_η as the Neumann and Dirichlet conditions at the top surface $z = \eta$ and n_ζ and d_ζ as the Neumann and Dirichlet conditions at the bottom $z = -h-\zeta$. Then, the above equation can be expressed as

$$\int_0^L \left(\psi^{\pm} n_\eta - d_\eta\frac{\partial \psi^{\pm}}{\partial n}\right)\Big|_{z=\eta} \mathrm{d}x + \int_0^L \left(\psi^{\pm} n_\zeta - d_\zeta\frac{\partial \psi^{\pm}}{\partial n}\right)\Big|_{z=-h-\zeta} \mathrm{d}x = 0. \tag{3.1}$$

The directional derivative of $\psi^{\pm}$ along the normal direction can be computed by dot product between the gradient and the normal vector. Thus, we can express it as

$$\frac{\partial \psi^{\pm}}{\partial n}\Big|_{z=\eta} = (ik\psi^{\pm}, \pm k\psi^{\pm}) \cdot (-\eta_x, 1) = (-ik\eta_x \pm k)\psi^{\pm} = \mp i\partial_x\left(\psi^{\pm}\left(z = \eta\right)\right).$$

Similarly, normal component of $\psi^{\pm}$ at the bottom surface is given by

$$\frac{\partial \psi^{\pm}}{\partial n}\Big|_{z=-h-\zeta} = (ik\psi^{\pm}, \pm k\psi^{\pm}) \cdot (-\zeta_x, -1) = (-ik\zeta_x \mp k)\psi^{\pm} = \pm i\partial_x\left(\psi^{\pm}\left(z = -h-\zeta\right)\right).$$

Using these expression for normal derivatives, equation (3.1) can be written as

$$\int_0^L \left(\psi^{\pm} n_\eta \pm i d_\eta \partial_x \psi^{\pm}\right)\Big|_{z=\eta} \mathrm{d}x + \int_0^L \left(\psi^{\pm} n_\zeta \mp i d_\zeta \partial_x \psi^{\pm}\right)\Big|_{z=-h-\zeta} \mathrm{d}x = 0.$$

Integrating by parts, we obtain

$$\int_0^L \left(\psi^{\pm} n_\eta \mp i\partial_x\left(d_\eta\right)\psi^{\pm}\right)\Big|_{z=\eta} \mathrm{d}x + \int_0^L \left(\psi^{\pm} n_\zeta \pm i\partial_x\left(d_\zeta\right)\psi^{\pm}\right)\Big|_{z=-h-\zeta} \mathrm{d}x = 0.$$

Writing separate equations for ψ^+ and ψ^- and substituting their values, the above equation can be expressed as

$$\int_0^L \left\{e^{ikx+k\eta}\left(n_\eta - i\partial_x\left(d_\eta\right)\right) + e^{ikx+k(-h-\zeta)}\left(n_\zeta + i\partial_x\left(d_\zeta\right)\right)\right\} \mathrm{d}x = 0,$$

and

$$\int_0^L \left\{e^{ikx-k\eta}\left(n_\eta + i\partial_x\left(d_\eta\right)\right) + e^{ikx-k(-h-\zeta)}\left(n_\zeta - i\partial_x\left(d_\zeta\right)\right)\right\}\mathrm{d}x = 0.$$

Factoring out the constant $\exp(-kh)$ and then taking the complex conjugate of these equations, we obtain

$$\int_0^L \left\{e^{-ikx+k(\eta+h)}\left(n_\eta + i\partial_x\left(d_\eta\right)\right) + e^{-ikx-k\zeta}\left(n_\zeta - i\partial_x\left(d_\zeta\right)\right)\right\}\mathrm{d}x = 0,$$

$$\int_0^L \left\{e^{-ikx-k(\eta+h)}\left(n_\eta - i\partial_x\left(d_\eta\right)\right) + e^{-ikx+k\zeta}\left(n_\zeta + i\partial_x\left(d_\zeta\right)\right)\right\}\mathrm{d}x = 0.$$

Adding and subtracting these two equations, we get

$$\int_0^L \Big[e^{-ikx}\left\{n_\eta \cosh\left(k(\eta+h)\right) + i\partial_x(d_\eta)\sinh\left(k(\eta+h)\right)\right\} + e^{-ikx}\left\{n_\zeta\cosh\left(k\zeta\right) + i\partial_x(d_\zeta)\sinh\left(k\zeta\right)\right\}\Big]\mathrm{d}x = 0, \tag{3.2}$$

$$\int_0^L \Big[e^{-ikx}\left\{n_\eta \sinh\left(k(\eta+h)\right) + i\partial_x(d_\eta)\cosh\left(k(\eta+h)\right)\right\} + e^{-ikx}\left\{-n_\zeta\sinh\left(k\zeta\right) - i\partial_x(d_\zeta)\cosh\left(k\zeta\right)\right\}\Big]\mathrm{d}x = 0. \tag{3.3}$$

In the preceding steps, we introduced terms such as $\sinh\left(k(\eta+h)\right)$ and $\cosh\left(k(\eta+h)\right)$ into our equations, offering enhanced clarity and allowing for the truncation of their Taylor series expansions when considering the shallow-water limit. Recalling that Dirichlet conditions and Neumann conditions at the top and bottom can be expressed as $d_\eta = \phi\left(x,\eta,t\right) = q(x,t)$, $n_\zeta = 0$, and $n_\eta = G(\eta,\zeta)q$, let's define the velocity tangential to the fluid domain at the bottom $z = -h-\zeta$ as Q_x. Consequently, $\partial_x(d_\zeta) = Q_x = \phi_x - \zeta_x\phi_z$. Substituting these expressions into equations (3.2) and (3.3), we obtain the following simplified equations:

$$\int_0^L e^{-ikx}\left\{\cosh\left(k(\eta+h)\right)G(\eta,\zeta)q + iq_x\sinh\left(k(\eta+h)\right) + iQ_x\sinh\left(k\zeta\right)\right\}\mathrm{d}x = 0, \tag{3.4}$$

and

$$\int_0^L e^{-ikx}\left\{\sinh\left(k(\eta+h)\right)G(\eta,\zeta)q + iq_x\cosh\left(k(\eta+h)\right) - iQ_x\cosh\left(k\zeta\right)\right\}\mathrm{d}x = 0. \tag{3.5}$$

These two equations, known as global relations, can be simultaneously solved for both $G(\eta,\zeta)q$ and Q_x when q_x is provided. The above global relations are also obtained in [1]. Importantly, we don't assume the mean of ζ to be zero. In this context, h can be regarded as an estimate for the bottom topography rather than the actual mean value of

the bottom surface.

Within the shallow-water regime, characterised by a small depth relative to the water wavelength i.e., the aspect ratio $\mu = h/L$ is considered a small parameter. Also, we will consider small amplitude waves only. Specifically, the ratio of infinity norm of the free-surface to the depth and the ratio of infinity norm of the bottom profile to the depth ($\|\eta\|_\infty/h$ and $\|\zeta\|_\infty/h$) is small and close to each other, let us denote it by ϵ. We assume a KdV balance, $\epsilon \sim \mu^2$ [2]. This implies that both

$$\frac{\|\eta\|_\infty}{h}, \frac{\|\zeta\|_\infty}{h} \sim \left(\frac{h}{L}\right)^2. \tag{3.6}$$

In this setting, we obtain an $\mathcal{O}(\mu^4)$ accurate expansion for hyperbolic functions as follows:

$$\cosh(k(\eta+h)) = \cosh(\mu\tilde{k}(\epsilon\tilde{\eta}+1)) = 1 + \frac{(\mu\tilde{k})^2}{2} + \cdots = 1 + \frac{(kh)^2}{2} + \cdots, \tag{3.7}$$

$$\sinh(k(\eta+h)) = \sinh(\mu\tilde{k}(\epsilon\tilde{\eta}+1)) = \mu\tilde{k} + \mu\epsilon\tilde{k}\tilde{\eta} + \frac{\left(\mu\tilde{k}\right)^3}{6} + \cdots = kh + k\eta + \frac{k^3h^3}{6} + \cdots, \tag{3.8}$$

$$\cosh(k\zeta) = \cosh\left(\epsilon\mu\tilde{k}\tilde{\zeta}\right) = 1 + \cdots, \tag{3.9}$$

$$\sinh(k\zeta) = \sinh\left(\epsilon\mu\tilde{k}\tilde{\zeta}\right) = \epsilon\mu\tilde{k}\tilde{\zeta} + \cdots = k\zeta + \cdots, \tag{3.10}$$

where $\tilde{\eta} = \eta/\|\eta\|_\infty$, $\tilde{\zeta} = \zeta/\|\zeta\|_\infty$ and $\tilde{k} = kL$ are introduced solely for the expansion of hyperbolic trigonometric functions. This representation makes it evident that all higher-order terms in the expansions are of $\mathcal{O}(\mu^4)$. Using these expansions, the truncated forms of the global relations in equations (3.4) and (3.5) become

$$\int_0^L e^{-ikx}\left\{\left(1+\frac{(kh)^2}{2}\right)G(\eta,\zeta)q + iq_x\left(kh+k\eta+\frac{k^3h^3}{6}\right) + iQ_x\,(k\zeta)\right\}\mathrm{d}x = \text{h.o.t.'s}, \tag{3.11}$$

$$\int_0^L e^{-ikx}\left\{\left(kh+k\eta+\frac{k^3h^3}{6}\right)G(\eta,\zeta)q + iq_x\left(1+\frac{(kh)^2}{2}\right) - iQ_x\right\}\mathrm{d}x = \text{h.o.t.'s}, \tag{3.12}$$

where h.o.t.'s is short form for higher order terms. The higher order terms in equations (3.11) and (3.12) are of $\mathcal{O}(\mu^4)$ and higher. From equation (3.6), it follows that the term $k\zeta$ (multiplied with Q_x) in the last part of equation (3.11) is of $\mathcal{O}(\mu^3)$, therefore to derive a DNO expression to $\mathcal{O}(\mu^4)$, we must obtain an expression for Q_x accurate $\mathcal{O}(1)$ only. Considering equation (3.12) at $\mathcal{O}(1)$ order, we have: $\int_0^L e^{-ikx}(q_x - Q_x)\,\mathrm{d}x = 0$ leading to $Q_x = q_x$. This represents the expression for the tangential velocity of the fluid at the

bottom in our shallow-water approximation. Then, equation (3.11) yields:

$$\int_0^L e^{-ikx}\left\{\left(1+\frac{(kh)^2}{2}\right)G(\eta,\zeta)q+iq_x\left(kh+k\eta+\frac{k^3h^3}{6}\right)+iq_x\left(k\zeta\right)\right\}\mathrm{d}x=\text{h.o.t.'s.} \tag{3.13}$$

To express the DNO, we can rearrange this equation by placing the DNO term on the left-hand side and moving all other terms to the right-hand side:

$$\int_0^L e^{-ikx}\left(1+\frac{(kh)^2}{2}\right)G(\eta,\zeta)q\,\mathrm{d}x=\int_0^L e^{-ikx}\left\{-iq_x\left(kh+k\eta+\frac{k^3h^3}{6}\right)-iq_x\left(k\zeta\right)\right\}\mathrm{d}x, \tag{3.14}$$

and returning from Fourier space to physical space (with $k\to -i\partial_x$), we obtain the subsequent expression for a model Dirichlet-Neumann operator (DNO) with a variable bottom boundary:

$$\left(1-\frac{h^2}{2}\partial_x^2\right)G^M(\eta,\zeta)q=-hq_{xx}+\frac{h^3}{6}q_{xxxx}-\partial_x[(\eta+\zeta)q_x]. \tag{3.15}$$

We remind the reader that all functions of x are considered periodic with period 2π. Solving for G^M explicitly, we have

$$G^M(\eta,\zeta)q=-\left(1-\frac{h^2}{2}\partial_x^2\right)^{-1}\left(h-\frac{h^3}{6}\partial_x^2\right)q_{xx}-\left(1-\frac{h^2}{2}\partial_x^2\right)^{-1}\partial_x[(\eta+\zeta)q_x]. \tag{3.16}$$

As mentioned in Section 2.2, DNO for the water-wave model is self-adjoint. However the modelled DNO $G^M(\eta,\zeta)q$ provided above lacks self-adjointness. The primary reason is the last term on the right-hand side. This issue can be addressed by considering the following modified DNO:

$$G^M(\eta,\zeta)q=-\left(1-\frac{h^2}{2}\partial_x^2\right)^{-1}\left(h-\frac{h^3}{6}\partial_x^2\right)q_{xx}-\left(1-\frac{h^2}{2}\partial_x^2\right)^{-1}\partial_x\left[(\eta+\zeta)\left(1-\frac{h^2}{2}\partial_x^2\right)^{-1}q_x\right]. \tag{3.17}$$

The above modification has the same formal level of accuracy as the expression in equation (3.16). Replacing the DNO in the Hamiltonian in equation (2.6) by G^M leads to the following model equations (which are also evidently Hamiltonian):

$$\eta_t=\frac{\delta H^M}{\delta q}\qquad\Longrightarrow\ \eta_t=-\left(1-\frac{h^2}{2}\partial_x^2\right)^{-1}\left[\left(h-\frac{h^3}{6}\partial_x^2\right)q_{xx}-\partial_x\left((\eta+\zeta)\left(1-\frac{h^2}{2}\partial_x^2\right)^{-1}q_x\right)\right], \tag{3.18}$$

$$q_t=-\frac{\delta H^M}{\delta \eta}\qquad\Longrightarrow\ q_t=-g\eta-\frac{1}{2}\left(\left(1-\frac{h^2}{2}\partial_x^2\right)^{-1}q_x\right)^2. \tag{3.19}$$

Corresponding Hamiltonian $\mathcal{H}^M$ for this model is given by

$$\mathcal{H}^M = \frac{1}{2}\int \left(qG^M\left(\eta,\zeta\right)q + g\eta^2\right)\mathrm{d}x, \tag{3.20}$$

where G^M is defined in equation (3.17).

During the derivation of this model, it becomes apparent that numerous models with equivalent accuracy levels exist. For instance, the operator $\left(1-h^2\partial_x^2/2\right)^{-1}$ in right-hand side of equation (3.16) is asymptotically interchangeable with and can be replaced by 1 up to the level of accuracy we are considering. Note that the first term in equation (3.16) contains lower-order terms and higher order terms. This means when we replace $\left(1-h^2\partial_x^2/2\right)^{-1}$ by its expansion we should retain the appropriate terms. In this scenario, we arrive at a different model equation:

$$\eta_t = -\left(h+\frac{h^3}{3}\partial_x^2\right)q_{xx} - \partial_x\left((\eta+\zeta)q_x\right), \tag{3.21}$$

$$q_t = -g\eta - \frac{1}{2}q_x^2. \tag{3.22}$$

A question arises: why did we not opt for this seemingly simpler model compared to model equations (3.18-3.19)? To address this question, let's apply the ansatz $(\eta, q) \approx (A, B)e^{ikx-i\omega t}$ to the linear constant coefficient problem of this model. The resulting dispersion relation is $\omega^2 = ghk^2\left(1-h^2k^2/3\right)$. Consequently, for large kh, exponential growing solutions emerge. Thus, the model equation (3.21) is not linearly stable and leads to ill-posed forward model. For this reason, we discard this model and choose to work with the model provided in equations (3.18) and (3.19), where better analytic properties for the forward problem are observed. The dispersion relation for the equations (3.18-3.19) is given by

$$\omega = \sqrt{ghk^2\left(\frac{1+h^2k^2/6}{1+h^2k^2/2}\right)}. \tag{3.23}$$

Comparing it with the dispersion relation in equation (2.18) of full water-wave model, we can see that the large kh behaviour of equation (3.23) is like the small kh behaviour of equation (2.18), which reflects our choice to work in the shallow-water regime.

Another illustration of a model with the same level of asymptotic accuracy is when the operator $\left(1-h^2\partial_x^2/2\right)^{-1}$ in the right-hand side of equation (3.16) is replaced by 1 only in the last term. This substitution results in the following self-adjoint DNO:

$$G^M(\eta,\zeta)q = -\left(1-\frac{h^2}{2}\partial_x^2\right)^{-1}\left(h-\frac{h^3}{6}\partial_x^2\right)q_{xx} - \partial_x[(\eta+\zeta)q_x]. \tag{3.24}$$

By following this approach, the resulting Hamiltonian equations align with the Boussinesq-type equation derived by [1], with the distinction of incorporating a non-trivial bottom

boundary. We choose equation (3.17) over this alternative, as the model equations (3.18-3.19) represent a regularised version of the Boussinesq-type equations obtained from equation (3.24). This regularisation is introduced by the operator $(1 - h^2\partial_x^2/2)^{-1}$ multiplied in the nonlinear term in equation (3.17). Notably, this convolution operator smoothens out the function. For a detailed mathematical explanation, refer to Section 4.1 where we have shown that this operator maps $L^2[0, 2\pi]$ functions to at-least $H^1[0, 2\pi]$ functions.

Non-dimensionalised form:

The horizontal span in our domain has been $[0, L]$ so far. Let's employ a horizontal length scale of $L/2\pi$, ensuring that our Fourier modes k (wave numbers) become integers for simplicity. Utilising the following scaling:

$$(\eta, \zeta) \to h(\tilde{\eta}, \tilde{\zeta}), \quad q_x \to \sqrt{gh}\tilde{q}_x, \quad t \to \frac{L}{2\pi}\frac{1}{\sqrt{gh}}\tilde{t},$$

and removing the tilde in the new equations for the sake of simplicity in notation, equations (3.18-3.19) appear as:

$$\eta_t = \omega^2(-i\partial_x)q - \mathcal{P}(-i\partial_x)\partial_x\left[(\eta + \zeta)\mathcal{P}(-i\partial_x)q_x\right], \tag{3.25}$$

$$q_t = -\eta - \frac{1}{2}\left(\mathcal{P}(-i\partial_x)q_x\right)^2, \tag{3.26}$$

where we have defined the operator $\omega^2(-i\partial_x)$ and $\mathcal{P}(-i\partial_x)$ using their Fourier transforms, along with the parameter μ as follows:

$$\omega^2(k) = \frac{1 + \frac{(\mu k)^2}{6}}{1 + \frac{(\mu k)^2}{2}}k^2, \quad \mathcal{P}(k) = \frac{1}{1 + \frac{(\mu k)^2}{2}}, \quad \mu = \frac{2\pi h}{L}. \tag{3.27}$$

The only non-dimensionalised parameter in this form is the aspect ratio μ. The equations examined in [15] can be seen as a generalised version of equations (3.25-3.26), incorporating a boundary operator in place of bottom-profile ζ. In other words, the shallow-water wave equations presented here can also be considered as shallow-water approximations to the boundary operator employed in [15]. The Hamiltonian corresponding to equations (3.25-3.26) and DNO in terms of these operator are as follows:

$$\mathcal{H}^{\omega,\mathcal{P}} = \frac{1}{2}\int_0^{2\pi}\left(q\omega^2(-i\partial_x)q + \eta^2 + (\eta + \zeta)\left(\mathcal{P}q_x\right)^2\right)dx, \tag{3.28}$$

$$G^M(\eta, \zeta)q = \omega^2(-i\partial_x)q - \mathcal{P}(-i\partial_x)\partial_x\left[(\eta + \zeta)\mathcal{P}(-i\partial_x)q_x\right]. \tag{3.29}$$

Note that we use the symbols $\omega^2(-i\partial_x)$ and $\mathcal{P}(-i\partial_x)$ when these pseudo-differential operators act on functions of the real variable x, and $\omega^2(k)$ and $\mathcal{P}(k)$ for their Fourier transforms (Fourier multiplier), respectively. Most of the time, we will omit the arguments

of ω^2 and $\mathcal{P}$ to simplify our notations. It's important to recognise that we interpret them as operators when acting on functions of the real variable x and as Fourier multipliers when acting on the Fourier transforms of functions.

As discussed earlier, there are various models that can be derived here. For instance, by making a substitution $\omega^2 = k^2 + \mathcal{O}(\mu^2)$ and $\mathcal{P} = 1 + \mathcal{O}(\mu^2)$ we arrive at an alternative Hamiltonian which gives the hydrostatic shallow-water equations in one horizontal dimension. Different choices for the pseudo-differential operators ω^2 and $\mathcal{P}$ can lead to the non-trivial bottom boundary versions of the ASMP model [3] or a Hamiltonian version of the Hur-Pandey model [36]. All these models represent different types of bidirectional Whitham equations. For a comparative analysis of such models, we refer to [26].

While looking at the literature to see if the model in equation (3.27) has been derived before, we came across another model which is close to our model given by Hur and Pandey [36]. Writing the Hamiltonian version of their model, we see that it follows the same Hamiltonian as in equation (3.28) with Hamiltonian equations (3.25-3.26) with the choices of the operator given by

$$\omega^2(k) = k\frac{\tanh(\mu k)}{\mu}, \quad \mathcal{P}(k) = \frac{\tanh(\mu k)}{\mu k}, \quad \mu = \frac{2\pi h}{L}, \tag{3.30}$$

which we refer as regularised Boussinesq−Whitham model.

In this thesis, we will work with these two models given by equations (3.27) and (3.30), we will call the former as regularised Boussinesq model and the latter one as regularised Boussinesq−Whitham model. Here, we will write these models in the table format for comparison and a quick look. The model equations are:

$$\begin{aligned} \eta_t &= \omega^2 q - \mathcal{P}\partial_x\left((\eta+\zeta)\mathcal{P}q_x\right), \\ q_t &= -\eta - \frac{1}{2}\left(\mathcal{P}q_x\right)^2. \end{aligned}$$

The pseudo-differential operators for the two models are given by

Regularised Boussinesq Model	Regularised Boussinesq−Whitham Model
$\omega^2(k) = \dfrac{1+\frac{(\mu k)^2}{6}}{1+\frac{(\mu k)^2}{2}}k^2, \quad \mathcal{P}(k) = \dfrac{1}{1+\frac{(\mu k)^2}{2}}$	$\omega^2(k) = k\dfrac{\tanh(\mu k)}{\mu}, \quad \mathcal{P}(k) = \dfrac{\tanh(\mu k)}{\mu k}$

The regularised Boussinesq−Whitham equations with trivial bottom boundary was considered in [25] where they showed local and global wellposedness. Their equations are slightly different from those given here. Indeed their equations are written in terms of a new velocity variable. It suffices for our purposes, and makes our computer code more modular, to consider equations in terms of velocity potential since only ω and $\mathcal{P}$ need to be defined. Both regularised Boussinesq and regularised Boussinesq−Whitham have equations where the nonlinearity is a bounded operator (on some suitable function space

such as $L^2([0,2\pi]) \times L^2([0,2\pi]))$. Indeed regularised Boussinesq has a smoothing nonlinearity. For this reason we expect regularised Boussinesq to possess a local wellposedness theory for sufficiently smooth initial data.

3.3 Conservation Laws for Shallow Water Models

While not directly related to bathymetry detection, conserved quantities offer valuable insights into water wave dynamics and can be used for numerical validation tests. The full water-wave equations (2.1-2.4) possess several conserved quantities, as demonstrated by Olver [49] and Benjamin and Olver [11]. These quantities provide benchmarks for the accuracy of water wave models. This section delves into conserved quantities within the context of our work. In contrast to the works [11, 49], we connect properties of the DNO (or model DNO) to these conserved quantities. A function T is called a conserved density and $\int T$ is called conserved quantity if

$$\frac{d}{dt}\int_0^L T dx = 0.$$

Olver [49] established that the 2D water wave problem with infinite depth and surface tension possesses eight independent conservation laws. Here, we will explore a few of these for a general Hamiltonian system of the form:

$$\mathcal{H} = \frac{1}{2}\int \left(qG\left(\eta,\zeta\right)q + g\eta^2\right) \mathrm{d}x.$$

We will subsequently derive the conditions on the operator $G(\eta,\zeta)$ under which specific conservation laws from Olver's work [49] hold true for the system of equations (3.25-3.26).

For the 2D water wave problem with a finite bottom and no surface tension, Benjamin and Olver [11] demonstrated that only two quantities are conserved: energy and mass. We will show at the end of this section that these two conserved quantities are indeed conserved by both regularised Boussinesq model (3.27) and regularised Boussinesq−Whitham model (3.30).

In Hamiltonian systems, the time evolution of a functional quantity T is related to its Poisson bracket $\{T,\mathcal{H}\}$ with the Hamiltonian $\mathcal{H}$ by:

$$\frac{dT}{dt} = \{T,\mathcal{H}\} + \frac{\partial T}{\partial t}, \tag{3.31}$$

where

$$\{T,\mathcal{H}\} = \int \left(\frac{\delta T}{\delta \eta}\frac{\delta \mathcal{H}}{\delta q} - \frac{\delta T}{\delta q}\frac{\delta \mathcal{H}}{\delta \eta}\right) dx.$$

If T is independent of time explicitly i.e., $\dfrac{\partial T}{\partial t} = 0$, then to prove that T is a conserved

quantity, it is enough to show that its Poisson bracket with the Hamiltonian vanishes.

The functional derivative of Hamiltonian $\mathcal{H}$ w.r.t. η is given by:

$$\begin{aligned}\int_0^L \frac{\delta \mathcal{H}}{\delta \eta}\xi\, dx &= \lim_{\epsilon\to 0}\int_0^L \frac{\mathcal{H}(\eta+\epsilon\xi,\zeta)-\mathcal{H}(\eta,\zeta)}{\epsilon}\, dx \\ &= \lim_{\epsilon\to 0}\int_0^L \frac{1}{2}\frac{qG\left(\eta+\epsilon\xi,\zeta\right)q + g(\eta+\epsilon\xi)^2 - qG\left(\eta,\zeta\right)q - g\eta^2}{\epsilon}\, dx \\ &= \int_0^L \frac{1}{2}\lim_{\epsilon\to 0}\frac{qG\left(\eta+\epsilon\xi,\zeta\right)q - qG\left(\eta,\zeta\right)q}{\epsilon} + g\eta\xi\, dx \\ &= \int_0^L \left(\frac{1}{2}qD_\eta G(\eta,\zeta)[q,\xi] + g\eta\xi\right)\, dx.\end{aligned}$$

where $D_\eta G(\eta,\zeta)$ is Fréchet derivative of DNO w.r.t. η. Fréchet derivative of DNO w.r.t. η is a bilinear function in q and ξ therefore we can write

$$\int_0^L \frac{\delta \mathcal{H}}{\delta \eta}\xi\, dx = \int_0^L \left(\frac{1}{2}\xi B(\eta,\zeta)\left[q,q\right] + g\eta\xi\right)\, dx,$$

where

$$\int \xi B(\eta,\zeta)\left[q,q\right] = \int qDG(\eta,\zeta)\left[\xi,q\right], \tag{3.32}$$

is true for every smooth function ξ that satisfies periodic boundary conditions. We have dropped subscript η in DG for the sake of convenience. Substituting it in the above equation and comparing both sides, we get

$$\frac{\delta \mathcal{H}}{\delta \eta} = g\eta + \frac{1}{2}B(\eta,\zeta)\left[q,q\right].$$

The functional derivative of Hamiltonian $\mathcal{H}$ w.r.t. q is:

$$\frac{\delta \mathcal{H}}{\delta q} = \frac{G(\eta,\zeta)+G(\eta,\zeta)^\dagger}{2}q.$$

For water wave models, we know equation (1.1) is true, therefore

$$\frac{\delta \mathcal{H}}{\delta q} = \eta_t = G(\eta,\zeta)q.$$

Thus, we can say that water wave models by definition demand self-adjoint approximations of the DNO. Therefore, Hamiltonian equations can be written as

$$\eta_t = \frac{\delta \mathcal{H}}{\delta q} = G(\eta,\zeta)q, \tag{3.33}$$

$$q_t = -\frac{\delta \mathcal{H}}{\delta \eta} = -\left(g\eta + \frac{1}{2}B(\eta,\zeta)\left[q,q\right]\right). \tag{3.34}$$

To understand equation (3.32), we can try it on a simple example. Suppose we consider an example model DNO defined below as:

$$G^e(\eta,\zeta)q = -\partial_x\left((\eta+\zeta)q_x\right),$$

then the corresponding Hamiltonian is given by

$$\begin{aligned}\mathcal{H} &= \frac{1}{2}\int \left(-q\partial_x(\eta+\zeta)q_x + g\eta^2\right)\mathrm{d}x,\\ \implies \int \frac{\delta\mathcal{H}}{\delta\eta}\xi\,\mathrm{d}x &= \frac{1}{2}\int\left(\xi q_x^2 + g\eta\xi\right)\mathrm{d}x,\end{aligned}$$

and therefore Hamiltonian equations in this case are

$$\begin{aligned}\eta_t &= -\partial_x\left((\eta+\zeta)q_x\right),\\ q_t &= -\frac{1}{2}\left(g\eta + q_x^2\right).\end{aligned}$$

Here, we have $D_\eta G^e(\eta,\zeta)[q,\xi] = -\partial_x(\xi q_x)$, we can define $B(\eta,\zeta)\,[q,q] = q_x^2$, then $\int \xi B(\eta,\zeta)\,[q,q] = \int \xi q_x^2 = -\int q\partial_x(\xi q_x) = \int qDG^e(\eta,\zeta)\,[\xi,q]$.

Conservation of Energy:

Hamiltonian in our case is not an explicit function of time, thus time derivative of $\mathcal{H}$ is zero and thus from equation (3.31) it is obvious that it is conserved and it is, in fact, the total energy of the system.

Conservation of Momentum:

Water wave models conserve the momentum $P = \int q_x\eta$ when $\zeta = 0$. We can compute the Poisson bracket:

$$\begin{aligned}\{P,\mathcal{H}\} &= \int \frac{\delta P}{\delta\eta}\frac{\delta\mathcal{H}}{\delta q} - \frac{\delta P}{\delta q}\frac{\delta\mathcal{H}}{\delta\eta},\\ &= \int q_x G(\eta)q + \eta_x\left(g\eta + \frac{1}{2}B(\eta)\,[q,q]\right),\end{aligned} \tag{3.35}$$

where we used equations (3.33-3.34) in the last expression. Since for periodic boundary conditions, $\int \eta\eta_x dx = \int \frac{\partial}{\partial x}\left(\frac{\eta^2}{2}\right)dx = 0$, we have

$$\begin{aligned}\{P,\mathcal{H}\} &= \int q_x G(\eta)q + \frac{1}{2}\int \eta_x B(\eta)\,[q,q]\,,\\ &= \int q_x G(\eta)q + \frac{1}{2}\int qDG\,[\eta_x,q]\,.\end{aligned} \tag{3.36}$$

Note,

$$\begin{aligned}
\int q_x G(\eta) q &= -\int q \partial_x \left(G(\eta) q \right), \\
&= -\int q G(\eta) q_x - \int q DG(\eta) \left[\eta_x, q \right], \\
&= -\int q_x G(\eta) q - \int q DG(\eta) \left[\eta_x, q \right], \\
\implies 2 \int q_x G(\eta) q &= -\int q DG \left[\eta_x, q \right], \\
\implies \int q_x G(\eta) q &= -\frac{1}{2} \int q DG \left[\eta_x, q \right].
\end{aligned}$$

Substituting this in equation (3.36), we get $\{P, \mathcal{H}\} = 0$ and thus the momentum P is a conserved quantity.

When $\zeta \neq 0$, we can define

$$P_\zeta = \int (\eta + \zeta) q_x \, \mathrm{d}x,$$

and then following the same step of calculation as in the case for $\zeta = 0$, we get

$$\frac{dP_\zeta}{dt} = \int \zeta_x \eta \, \mathrm{d}x. \tag{3.37}$$

Conservation of Mass:

The Poisson bracket of mass $m = \int \eta$ with Hamiltonian is:

$$\begin{aligned}
\{m, \mathcal{H}\} &= \int (1) \frac{\delta \mathcal{H}}{\delta q} - 0, \\
&= \int G(\eta, \zeta) q.
\end{aligned}$$

If model DNO $G(\eta, \zeta)$ is such that its range is orthogonal to constant functions, then mass is conserved. Since, our DNO $G(\eta, \zeta)$ is self-adjoint, the statement for mass to be conserved is equivalent to that the model DNO has only constant functions in its null-space.

Conservation of Vertical Momentum:

The vertical momentum $V = \int q + gt\eta$ is conserved when

(i) The Fréchet derivative of the model Neumann condition $G(\eta, \zeta) q$ acting on constant functions is identically zero i.e., $DG(\eta)[1, q] = 0$ for all q, η, and

(ii) Range of DNO $G(\eta, \zeta)$ is orthogonal to constant functions.

To see the proof, let $v = \int q$, then

$$\frac{dv}{dt} = \{v, \mathcal{H}\} = -\int \frac{\delta \mathcal{H}}{\delta \eta} = -\int g\eta + \frac{1}{2}B(\eta, \zeta)[q, q].$$

From the assumption (i), we have $\int B(\eta, \zeta)[q, q] = \int qDG(\eta, \zeta)[1, q] = 0$, thus we have

$$\frac{dv}{dt} = -\int g\eta.$$

Since $\int \eta =$ mass is conserved under assumption (ii), we get

$$\begin{aligned} v &= -t\int g\eta + c, \\ \implies \int q + \int tg\eta &= c, \\ \implies V &= c. \end{aligned}$$

for some constant c.

Conservation of Center of Mass:

P is the momentum defined above, then the centre of mass $\mathrm{CoM} = \int x\eta - tP$ is conserved for the model water wave equations on the whole line

(i) if $\zeta = 0$, (This is required for momentum P itself to be conserved.)

(ii) if the model DNO satisfies $G(\eta)x = -\eta_x$ (in a distributional sense).

Proof is simple as follows:

$$\begin{aligned} \frac{d}{dt}\mathrm{CoM} &= \frac{\partial}{\partial t}\mathrm{CoM} + \{\mathrm{CoM}, \mathcal{H}\} = -\int P + \{x\eta, H\} - t\{P, H\}, \\ &= -\int P + \int xG(\eta)q - 0 = -\int P - \int q\eta_x = -\int P + \int q_x\eta = 0. \end{aligned}$$

Conservation of Potential Energy:

Potential energy PE is given by

$$\mathrm{PE} = \left(\int \frac{1}{2}\eta^2\right) - tV + \frac{1}{2}gt^2m,$$

where V and m are vertical momentum and mass defined above respectively.

(i) The Fréchet derivative of the model DNO $G(\eta, \zeta)q$ acting on constant functions is identically zero i.e., $DG(\eta)[1, q] = 0$ for all q, η,

(ii) Range of DNO $G(\eta, \zeta)$ is orthogonal to constant functions, and

(iii) DNO acting on surface variable η is constant function 1 i.e., $G(\eta, \zeta)\eta = 1$.

To prove this, define $s = \frac{1}{2}\int \eta^2$, then

$$\frac{ds}{dt} = \frac{\partial}{\partial t}s + \{s, \mathcal{H}\} = \int \eta \frac{\delta \mathcal{H}}{\delta q} = \int \eta G(\eta, \zeta) q = \int q G(\eta, \zeta)\eta = \int q,$$

where the last second step is true because DNO is self-adjoint and we used the assumption (iii) in last step. Note that V and m are conserved because of assumptions (i) and (ii), therefore

$$\begin{aligned}\frac{d}{dt}\text{PE} &= \frac{ds}{dt} - V + gtm, \\ &= \int q - V + gt \int \eta, \\ &= 0.\end{aligned}$$

Thus, PE is conserved under these assumptions.

Based on the conditions defined above on DNO for each of the conservation quantity, we can see that both the models (3.27) and (3.30) satisfy conditions for conservation of energy and conservation of mass. Moreover, when $\zeta = 0$, then both the models conserve momentum as well.

3.4 Forward Problem

3.4.1 Discussion on Forward Model

In mathematical physics, inverse problems are commonly characterised as the "inverse" of conventional, well-posed, "forward" problems [61]. In the context of our investigation, the forward problem involves determining the evolution of the surface displacement and velocity over time, given a set of initial conditions and a known bottom profile. In this section, we present the analytical solution of the linear component of the forward model equations, with a subsequent section presenting the numerical solution for the full nonlinear forward problem. The numerical methods described in this chapter will also be used for the observer problem discussed in Chapter 5.

The linear part of the model equations (3.25-3.26), with a trivial bottom-profile i.e., ζ are expressed as follows:

$$\eta_t = \omega^2(-i\partial_x)q, \tag{3.38}$$

$$q_t = -\eta, \tag{3.39}$$

where ω^2 is defined by equation (3.27) for regularised Boussinesq model and equation (3.30) for regularised Boussinesq−Whitham model. For readers reference we repeat the models below:

Regularised Boussinesq Model	Regularised Boussinesq−Whitham Model
$\omega^2(k) = \dfrac{1+\frac{(\mu k)^2}{6}}{1+\frac{(\mu k)^2}{2}}k^2, \quad \mathcal{P}(k) = \dfrac{1}{1+\frac{(\mu k)^2}{2}}$	$\omega^2(k) = k\dfrac{\tanh(\mu k)}{\mu}, \quad \mathcal{P}(k) = \dfrac{\tanh(\mu k)}{\mu k}$

Solution for the Linearised Model

The linear system (3.38-3.39) for both the models is:

$$\eta_t = \omega^2(-i\partial_x)q, \tag{3.40}$$

$$q_t = -\eta. \tag{3.41}$$

Differentiating equation (3.40) with respect to t and substituting q_t from equation (3.41), we obtain a single equation:

$$\eta_{tt} - \omega^2(-i\partial_x)\eta = 0.$$

Assuming a solution of the wave form type $e^{ikx\pm i\omega t}$ for η in the above equation, we obtain the following dispersion relation between ω and k (for all $k \neq 0$):

Regularised Boussinesq Model	Regularised Boussinesq−Whitham Model
$\omega_k = k\sqrt{\frac{\left(1+\frac{\mu^2k^2}{6}\right)}{\left(1+\frac{\mu^2k^2}{2}\right)}}$	$\omega_k = \sqrt{k\frac{\tanh(\mu k)}{\mu}}$

Note ω_k is given by the symbol of the Fourier multiplier shown in the definition of the model. The solution can thus be expressed as:

$$\eta = c^{(0)} + \sum_{\substack{k=-\infty \\ k\neq 0}}^{k=\infty} e^{ikx}\left(c_k^{(1)}\cos(\omega_k t) + c_k^{(2)}\sin(\omega_k t)\right), \tag{3.42}$$

where $c^{(0)}, c_k^{(1)}, c_k^{(2)}$ are constants. Using equation (3.40), the solution for q can be written as:

$$q = -c^{(0)}t + c' + \sum_{\substack{k=-\infty \\ k\neq 0}}^{k=\infty} \frac{1}{\omega_k} e^{ikx}\left(-c_k^{(1)}\sin(\omega_k t) + c_k^{(2)}\cos(\omega_k t)\right). \tag{3.43}$$

To determine the constant coefficients, we use the initial conditions $\eta(x,0) = \eta^0$ and $q(x,0) = q^0$. Let $\hat{\eta}_k^0$ and $\hat{q}_k^0$ represent the Fourier coefficients of the initial conditions η^0 and q^0. Then,

$$c^{(0)} = \hat{\eta}_0^0,\ c' = \hat{q}_0^0, c_k^{(1)} = \hat{\eta}_k^0,\ c_k^{(2)} = \omega_k \hat{q}_k^0,$$

Substituting these coefficients back into equations (3.42) and (3.43), the final solutions for η and q are:

$$\eta(x,t) = \hat{\eta}_0^0 + \sum_{\substack{k=-\infty \\ k\neq 0}}^{k=\infty} e^{ikx}\left(\hat{\eta}_k^0\cos(\omega_k t) + \omega_k\hat{q}_k^0\sin(\omega_k t)\right),$$

$$q(x,t) = \hat{q}_0^0 - \hat{\eta}_0^0 t + \sum_{\substack{k=-\infty \\ k\neq 0}}^{k=\infty} e^{ikx}\left(-\frac{1}{\omega_k}\hat{\eta}_k^0\sin(\omega_k t) + \hat{q}_k^0\cos(\omega_k t)\right).$$

3.4.2 Numerical Solution for Time Evolution in Model Equations

We now discuss the temporal evolution of surface displacement $\eta(x,t)$ through numerical simulations. Based on initial conditions for surface displacement $\eta(x,0)$ and surface velocity potential $q(x,0)$, along with the bottom profile ζ, we aim to compute the dynamic behaviour of these quantities over time. Our numerical techniques and illustrative examples are inspired by the methodologies outlined in [57].

Numerical Methodology:

- **Non-dimensional parameter:** The non-dimensional shallowness parameter here, μ, is defined as $2\pi h/L$, and for our experiments, we set $\mu = 1$, corresponding to a

fluid aspect ratio of $h/L \sim 0.16$.

- **Grid and boundary conditions:** A pseudospectral technique with an even-numbered grid of N spatial points is implemented [12, 56]. Periodic boundary conditions are applied along the spatial domain direction in the domain $[0, 2\pi]$. The spatial grid is defined as

$$x_j = (j-1)2\pi/N,\ j = 1, 2, \ldots, N.$$

- **Fourier series and derivatives:**

  ✧ Surface quantities η and q are represented and truncated using Fourier series, employing the Fast Fourier Transform (FFT) [56] across Fourier modes

$$-\frac{N}{2}, -\left(\frac{N}{2}-1\right), -\left(\frac{N}{2}-2\right), \ldots, -1, 0, 1, \ldots, \left(\frac{N}{2}-2\right), \left(\frac{N}{2}-1\right).$$

  ✧ Derivatives of η and q are computed in Fourier space using Fourier multipliers.

  ✧ Nonlinear product terms are calculated in physical space on the discretised grid, with zero padding employed to control aliasing errors [12, 56].

- **Time integration:** A fourth-order Runge-Kutta scheme is used for time integration of surface quantities. This is performed in Fourier space due to the computational efficiency offered for operators ω^2 and $\mathcal{P}$.

- **Accuracy and computational details:** Given the quadratic nonlinearity in our model equations, a total of $3N/2$ Fourier modes are used to ensuring N modes of accuracy.

Illustrative Examples: Two illustrative examples are presented, each showcasing the temporal evolution of surface displacement using both the models (3.27-3.30). Both examples utilise $N = 256$ grid points.

Conservation Laws: As discussed in 3.3, the conservation of the system's Hamiltonian and momentum is maintained when ζ is zero. In this case, the Hamiltonian can be numerically evaluated by extracting the 0^{th} Fourier mode from the Fourier series of the integrand in equation (3.28). Similarly, momentum corresponds to the 0^{th} Fourier mode of the Fourier series of $q_x\eta$ when ζ is zero. We set $\zeta = 0$ for both examples presented below.

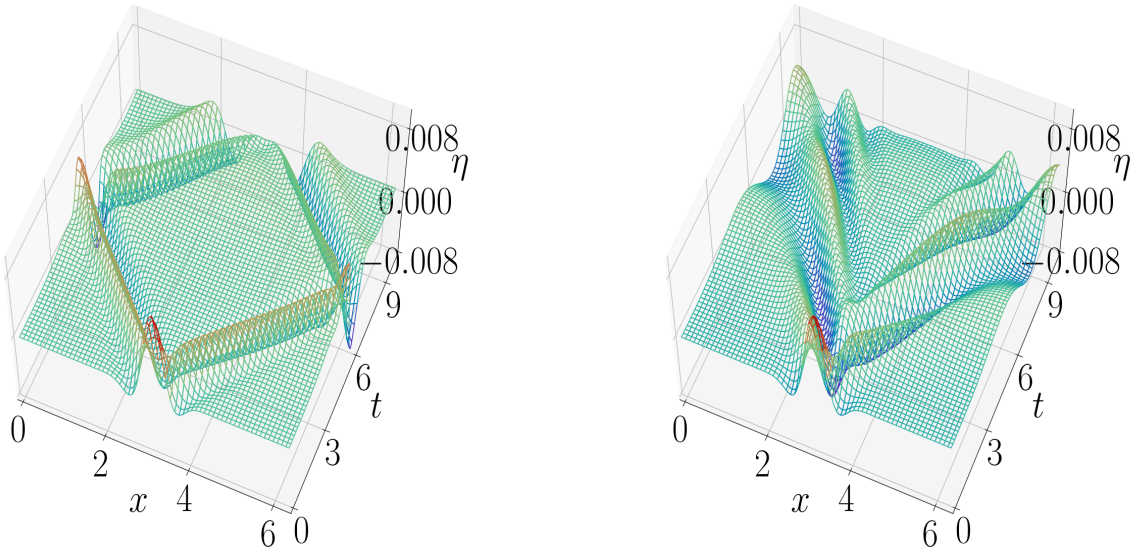

(a) Regularised Boussinesq Model

(b) Regularised Boussinesq−Whitham Model

Figure 3.2: Evolution of unsteady wave

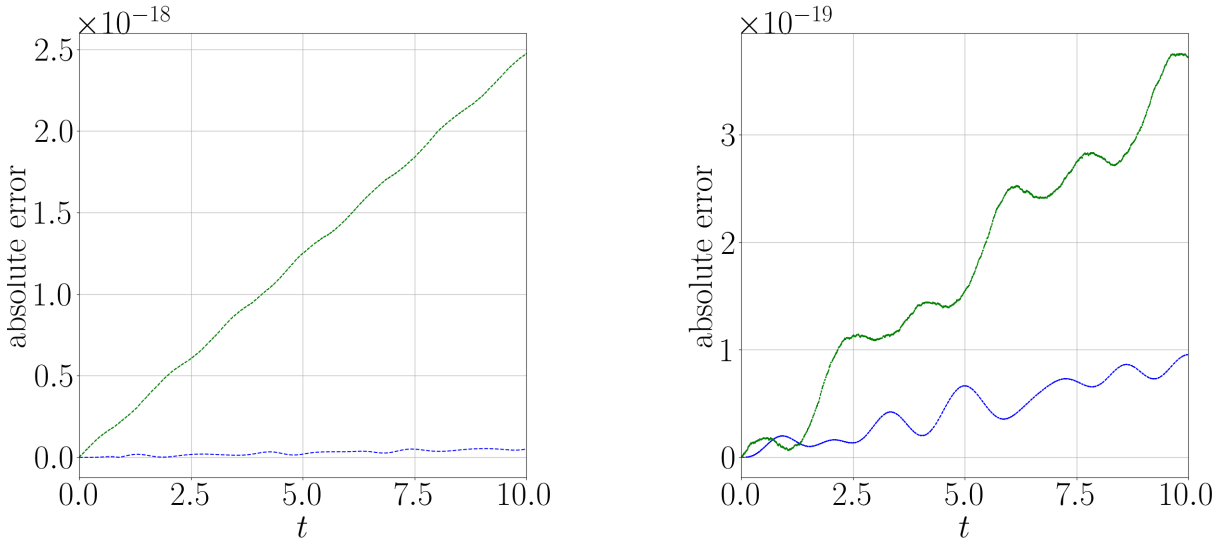

(a) Regularised Boussinesq Model

(b) Regularised Boussinesq−Whitham Model

Figure 3.3: Absolute error in Hamiltonian(in green doted lines) and in momentum(in blue doted lines) with time. Note that vertical axis is on the scale of 10^{-18} in left plot and 10^{-19} in right plot.

Unsteady wave

Let's consider an example in which we will employ the following initial conditions for surface displacement:

$$\eta_0 = 0.01e^{-4(x-\pi)^2}\cos(4x), \tag{3.44}$$

accompanied by a surface velocity potential of zero. The evolution of surface displacement obtained from the numerical method is depicted in Figure 3.2. This experiment exhibits a remarkable stability over extended time periods.

To gain a deeper understanding, let's examine the three-dimensional surface plots presented in Figure 3.2. Figures 3.2a and 3.2b illustrate the behaviour of the function $\eta(x,t)$ along the z-axis for both the regularised Boussinesq model and the regularised Boussinesq−Whitham Model respectively. As expected from the definition of the respective dispersion relations, both the models exhibit bidirectional behaviour.

In the regularised Boussinesq model 3.2a, the initial bump located at $x = \pi$ splits into two smaller, equally sized bumps, and these smaller bumps then propagate in opposite directions with identical velocities. As they approach the boundary condition, they coalesce once more, change their sign, undergo splitting again, and persist in their bidirectional journeys. This cyclic process continues if the simulation is extended. On the other hand, in the regularised Boussinesq−Whitham model, a similar initial bump at $x = \pi$ also divides into two parts, and these parts proceed to travel in opposite directions with the same speed. However, rather than simply traveling in two opposite directions, they undergo further splitting, generating smaller bumps that also propagate in opposite directions.

The behaviour described in the previous paragraph is likely due to the more dispersive tendency of Boussinesq−Whitham. A crude measure of dispersion is whether the second derivative of $\omega(k)$ is a function of wave number. Note for large k, regularised Boussinesq has a dispersion relation similar to the bidirectional wave equation which is non-dispersive in 1-dimension. Regularised Boussinesq−Whitham, on the other hand, has the same dispersion relation as the full water-wave equations. To gain a clearer understanding, refer to Figure 3.4a, which illustrates the dispersion relations for both models. It is evident that the dispersion relation for the regularised Boussinesq model is approximately a straight line, while the dispersion relation for the regularised Boussinesq−Whitham model exhibits some nonlinearity.

These observations are made with the spatial variable ranging from 0 to 2π along the x-axis and the temporal axis spanning from 0 to 10 along the y-axis. The simulations remain stable and have the potential for further continuation with similar behaviour. Importantly, both models demonstrate the conservation of their respective Hamiltonians and momenta, as evidenced by the data presented in Figure 3.3.

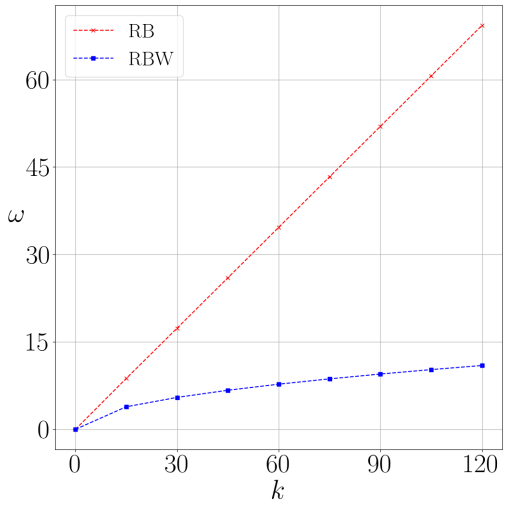

(a) Dispersion relation for $N = 256$ only for positive modes. Note we can extend for negative modes simply because $\omega(-k) = -\omega(k)$.

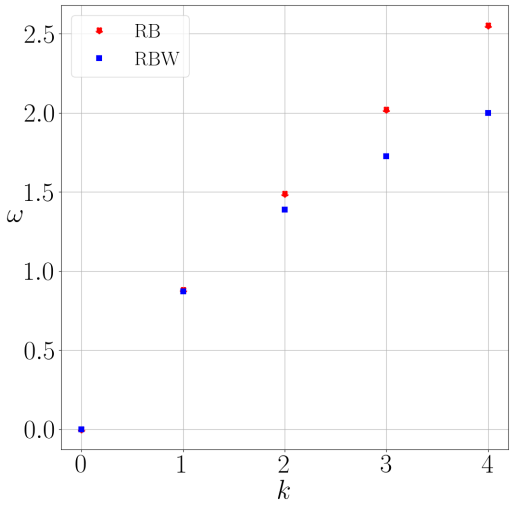

(b) Dispersion relation for first 5 modes

Figure 3.4: Dispersion relation for both the models (equations 3.27-3.30). Here, in legends, RB denotes regularised Boussinesq model and RBW denotes regularised Boussinesq−Whitham model.

Approximate traveling waves

Figure 3.5 illustrates the temporal evolution of the water's free surface, where initial conditions for surface displacement and surface velocity are set as follows

$$\eta_0 = a\cos(x) + (a/5)\cos(2x) - 0.1, \tag{3.45}$$

$$q_0 = a\sin(x) + (a/5)\sin(2x), \tag{3.46}$$

where a is set to 0.0525. These initial conditions are motivated by an approximate Stokes expansion [54] to produce disturbances that propagate without much change in shape. We emphasise these are not exact traveling wave solutions to the shallow water-wave models. The time axis spans from $t = 0$ to $t = 10$, and the x-axis ranges from 0 to 2π. Figures 3.5a and 3.5b depict the function $\eta(x, t)$ along the z-axis for the regularised Boussinesq model and the regularised Boussinesq−Whitham model, respectively.

Now, revisiting the dispersion relation, it's noteworthy that as k approaches zero, the dispersion relation is nearly identical for both models. Additionally, Figure 3.4b shows that the values of ω for both models are very close for first 3 modes. Given that the initial conditions (3.45-3.46) consist of only three modes ($k = 0, 1, 2$), both models exhibit almost the same shape while evolving over time. Since the amplitude of the initial condition is also taken to be small, the nonlinear effects are sub-dominant to the linear evolution.

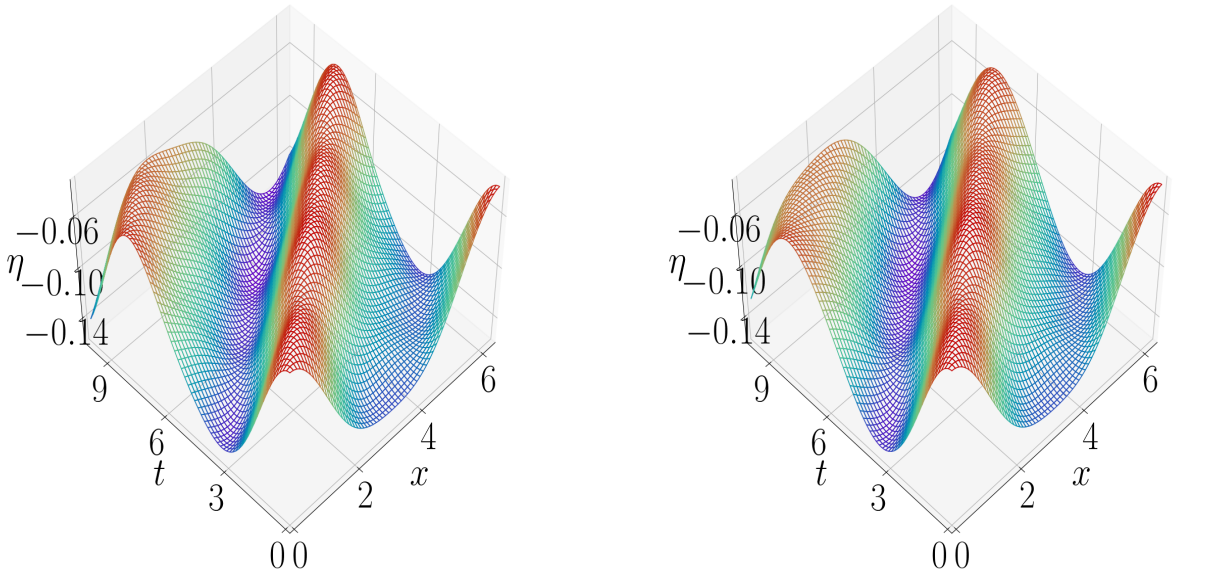

(a) Regularised Boussinesq Model

(b) Regularised Boussinesq−Whitham Model

Figure 3.5: Evolution of approximate traveling waves

In the case of a localised feature, such as a Gaussian, considered as the initial condition for η in a previous example, it is well represented in Fourier space by a suitably large number of modes. Therefore, the nonlinear effect on the dispersion relation in the regularised Boussinesq−Whitham model becomes apparent in such scenarios. However, for the initial conditions (3.45-3.46), where only first three modes ($k = 0, 1, 2$) are initially present, nonlinearity doesn't have a significant impact on either model. Although additional modes are generated over time, first three modes dominate, resulting in approximately traveling waves for both the models.

These simulations exhibit stability and have the potential for further continuation with similar behaviour. Additionally, Figure 3.6 presents the absolute errors in Hamiltonian and momentum over time, demonstrating the conservation of both quantities. This highlights the fundamental stability and consistency of our analysis across these models.

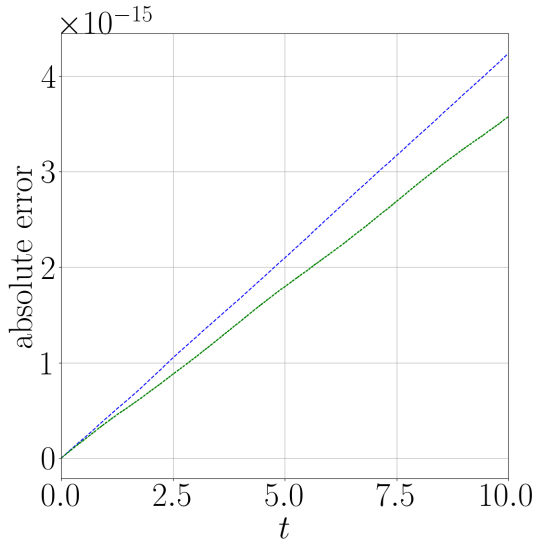

(a) Regularised Boussinesq Model

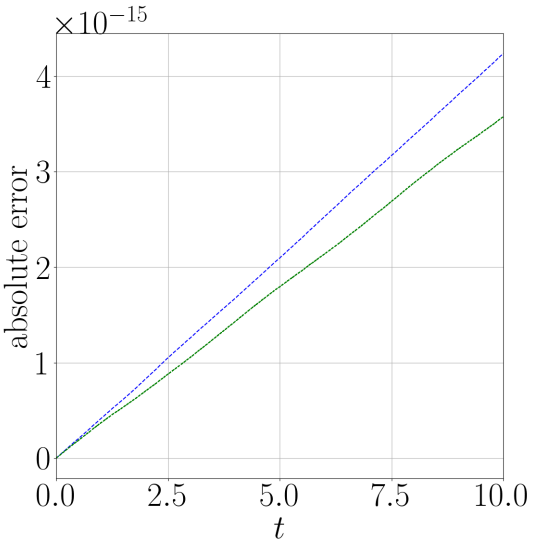

(b) Regularised Boussinesq−Whitham Model

Figure 3.6: Absolute error in Hamiltonian(in green doted lines) and in momentum(in blue doted lines) with time. Note that vertical axis is on the scale of 10^{-15}.

Chapter 4

BATHYMETRY PROBLEM GIVEN SURFACE DATA

In the previous chapter, we explored the forward problem of ocean wave dynamics: given the bottom boundary profile $\zeta(x)$ and initial conditions for surface displacement $\eta(x, t_0)$ and surface potential $q(x, t_0)$, we can determine their evolution over time. In this chapter, we delve into the inverse problem: can we recover the bottom profile $\zeta(x)$ from the observed surface displacement $\eta(x, t)$ and surface velocity $q(x, t)$ over a finite time interval? This inverse problem, known as bathymetry reconstruction, is crucial for understanding and predicting wave behaviour in various applications, including coastal engineering, marine navigation, and tsunami warning systems. Successfully solving this problem allows us to map the underwater landscape without need of direct bathymetric surveys, which can be time-consuming and expensive. To be precise, the problem addressed in this chapter is to reconstruct the bottom profile $\zeta(x)$ assuming we are given

(a) The surface displacement η and the surface potential q as functions of x and t,

(b) A model for water waves that describes the temporal evolution of η and q.

The model necessarily involves the bottom profile ζ. Note that the profile is a function of the horizontal variable alone and it is not time dependent.

This chapter outlines our method for tackling the inverse problem of reconstructing the bottom profile from surface wave observations. We start by delving into the specific techniques used to formulate the reconstruction equation and analyse the properties of the associated operator. Notably, we demonstrate that the reconstruction operator is ill-conditioned, mirroring the inherent ill-posedness of the bathymetry problem in full water-wave equations. Subsequently, we investigate the causes for this ill-posed nature, highlighting the role of the chosen water-wave model and the relation to the ill-posedness of the inverse problem in the context of the full water-wave equations. In the next

section we introduce the reconstruction operator and state some of its properties. Then we discuss a physically motivated regularisation technique that reduces the ill-conditioned nature of the problem. Finally we present some numerical results by applying our method to simulated data. These results convincingly demonstrate the capability of our approach to accurately recover the bottom profile based solely on surface observations.

4.1 The Reconstruction Operator

This thesis explores two distinct models for wave propagation: the regularised Boussinesq Model and the regularised Boussinesq−Whitham Model. Both models are governed by a system of evolution equations (3.25-3.26). For the reader's convenience, we recall these equations:

$$\begin{aligned}\eta_t &= \omega^2 q - \mathcal{P}\partial_x\left((\eta+\zeta)\mathcal{P}q_x\right),\\ q_t &= -\eta - \frac{1}{2}\left(\mathcal{P}q_x\right)^2.\end{aligned}$$

The operators ω and $\mathcal{P}$ are defined by Fourier multipliers in equations (3.27) and (3.30) respectively for the regularised Boussinesq Model and the regularised Boussinesq−Whitham Model. For convenience, we recall the definitions of ω and $\mathcal{P}$ again:

Regularised Boussinesq Model	Regularised Boussinesq−Whitham Model
$\omega^2(k) = \dfrac{1+\frac{(\mu k)^2}{6}}{1+\frac{(\mu k)^2}{2}}k^2, \quad \mathcal{P}(k) = \dfrac{1}{1+\frac{(\mu k)^2}{2}}$	$\omega^2(k) = k\dfrac{\tanh(\mu k)}{\mu}, \quad \mathcal{P}(k) = \dfrac{\tanh(\mu k)}{\mu k}$

In the governing equations for these models, it is evident that the operator $\mathcal{P}$ acts on the bottom boundary function ζ. Consequently, to determine ζ, an inversion of the operator $\mathcal{P}$ is necessary. Therefore, prior to introducing the reconstruction operator, we first mention some properties of $\mathcal{P}$ in the context of either shallow-water model. All properties are valid for both models.

Properties of the operator $\mathcal{P}$:

1. **Boundedness:** Let $f \in L^2([0,2\pi])$, where $\hat{f}$ represents the sequence of Fourier coefficients of f. The following inequalities hold:

$$\|\mathcal{P}f\|_2^2 = \int |\mathcal{P}f|^2\,\mathrm{d}x = \sum_{k=-\infty}^{\infty} |\widehat{\mathcal{P}f}|^2 = \sum_{k=-\infty}^{\infty} \mathcal{P}(k)^2|\hat{f}(k)|^2 \leq \sum_{k=-\infty}^{\infty} |\hat{f}(k)|^2 = \|f\|_2^2. \tag{4.1}$$

   In the calculations presented in equation (4.1), we initially utilise the definition of the norm, followed by Parseval's identity. Subsequently, we exploit the fact that the Fourier coefficients of the operator $\mathcal{P}$ acting on a function f is equivalent

to the multiplication of the symbol of $\mathcal{P}$ and the Fourier coefficients of f. The subsequent inequality is evident because $\mathcal{P}(k)^2 \leq 1$ holds true for both models. The last step uses the Parseval's identity. Since f is in $L^2([0, 2\pi])$, this implies that $\mathcal{P}f \in L^2([0, 2\pi])$.
Hence, based on the equation (4.1), it follows that

$$\frac{\|\mathcal{P}f\|_2}{\|f\|_2} \leq 1 \quad \text{for any } f \in L^2([0, 2\pi]).$$

Utilising the definition of the operator norm

$$\|\mathcal{P}\|_2 = \sup\left\{\frac{\|\mathcal{P}f\|_2}{\|f\|_2} : f \neq 0, f \in L^2([0, 2\pi])\right\} \tag{4.2}$$

implies $\|\mathcal{P}\|_2 \leq 1$. Therefore, $\mathcal{P}$ is bounded operator on $L^2([0, 2\pi])$ for both the models.

2. **The range of $\mathcal{P}$ is contained in $H^1([0, 2\pi])$:** The operator $\mathcal{P}$ not only is bounded but also maps functions from $L^2([0, 2\pi])$ into $H^1([0, 2\pi])$. This follows directly from the definition of the Hilbert space $H^1([0, 2\pi])$ as the set of functions:

$$\left\{f \in L^2([0, 2\pi]) \ : \ \sum_{k=-\infty}^{\infty}(1 + k^2)|\hat{f}(k)|^2 < \infty\right\} \tag{4.3}$$

The convergence of the series $\displaystyle\sum_{k=-\infty}^{\infty}(1 + k^2)\left|\widehat{\mathcal{P}f}\right|^2 < \infty$ is guaranteed as a result of the specific form of the Fourier series for $\mathcal{P}(-i\partial_x)f(x)$ in both the models as shown below:
For regularised Boussinesq model (3.27), we have

$$\begin{aligned}
\sum_{k=-\infty}^{\infty}(1 + k^2)\left|\widehat{\mathcal{P}f}\right|^2 &= \sum_{k=-\infty}^{\infty}\frac{(1 + k^2)}{\left(1 + \frac{(\mu k)^2}{2}\right)^2}\left|\hat{f}(k)\right|^2, \\
&\leq \sum_{k=-\infty}^{\infty}\frac{1 + k^2}{1 + \mu^2 k^2}\left|\hat{f}(k)\right|^2, \\
&\leq \begin{cases} \displaystyle\sum_{k=-\infty}^{\infty}\frac{1}{\mu^2}\left|\hat{f}(k)\right|^2 & \text{when } \mu \leq 1 \\ \displaystyle\sum_{k=-\infty}^{\infty}\left|\hat{f}(k)\right|^2 & \text{when } \mu > 1 \end{cases}.
\end{aligned} \tag{4.4}$$

Similarly, for regularised Boussinesq−Whitham model (3.30), we have

$$\sum_{k=-\infty}^{\infty}(1+k^2)\Big|\frac{\tanh(\mu k)}{\mu k}\hat{f}(k)\Big|^2 \leq \sum_{k=-\infty}^{\infty}\frac{1}{\mu^2}\left(1+\frac{\tanh^2(\mu k)}{k^2}\right)\big|\hat{f}(k)\big|^2 < \infty. \quad (4.5)$$

3. **Self-adjoint:** For any $f(x)$ and $g(x)$ in $L^2([0,2\pi])$, the inner product

$$\langle \mathcal{P}(-i\partial_x)f(x), g(x)\rangle = \int_0^{2\pi}\mathcal{P}(-i\partial_x)f(x)\overline{g(x)}dx = 2\pi\sum_{k=-\infty}^{\infty}\mathcal{P}(k)\hat{f}(k)\overline{\hat{g}(k)}, \quad (4.6)$$

utilising Parseval's theorem in the last step. Since, $\mathcal{P}(k)$ is real for both the models, the expression above is same as

$$2\pi\sum_{k=-\infty}^{\infty}\hat{f}(k)\overline{\mathcal{P}(k)\hat{g}(k)} = \int_0^{2\pi}f(x)\overline{\mathcal{P}(-i\partial_x)g(x)}dx = \langle f(x), \mathcal{P}(-i\partial_x)g(x)\rangle. \quad (4.7)$$

In this final step, we once again apply Parseval's theorem in the opposite direction. Consequently, $\mathcal{P}$ is self-adjoint for both the models.

4. **Boundedness of $\mathcal{P}\partial_x$:** Let $f \in L^2([0,2\pi])$. For regularised Boussinesq Model (3.27), we have

$$\|\mathcal{P}\partial_x f\|_2^2 = \sum_{k=-\infty}^{\infty}\frac{k^2}{\left(1+\frac{\mu^2k^2}{2}\right)^2}|\widehat{f}|^2 \leq \sum_{k=-\infty}^{\infty}\frac{1}{\mu^2}\frac{\mu^2k^2}{(1+\mu^2k^2)}|\widehat{f}|^2 \leq \frac{1}{\mu^2}\|f\|_2^2.$$

For regularised Boussinesq−Whitham model (3.30), we have

$$\|\mathcal{P}\partial_x f\|_2^2 = \sum_{k=-\infty}^{\infty}|k\frac{\tanh(\mu k)}{\mu k}\widehat{f}|^2 \leq \sum_{k=-\infty}^{\infty}\frac{1}{\mu^2}|\widehat{f}|^2 \leq \frac{1}{\mu^2}\|f\|_2^2.$$

Thus, $\mathcal{P}\partial_x$ is bounded operator from $L^2([0,2\pi])$ to $L^2([0,2\pi])$.

Remark. All the properties above hold true for any model where the symbol of the operator $\mathcal{P}$ satisfies the following

(a) $\mathcal{P}(k)$ is real.

(b) $(1+|k|)\mathcal{P}(k) \leq C$ for some positive constant C.

Functional whose minimiser is the true bathymetry: The reconstruction approach in [29] defines the bottom boundary as the minimiser of the functional

$$F(\tilde{\zeta}) = \int_0^{2\pi}\left(\eta_t - G(\eta,\tilde{\zeta})q\right)^2 \mathrm{d}x, \quad (4.8)$$

where η, q and η_t are given functions. Recall that $G(\eta, \zeta)$ is the Dirichlet-Neumann Operator associated with the Laplace equation that maps the Dirichlet condition q at the surface $z = \eta$ to the corresponding Neumann condition. The quantity F essentially is the mismatch between LHS and RHS in equation (2.7). In [29], the authors established a theorem proving that this functional has a unique minimiser when given data for the surface height function η, its first derivative η_t, and the surface velocity potential q at a specific time corresponding to the solutions of the complete water wave problem (2.9-2.12). Furthermore the minimiser is the true bottom profile. For shallow water models, the functional F can be suitably modified by replacing the full water-wave DNO with the model DNO obtained via truncation (as discussed in Chapter 3). Consequently, we can express the bottom surface for the shallow-water model as the minimiser of the functional

$$F^M(\tilde{\zeta}) = \int_0^{2\pi} \left(\eta_t - G^M(\eta, \tilde{\zeta})q\right)^2 \mathrm{d}x, \tag{4.9}$$

where G^M is given by equation (3.29). The evolution equation for surface displacement in both of our models is expressed by the equation $\eta_t = G^M(\eta, \zeta)$. Consequently, the function $F^M(\tilde{\zeta})$ signifies the mean square difference between predicted values $G^M(\eta, \tilde{\zeta})$ (for a given bottom profile $\tilde{\zeta}$) and true values η_t of the surface normal velocity. Substituting the value of G^M from equation (3.29) leads to

$$\zeta = \arg\min_{\zeta^*} \int \left(\eta_t - \omega^2 q + \mathcal{P}\partial_x\left((\eta + \zeta^*)\mathcal{P}q_x\right)\right)^2 dx. \tag{4.10}$$

Remark. We remind the reader of the notation that the expression $\mathcal{P}q_x$ denotes a function. When it appears in the definition of an operator, it signifies multiplication by the function $\mathcal{P}q_x$.

Suitable function space for the minimisation problem: Under the assumption that the surface displacement η and its time derivative η_t reside in the function space $L^2([0, 2\pi])$, we need to guarantee that $\omega^2 q$ also belongs to $L^2([0, 2\pi])$. For both regularised Boussinesq and regularised Boussinesq−Whitham models, this requirement is satisfied by assuming $q_x \in H^1([0, 2\pi])$. Consequently, the product $\mathcal{P}q_x$ lies in at least $H^1([0, 2\pi])$ for both models. Since any function in $H^1([0, 2\pi])$ is continuous, and continuous functions over a closed interval in $\mathbb{R}$ are bounded, we can conclude that $\mathcal{P}q_x$ is a bounded function of x. Therefore, choosing $\zeta^* \in L^2([0, 2\pi])$ allows us to bound the term $(\eta + \zeta^*)\mathcal{P}q_x$ using the Cauchy-Schwarz inequality:

$$\|(\eta + \zeta^*)\mathcal{P}q_x\|_2 \leq \|\mathcal{P}q_x\|_\infty \|(\eta + \zeta^*)\|_2.$$

This ensures $(\eta + \zeta^*)\mathcal{P}q_x$ remains in $L^2([0, 2\pi])$. We have also shown above that $\mathcal{P}\partial_x$ is bounded operator from $L^2([0, 2\pi])$ to $L^2([0, 2\pi])$. Consequently, a reasonable function space for the above minimisation problem is $\zeta^* \in L^2([0, 2\pi])$.

4.1.1 Properties of the Reconstruction Operator

To determine the true bottom profile, we shall minimise a functional using the Euler-Lagrange equation. We define the functional as

$$F^M(\tilde{\zeta}) = \int \mathcal{L}(\tilde{\zeta})\, dx,$$

where

$$\mathcal{L}(\tilde{\zeta}) = \left(\eta_t - \omega^2 q + \mathcal{P}\partial_x\left((\eta + \tilde{\zeta})\mathcal{P}q_x\right)\right)^2 = \left(b + \mathcal{M}\tilde{\zeta}\right)^2.$$

Here, $b = \eta_t - \omega^2 q + \mathcal{P}\partial_x(\eta\mathcal{P}q_x)$ depends on known quantities, and $\mathcal{M}\tilde{\zeta} = \mathcal{P}\partial_x\left(\tilde{\zeta}\mathcal{P}q_x\right)$ is a linear operator acting on $\tilde{\zeta}$. Our goal is to find the function ζ that minimises the functional $F^M(\tilde{\zeta})$. For this, we proceed as follows:

$$\begin{aligned}
\int \frac{\delta\mathcal{L}}{\delta\tilde{\zeta}}\xi(x)\,\mathrm{d}x &= \lim_{\epsilon\to 0}\int \frac{\left(b + \mathcal{M}(\tilde{\zeta} + \epsilon\xi)\right)^2 - \left(b + \mathcal{M}\tilde{\zeta}\right)^2}{\epsilon}\,\mathrm{d}x, \\
&= \lim_{\epsilon\to 0}\int \frac{\epsilon^2(\mathcal{M}(\xi))^2 + 2\epsilon\mathcal{M}(\tilde{\zeta})\mathcal{M}(\xi) + 2\epsilon b\mathcal{M}(\xi)}{\epsilon}\,\mathrm{d}x, \\
&= 2\int \left(\mathcal{M}^\dagger\mathcal{M}(\tilde{\zeta}) + \mathcal{M}^\dagger b\right)\xi(x)\,\mathrm{d}x,
\end{aligned}$$

where $\xi(x)$ is an arbitrary test function in $L^2([0, 2\pi])$, and $\mathcal{M}^\dagger f = -\mathcal{P}q_x\partial_x(\mathcal{P}f)$ is the L^2-adjoint of $\mathcal{M}$. Consequently, we obtain

$$\frac{\delta\mathcal{L}}{\delta\tilde{\zeta}} = 2\left(\mathcal{M}^\dagger\mathcal{M}(\tilde{\zeta}) + \mathcal{M}^\dagger b\right).$$

Hence the equation for the minimiser of F^M is given by

$$(\mathcal{P}q_x)\partial_x^2\mathcal{P}^2(\zeta\mathcal{P}q_x) = -(\mathcal{P}q_x)\partial_x\mathcal{P}\left(\eta_t - \omega^2 q + \mathcal{P}\partial_x(\eta\mathcal{P}q_x)\right). \tag{4.11}$$

Since all terms on the right-hand side are known, solving for the function ζ requires inverting the operator

$$B\ :\ f \to (\mathcal{P}q_x)\partial_x^2\mathcal{P}^2((\mathcal{P}q_x)f). \tag{4.12}$$

We refer to B as the reconstruction operator. Let's analyse some properties of the operator B:

1. **Boundedness**: The operator B is defined as the composition of three operations.

Firstly, it involves multiplication by the function $\mathcal{P}q_x$. Secondly, it includes the operator $\mathcal{P}^2\partial_x^2$ acting on a function in $L^2([0,2\pi])$. Thirdly, it involves multiplication by the function $\mathcal{P}q_x$ once again. We have previously established that $\mathcal{P}\partial_x$ is a bounded operator, and therefore, the operator $\mathcal{P}^2\partial_x^2$ is also bounded for both the models. Regarding the first and third components, $\mathcal{P}$ maps $L^2([0,2\pi])$ functions to at least $H^1([0,2\pi])$ functions. Additionally, $H^1([0,2\pi]) \subset C^0([0,2\pi])$. Consequently, $\mathcal{P}q_x$ is continuous when $q_x \in L^2([0,2\pi])$ and since $[0,2\pi]$ is a bounded interval, $\mathcal{P}q_x$ is a bounded continuous function of x. Multiplication by a bounded continuous real-valued function results in a bounded operator on $L^2([0,2\pi])$, therefore we conclude that B is indeed a bounded operator.

2. **Self-adjoint:** For any $f_1, f_2 \in L^2([0,2\pi])$,

$$\langle Bf_1, f_2\rangle = \int_0^{2\pi} (\mathcal{P}q_x)\partial_x^2\mathcal{P}^2((\mathcal{P}q_x)f_1)f_2 dx = \int_0^{2\pi} f_1(\mathcal{P}q_x)\mathcal{P}^2\partial_x^2\left((\mathcal{P}q_x)f_2\right)dx = \langle f_1, Bf_2\rangle.$$

Thus, B is a self-adjoint operator. Note we have used the fact that the symbol of $(\mathcal{P}\partial_x)^2$ is real-valued. Hence it corresponds to a self-adjoint operator on $L^2([0,2\pi])$.

3. **Compact operator for regularised Boussinesq model:** For the regularised Boussinesq model, we establish that $\mathcal{P}\partial_x$ maps functions in $L^2([0,2\pi])$ to at least $H^1([0,2\pi])$. We proceed as follows:

$$\begin{aligned}\|\mathcal{P}\partial_x f\|_{H^1}^2 &= \sum_{k=-\infty}^{\infty} \frac{k^2(1+k^2)}{\left(1+\frac{\mu^2k^2}{2}\right)^2}|\widehat{f}|^2 \leq \sum_{k=-\infty}^{\infty} \frac{k^2+k^4}{(\mu^4k^4/4+\mu^2k^2)}|\widehat{f}|^2,\\ &\leq \sum_{k=-\infty}^{\infty} \frac{4}{\mu^4}\frac{\mu^4k^2/4+\mu^4k^4/4}{(\mu^4k^4/4+\mu^2k^2)}|\widehat{f}|^2 \leq \frac{4}{\mu^4}\|f\|_2^2.\end{aligned}$$

Here, we utilise the fact that $\mu \leq 1$. Similarly, for $\mu > 1$, we have

$$\begin{aligned}\|\mathcal{P}\partial_x f\|_{H^1}^2 &= \sum_{k=-\infty}^{\infty} \frac{k^2(1+k^2)}{\left(1+\frac{\mu^2k^2}{2}\right)^2}|\widehat{f}|^2 \leq \sum_{k=-\infty}^{\infty} \frac{k^2+k^4}{(\mu^4k^4/4+\mu^2k^2)}|\widehat{f}|^2,\\ &\leq \sum_{k=-\infty}^{\infty} \frac{k^2+k^4}{(k^4/4+k^2)}|\widehat{f}|^2 \leq 4\|f\|_2^2.\end{aligned}$$

Consequently, $\mathcal{P}^2\partial_x^2$ also maps functions in $L^2([0,2\pi])$ to at least $H^1([0,2\pi])$. Also we have shown before that $\mathcal{P}q_x$ is at least in $H^1([0,2\pi])$ when $q_x \in L^2([0,2\pi])$. The property of $H^1([0,2\pi])$ being an algebra ensures that B maps $L^2([0,2\pi])$ to $H^1([0,2\pi])$. Since $H^1([0,2\pi])$ is compactly embedded in $L^2([0,2\pi])$ [28], we conclude B is a compact operator for regularised Boussinesq model.

For the regularised Boussinesq−Whitham model, the reconstruction operator B is not

compact as shown in the following theorem:

Theorem 1. *Suppose $q_x \in L^2([0, 2\pi])$ and $\mathcal{P}q_x$ is not identically zero, then for regularised Boussinesq−Whitham model, B is not a compact operator.*

Proof. We recall the definition of a compact operator. Let $T : X \to Y$ be a linear map, where X and Y are Banach spaces. The map T is compact if for any bounded sequence $(x_n)_{n\in\mathbb{N}}$ in X, the sequence $(Tx_n)_{n\in\mathbb{N}}$ contains a converging subsequence.

Focusing on B, we recognise that it comprises three components. Two involve simple multiplication, while the third is the operator $\mathcal{P}^2\partial_x^2$ acting on functions within $L^2([0, 2\pi])$. Our strategy lies in proving the non-compactness of $\mathcal{P}^2\partial_x^2$ (in the case of regularised Boussinesq−Whitham) and subsequently inheriting this property to B.

Non-compactness of $\partial_x^2\mathcal{P}^2$: Consider the symbol of $\mathcal{P}^2\partial_x^2$, which has the form $-\tanh^2(\mu k)/\mu^2$. As the absolute value of k goes to infinity, this multiplier doesn't approach zero. This hints at the non-compact nature of the operator. To establish this rigorously, we present a proof by considering an orthonormal sequence in $L^2([0, 2\pi])$ defined as $a_n = \sin(nx)/\sqrt{\pi}$, $n = 1, 2, \ldots$, where $\|a_n\| = 1$.
For any $n, m \in \mathbb{N}$ where $m \neq n$, we have

$$\begin{aligned}
\|\partial_x^2\mathcal{P}^2(a_n - a_m)\|_2^2 &= \int_0^{2\pi} \left|\partial_x^2\mathcal{P}^2\left(a_n - a_m\right)\right|^2 \mathrm{d}x, \\
&= 2\pi \sum_{k=-\infty}^{\infty} \frac{\tanh^4(\mu k)}{\mu^4} \left|\mathcal{F}[a_n - a_m]_k\right|^2, \\
&= \sum_{k=-\infty}^{\infty} \frac{\tanh^4(\mu k)}{\mu^4} \left|\delta(k-n) - \delta(k-m)\right|^2, \\
&= \frac{\tanh^4(\mu n)}{\mu^4} + \frac{\tanh^4(\mu m)}{\mu^4}, \\
&\geq 2\frac{\tanh^4(\mu)}{\mu^4},
\end{aligned}$$

where in the second line, Parseval's identity was applied and $\mathcal{F}$ represents the Fourier transform of the function. Moving to the third line, we explicitly expressed the Fourier multipliers of a_n and a_m. Since $\delta(k-n)\delta(k-m) = 0$ when $m \neq n$, the forth line holds and the last line is true because tanh is monotonically increasing function.
Thus, we have a bounded sequence a_n such that $\|\partial_x^2\mathcal{P}^2(a_n - a_m)\|_2$ is bounded below by a positive number for all $n \neq m$. This implies that the sequence $\partial_x^2\mathcal{P}^2(a_n)$ can not have any convergent subsequence, establishing that $\partial_x^2\mathcal{P}^2$ is not a compact operator.

We now aim to demonstrate that B is not a compact operator. Similar to our approach for the operator $\mathcal{P}^2\partial_x^2$, we must find a bounded sequence $(v_n)_{n\in\mathbb{N}}$ such that $\|B(v_n - v_m)\|_2$ is bounded below by a positive number for all n and m. Therefore, it is imperative to position ourselves sufficiently far from the null space of the operator $\partial_x^2\mathcal{P}^2$ and away from

the zeros of the function $\mathcal{P}q_x$.

Avoiding Zeros of $\mathcal{P}q_x$: When q_x is in L^2, then $\mathcal{P}q_x$ is a continuous function. Let's define a set S' where $\mathcal{P}q_x$ is away from zero. S' is non-empty because $\mathcal{P}q_x$ is not identically zero. Since $\mathcal{P}q_x$ is continuous, we can identify a non-empty connected component S of S'. Specifically, S is a non-empty connected component of the set $\{x \in [0, 2\pi] : |\mathcal{P}q_x| \geq c\}$ for some $c > 0$.

Orthogonality of $\mathcal{P}q_x$ with $\partial_x^2\mathcal{P}^2(\cdot)$: Consider $\mathcal{P}q_x$ restricted to S, denoted as $\mathcal{P}q_x\Big|_S$, which is an element of $L^2(S)$. Let X be the orthogonal complement of span of $\mathcal{P}q_x\Big|_S$ in $L^2(S)$. An orthonormal sequence w_n in X is constructed as follows: Take an orthonormal sequence in $L^2(S)$, project it onto X and then apply Gram-Schmidt on it. Remove any trivial elements in this process. Thus, sequence w_n obtained now is an orthonormal sequence in $L^2(S)$ which is also orthogonal to $\mathcal{P}q_x\Big|_S$. Finally, defining $v_n = w_n\chi_S$ where χ_S is the indicator function on S we obtain a bounded sequence in v_n in $L^2([0, 2\pi])$ whose image under B satisfies:

$$
\begin{aligned}
\|Bv_n - Bv_m)\|_2^2 &= \int_0^{2\pi} \Big((\mathcal{P}q_x)\partial_x^2\mathcal{P}^2\left((\mathcal{P}q_x)(v_n - v_m)\right)\Big)^2 \,\mathrm{d}x, \\
&= \int_S (\mathcal{P}q_x)^2\Big(\partial_x^2\mathcal{P}^2\left((\mathcal{P}q_x)(w_n - w_m)\right)\Big)^2 \,\mathrm{d}x, \\
&\geq c^2 \int_0^{2\pi} \Big(\partial_x^2\mathcal{P}^2\left((\mathcal{P}q_x)(v_n - v_m)\right)\Big)^2 \,\mathrm{d}x, \\
&= 2\pi c^2 \sum_{k=-\infty}^{\infty} \frac{\tanh^4(\mu k)}{\mu^4} \Big|\mathcal{F}\Big((\mathcal{P}q_x)(v_n - v_m)\Big)_k\Big|^2, \\
&\geq 2\pi c^2 \frac{\tanh^4(\mu)}{\mu^4} \sum_{\substack{k=-\infty \\ k\neq 0}}^{\infty} \Big|\mathcal{F}\Big((\mathcal{P}q_x)(v_n - v_m)\Big)_k\Big|^2, \\
&= c^2 \frac{\tanh^4(\mu)}{\mu^4} \int_0^{2\pi} \left((\mathcal{P}q_x)(v_n - v_m)\right)^2 \mathrm{d}x, \\
&\geq c^4 \frac{\tanh^4(\mu)}{\mu^4} \int_0^{2\pi} (v_n - v_m)^2 \,\mathrm{d}x = 2c^4 \frac{\tanh^4(\mu)}{\mu^4}.
\end{aligned}
$$

Here, the second and third lines utilise the relation of v_n and w_n and hold true because $|\mathcal{P}q_x| \geq c$ is true in S. For the fourth line, Parseval's identity is applied. Recognising that tanh is monotonic increasing and vanishes at $k = 0$, we can safely discard the zeroth Fourier mode in the fifth line. The next line relies on the orthogonality between $\mathcal{P}q_x$ and v_n, ensuring $\mathcal{F}\Big((\mathcal{P}q_x)(v_n - v_m)\Big)_{k=0} = 0$ and therefore Parseval's identity in reverse direction can be used then last line is obvious as $|\mathcal{P}q_x| \geq c$.

Consequently, $\|Bv_n - Bv_m\|_2^2$ is bounded below by positive number and therefore, no subsequence of Bv_n can converge in $L^2([0, 2\pi])$. Hence, B is not compact. □

Remark. For the regularised Boussinesq−Whitham model, the function $\mathcal{P}(k) = \tanh(\mu k)/\mu k >$

0 for all non-zero values of k. This implies that $\mathcal{P}q_x$ is identically zero if and only if q_x itself is identically zero. Therefore, we can equivalently state the theorem as follows:

Theorem. *Suppose $q_x \in L^2([0, 2\pi])$ and q_x is not identically zero, then the operator B is not compact for the regularised Boussinesq– Whitham model.*

Requiring q_x to be non-zero makes physical sense since it's impossible to recover the bottom boundary shape without any horizontal velocity at the top surface. As discussed in Section 3.1, any bottom profile is possible when water is completely still. Since the velocity potential is a harmonic function, the velocities in the bulk of the fluid domain are zero if and only if the velocities on the free surface are zero.

4.1.2 The Spectrum of the Reconstruction Operator B:

As demonstrated below, the spectrum of operator B lies entirely on the negative real axis:

$$\int fBf = \int f(\mathcal{P}q_x)\partial_x^2\mathcal{P}^2((\mathcal{P}q_x)f)\,\mathrm{d}x = -\int (\mathcal{P}\partial_x((\mathcal{P}q_x)f))^2\,\mathrm{d}x \leq 0.$$

Recall our initial objective was to invert the operator B, and now, recognising that it possesses eigenvalues on the negative real line and is compact for the regularised Boussinesq model, we can infer that zero is a limit point of the eigenvalues of B and hence zero belongs to the spectrum. Nevertheless, we establish that zero is not an eigenvalue of the operator B for either of our models under appropriate conditions, as indicated in the following theorem:

Theorem 2. *Suppose $q \in H^2([0, 2\pi])$ and the function $\mathcal{P}q_x$ only vanishes on a set of measure zero, then the operator B has no zero eigenvalue for either of the models given in (3.27) and (3.30).*

Proof. Let's assume that zero is an eigenvalue of the operator B. This implies that there exists a function $f \in L^2([0, 2\pi])$ such that

$$(\mathcal{P}q_x)\partial_x^2\mathcal{P}^2((\mathcal{P}q_x)f) = 0. \tag{4.13}$$

We now show that no such non-zero f in $L^2([0, 2\pi])$ exists.

Assuming $\mathcal{P}q_x$ only vanishes on a set of measure zero, from the above equation, it follows that $\partial_x^2\mathcal{P}^2((\mathcal{P}q_x)f)$ is zero almost everywhere. Since $q \in H^2([0, 2\pi])$, and $\mathcal{P}\partial_x$ is bounded operator on $H^2([0, 2\pi])$, $\mathcal{P}q_x \in H^2([0, 2\pi])$ and is thus a continuous function. Consequently, $\partial_x^2\mathcal{P}^2((\mathcal{P}q_x)f)$ is not merely zero almost everywhere but is zero everywhere i.e.,

$$\partial_x^2\mathcal{P}^2((\mathcal{P}q_x)f) = 0. \tag{4.14}$$

For both of our models (3.27) and (3.30), $\mathcal{F}_k(\partial_x^2\mathcal{P}^2) = -k^2\mathcal{P}(k)^2 < 0$ for all $k \neq 0$. Thus, for $\partial_x^2\mathcal{P}^2((\mathcal{P}q_x)f)$ to be zero, $(\mathcal{P}q_x)f$ must be a constant. Let's denote this constant as A:

$$(\mathcal{P}q_x)f = A. \tag{4.15}$$

Now, we'll consider two cases: when $A = 0$ and $A \neq 0$ and show that f cannot be an eigenfunction in $L^2([0, 2\pi])$ in either case.

1. $A = 0$: We have $(\mathcal{P}q_x)f = 0$. Since $\mathcal{P}q_x$ is zero only on a set of measure zero, this implies f has to be zero almost everywhere. Thus, f can't be an eigenfunction, and therefore, zero is not an eigenvalue.

2. $A \neq 0$: Since $\mathcal{P}q_x$ is in $H^2([0, 2\pi])$ and $H^2([0, 2\pi])$ is embedded in $C^{1,\frac{1}{2}}[0, 2\pi]$ using Sobolev embedding theorem [27] and therefore, $\mathcal{P}q_x \in C^{1,\frac{1}{2}}[0, 2\pi]$. Moreover, $\mathcal{P}q_x$ is continuous and since its Fourier coefficient at $k = 0$ vanishes, the mean value theorem guarantees the presence of at least one point where $\mathcal{P}q_x$ vanishes within the domain $[0, 2\pi]$. We can assume this zero occurs at $x = 0$ without loss of generality. Employing the Taylor series with the Lagrange form of the remainder around $x = 0$, we can express $\mathcal{P}q_x$ in a neighbourhood of $x = 0$:

$$\mathcal{P}q_x = 0 + (x - 0)\frac{d\mathcal{P}q_x}{dx}\bigg|_{x=s}, \quad \text{for } |x| \text{ sufficiently small} \tag{4.16}$$

where s lies between 0 and x. Adding and subtracting a term in the above equation, we get

$$\mathcal{P}q_x = x\frac{d\mathcal{P}q_x}{dx}\bigg|_{x=0} + x\left(\frac{d\mathcal{P}q_x}{dx}\bigg|_{x=s} - \frac{d\mathcal{P}q_x}{dx}\bigg|_{x=0}\right). \tag{4.17}$$

Since, $\mathcal{P}q_x \in C^{1,\frac{1}{2}}[0, 2\pi]$, the derivatives of $\mathcal{P}q_x$ are Hölder continuous with exponent $1/2$ and thus there exist a nonnegative real constant c_1 such that

$$\left|\frac{d\mathcal{P}q_x}{dx}\bigg|_{x=s} - \frac{d\mathcal{P}q_x}{dx}\bigg|_{x=0}\right| \leq c_1|s|^{1/2} \leq c_1|x|^{1/2}. \tag{4.18}$$

Moreover, a Hölder continuous function on bounded domain of $\mathbb{R}$ is bounded, and thus, there exist nonnegative real constant c_2 such that

$$\left|\frac{d\mathcal{P}q_x}{dx}\bigg|_{x=0}\right| \leq c_2. \tag{4.19}$$

Using equations (4.18-4.19) in equation (4.17), we have

$$|\mathcal{P}q_x| \leq |x|c_2 + c_1|x|^{3/2}.$$

Note that both c_1 and c_2 cannot be zero because that would imply $\mathcal{P}q_x$ is zero in an open interval. Thus, for $|x| < 1$, we have

$$|\mathcal{P}q_x| \leq |x|(c_2 + c_1).$$

Substituting this into equation (4.15), we get the eigenfunction f satisfies

$$|f| = \frac{|A|}{|\mathcal{P}q_x|} \geq \frac{|A|}{|\mathcal{P}q_x|} \geq \frac{|A|}{|x|(c_2 + c_1)|}. \tag{4.20}$$

This implies that f cannot be in $L^2([0, 2\pi])$. Thus, f is not an eigenfunction.

□

While the previous proof guarantees that the operator B does not possess any zero eigenvalues, the operator B still exhibits signs of ill-conditioning. This becomes particularly evident in the regularised Boussinesq model, where the operator B is compact. A key characteristic of compact operators is that zero is a limit point of its eigenvalues [39]. This implies that eigenvalues cluster around zero, making the inverse operator highly sensitive to small perturbations in the input or noise.

Moreover, for either model, for $q \in H^1([0, 2\pi])$, the function $\mathcal{P}q_x$ is continuous and has an average value of zero. This implies that there is at least one point $x \in [0, 2\pi]$ for which $\mathcal{P}q_x$ is zero. Thus zero is an approximate eigenvalue of the operator B. To illustrate this, let's think about a sequence of smooth functions denoted as $f_n(x)$ converging to a function $f(x)$ defined as follows: The functions $f_n(x)$ possess compact support centred around the zero of $\mathcal{P}q_x$ and serve as approximations to a Dirac delta distribution situated at such a zero. Then we have

$$\lim_{n\to\infty} \langle f_n, B\zeta \rangle = 0, \quad \text{for any } \zeta \in L^2[0, 2\pi],$$

where the inner product $\langle f, g \rangle$ between two functions f and g is defined as the integral of their product, i.e., $\int fg\, dx$. Consequently, we have $\langle \zeta, Bf_n \rangle$ approaching zero, which leads to the conclusion that $Bf_n \to 0$, and thus Bf equals zero. As a result, B behaves as if it possesses a zero eigenvalue, even though it doesn't have zero eigenvalue in reality. Thus, for both the models, regularisation of the operator is necessary.

4.2 Regularising the Reconstruction Operator

Equation (4.11) presents a deceptively simple framework for bottom boundary reconstruction. However, the ease of solving this equation is hindered by the ill-conditioned nature of the operator B featured on the left-hand side. Despite zero not being an eigenvalue of the operator B, it remains ill-posed primarily for two reasons:

1. In the case of the regularised Boussinesq model (3.27), zero is as an accumulation point for the eigenvalues of the compact operator B.

2. The function $\mathcal{P}q_x$, present in B's definition for both models, necessarily vanishes at some point x. This effectively creates an approximate zero eigenvalue for B, resulting in ill-conditioning.

Since the true bottom profile ζ is independent of time, we demand that it simultaneously minimises the functional of (4.10) at multiple time instances. This leads to the following minimisation problem:

$$\zeta = \arg\min_{\zeta^*} \sum_{j=1}^{M} \int \left(\eta_t^{(j)} - \omega^2 q^{(j)} + \mathcal{P}\partial_x \left((\eta^{(j)} + \zeta^*)\mathcal{P}q_x^{(j)}\right)\right)^2 dx, \tag{4.21}$$

where the superscript j implies that the data (η, η_t, q_x) is at time t_j $(j = 1, 2, \ldots, M)$. The associated Euler-Lagrange equation for this problem is analogous to equation (4.11) but involves a summation over times t_j on both sides:

$$\sum_{j=1}^{M} \left[\mathcal{P}q_x^{(j)}\, \mathcal{P}^2\partial_x^2 \left(\mathcal{P}q_x^{(j)}\, \zeta^*\right)\right] = -\sum_{j=1}^{M} \left[\mathcal{P}q_x^{(j)}\, \mathcal{P}\partial_x \left(\eta_t^{(j)} - \omega^2 q^{(j)} + \mathcal{P}\partial_x \left(\eta^{(j)}\, \mathcal{P}q_x^{(j)}\right)\right)\right]. \tag{4.22}$$

This technique proves particularly effective when the zeros of the function $\mathcal{P}q_x$ vary spatially across different time instances. Therefore, we choose initial conditions that satisfy this condition. For ease of reference later, we define the operator

$$B_M(\zeta^*) = \sum_{j=1}^{M} \left[\mathcal{P}q_x^{(j)}\, \mathcal{P}^2\partial_x^2 \left(\mathcal{P}q_x^{(j)}\, \zeta^*\right)\right]. \tag{4.23}$$

Our aim is to address the ill-conditioning of the reconstruction operator B. Thus we are motivated to investigate the eigenvalues of finite dimensional truncations of the operator on the left hand side of equation (4.22).

4.2.1 Numerical Results

As mentioned earlier, the equation (4.11) falls short in providing an effective reconstruction procedure for the bottom-profile. Figure 4.1 visually demonstrates this. In the Figure 4.1a, two zeros of the function $\mathcal{P}q_x$ are evident at $x = 0$ and $x = \pi$. The reconstructed bottom profile obtained by inverting (a finite-dimensional approximation of) the operator B (dotted red line) displays a clear discontinuity at these points, significantly diverging from the actual profile (green solid line). However, for the remaining points, the two profiles exhibit relative closeness. The discontinuity observed near the end of the grid can be attributed to the periodic boundary condition, and the zero at $x = 0$

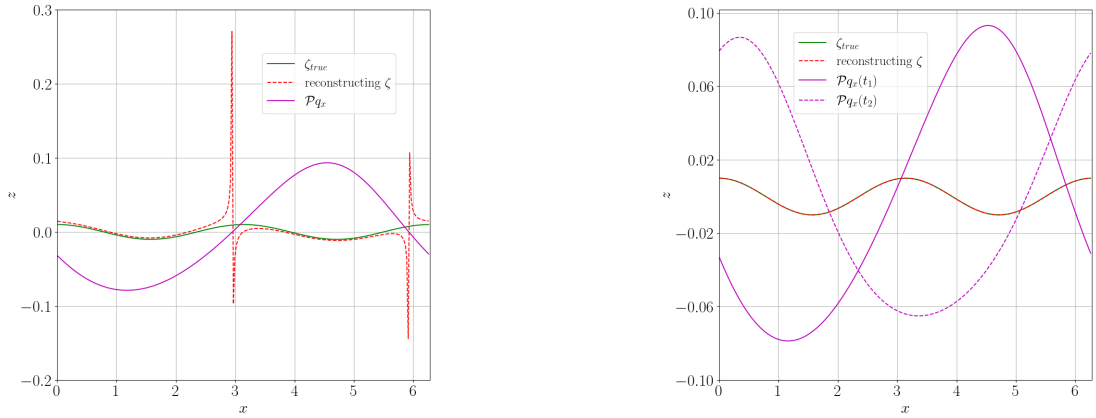

(a) (b)

Figure 4.1: Bottom profile reconstruction using equation (4.22) with data from one ($M = 1$) and two ($M = 2$) time instances in Figures 4.1a and 4.1b respectively. The true profile (solid green), reconstructed profile (dashed red), and values of $\mathcal{P}q_x$ (magenta) are shown. When using data from one time instance shown in left, significant deviations occur near zeros of $\mathcal{P}q_x$. These deviations are reduced when using two data points (where the zeros of $\mathcal{P}q_x$ do not coincide in space) as shown in right.

accounts for the encountered issue. Consequently, the zeros of the function $\mathcal{P}q_x$ pose a challenge in the reconstruction process. It seems natural to want to impose continuity of the reconstructed bottom profile at the zero of $\mathcal{P}q_x$. At the same time we want to ensure this continuity without affecting the quality of the reconstruction at all other points in the domain. Here's where equation (4.22) comes to the rescue! As Figure 4.1b showcases, using two data points significantly improves the reconstruction. Crucially, these data points are chosen at different times so that the zeros of $\mathcal{P}q_x$ don't coincide. This clever strategy mitigates the disruptive impact of zeros, leading to a much closer match between the reconstructed and actual profiles.

We know that the function $\mathcal{P}q_x$ has at least one zero in space. Hence to recover the bottom-profile, the key lies in ensuring that the the time-dependence of the velocity potential q is such that the location of the zeros of $\mathcal{P}q_x$ do not remain fixed in space for all time. There are many choices of q for which the zeros of $\mathcal{P}q_x$ will vary in time. Here, we show two examples of velocity potentials that satisfy our requirements. Note these are not obtained from solving the shallow-water models but are chosen to highlight our regularisation procedure. In Figure 4.2a, we have $q(x,t) = 0.1\sin(x-t)+0.3$ and we plot q (different dashed green lines correspond to different time instance) and $\mathcal{P}q_x$ (different solid blue lines correspond to different time instance) with a grid size of 256 and for $t = 2\pi j/15$, $j = 1, 2, \ldots, 15$. Here, we can see the zeros of q as well as zeros of $\mathcal{P}q_x$ are not fixed in time. The constant offset 0.3 in q is added for the sake of distinguishing q and $\mathcal{P}q_x$ in the Figure 4.2a. The second Figure 4.2b, we have $q(x,t) = 0.1\sin(x-t)\cos(x)+0.3$

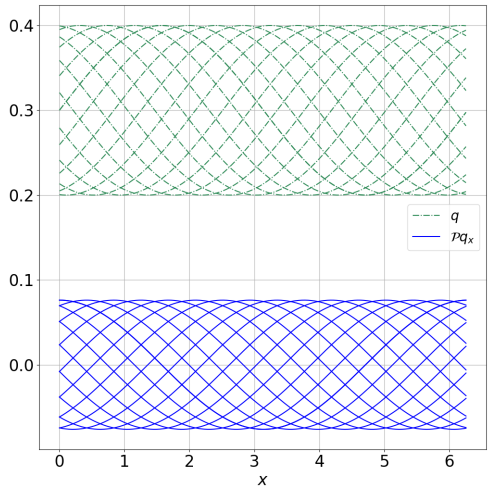

(a) Zeros of q as well as zeros of $\mathcal{P}q_x$ vary in time where $q(x,t) = 0.1\sin(x-t) + 0.3$.

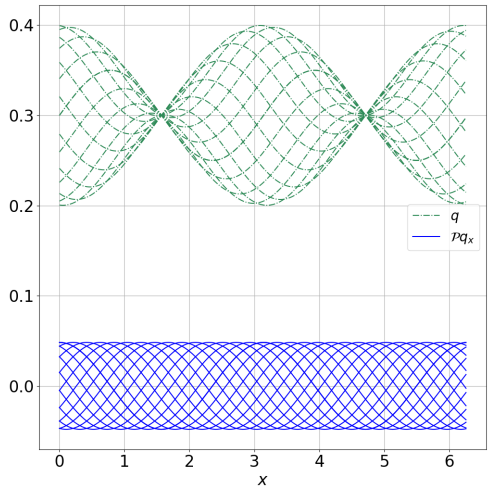

(b) Zeros of q are fixed in time but zeros of $\mathcal{P}q_x$ vary in time where $q(x,t) = 0.1\sin(x-t)\cos(x) + 0.3$.

Figure 4.2: Some Examples where zeros of $\mathcal{P}q_x$ vary in time for regularised Boussinesq−Whitham model.

with the same grid size and same values of t as in the previous example. Although the zeros of q remains fixed in the time, zeros of $\mathcal{P}q_x$ vary in time. Examples shown here are for regularised Boussinesq−Whitham model. They look similar for regularised Boussinesq model.

To analyse the impact of M on the invertibility of the operator B_M in equation (4.23), let's examine the eigenvalues of this operator across different values of M. Consider a periodic traveling-wave profile for the velocity potential $q(x,t) = 0.1\sin(x-t)$. We discretised this function on a uniform grid in the x-variable with 256 points. We will consider the values of t on a uniform grid of $t = 2\pi j/M$ where $j = 1, 2, \ldots, M$. We follow these steps for different values of $M = 1, 2, 10, 100, 200$:

1. For fixed t, compute the matrix representation of the operator $\mathcal{P}q_x\,\mathcal{P}^2\partial_x^2\,(\mathcal{P}q_x\,\cdot)$ using a pseudospectral method. Each matrix thus obtained will be a real symmetric matrix of the size of our spatial grid, that is 256×256 in this case.

2. Sum the M symmetric matrices to obtain a matrix representation of B_M.

3. Compute the eigenvalues of this operator.

The eigenvalues of the finite-dimensional approximation to B_M operator are all negative as expected (since it is the sum of M symmetric negative semi-definite matrices). Figure 4.3 depicts the sorted magnitudes of the eigenvalues for varying M values. As anticipated, the scenario with $M = 1$ exhibits all eigenvalues clustered near zero, confirming the ill-conditioned nature of the operator. Increasing M to 2 results in a modest upward shift of

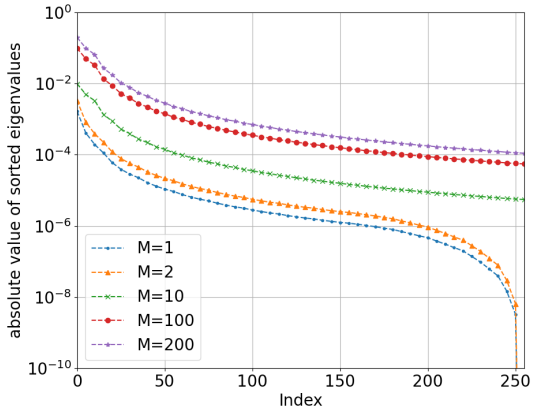

(a) Regularised Boussinesq model

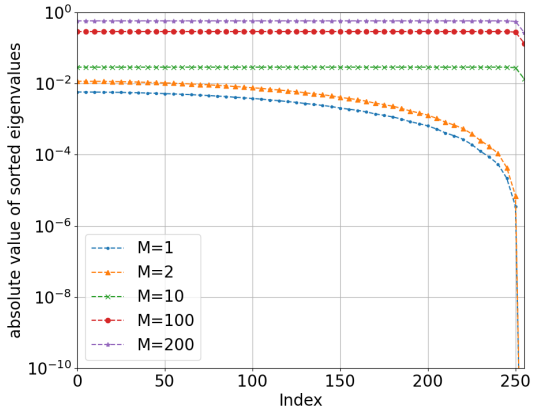

(b) Regularised Boussinesq−Whitham model

Figure 4.3: Absolute values of sorted eigenvalues from the operator on the left-hand side of equation (4.22) for both models. In this context, $q^{(j)} = 0.1\sin(x - t_j)$, where $x \in [0, 2\pi]$ and $t_j = 2\pi j/M$ with $j = 1, 2, \ldots, M$. The index of the sorted eigenvalue is represented along the horizontal axis. Each curve represents total number of time instances (M) used in the analysis, as indicated in the legend. Markers on the curves serve for visual distinction and don't imply specific data points. Both models depict 256 eigenvalues, corresponding to 256 grid points in the x-axis.

the eigenvalues, but they remain critically close to zero. However, introducing more time instances acts as a form of regularisation. Larger M values lead to a significant boost in eigenvalue magnitudes, particularly evident in the regularised Boussinesq−Whitham model, where the trend plateaus at certain M values. Notably, the regularised Boussinesq model demonstrates a faster decay in eigenvalue magnitudes despite some improvement with $M > 1$. This difference can be attributed to the inherent differences in the operators' (sum of M compact operators in case of regularised Boussinesq model) compactness properties.

Our previous analysis focused on a fixed spatial resolution of 256 grid points. Let's investigate how modifying this resolution affects the eigenvalue spectrum. Figure 4.4 presents the absolute values of sorted eigenvalues for the regularised Boussinesq model at various grid sizes ($128, 256, 512$, and 1024) while keeping M fixed at 200. For the regularised Boussinesq model, increasing the resolution in x (while fixing M) leads to smaller minimum eigenvalues (in term of absolute values). This observation implies that if the resolution in x were increased, one may require higher values of M to achieve a similar amount of regularisation for the regularised Boussinesq model. In other words, the benefit of using a finer grid is offset by the need for more time instances to overcome the persistent ill-conditioning.

However, this scenario is different for regularised Boussinesq−Whitham model. Here, the operator is not compact, and the primary culprit of ill-posedness lies in the zeros of $\mathcal{P}q_x$. For this model, larger M values offer a powerful regularisation tool, especially

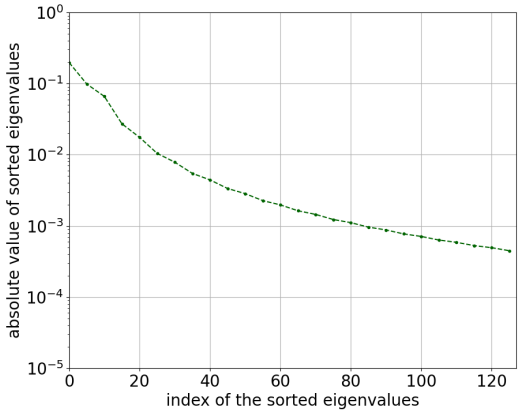

(a) Grid size = 128

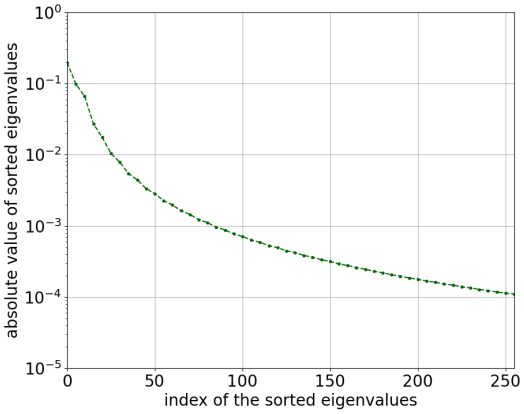

(b) Grid size = 256

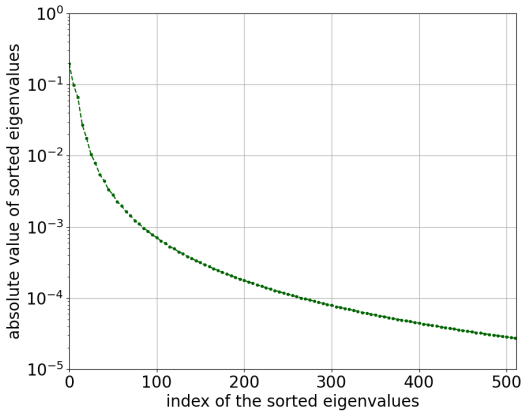

(c) Grid size = 512

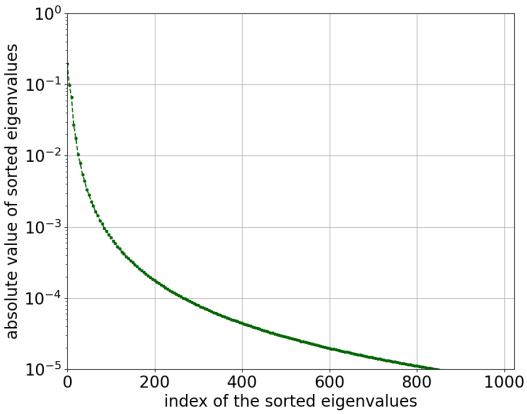

(d) Grid size = 1024

Figure 4.4: Eigenvalues for different values of grid size with fixed $M = 200$ for regularised Boussinesq model. For larger grid size, eigenvalues are smaller so this value of M might not be enough to invert the reconstruction operator. Thus, we might need higher values of M if we are inverting the reconstruction operator if we are working with higher resolution.

when the zeros of $\mathcal{P}q_x$ are not fixed in time. Notably, this trend holds true even at higher resolutions in x as shown in Figure 4.5, further highlighting the effectiveness of multi-time data for the regularised Boussinesq−Whitham model. We emphasise that these conclusions are contingent on the choice of velocity potential and are intended to give some intuition about the choice of the parameter M as well as the grid size in x. For more complicated velocity potentials, the underlying relationships between spectra and M/(grid size) may be also be complicated.

The accuracy of bottom profile reconstruction is sensitive to the decay rate of the eigenvalues of the associated operator. When eigenvalues decrease rapidly, the reconstruction becomes increasingly susceptible to amplification of even minor discrepancies in the provided data (η, η_t, q). This phenomenon arises due to the inherent sensitivity of the reconstruction process (inverting the reconstruction operator) to noise in the data.

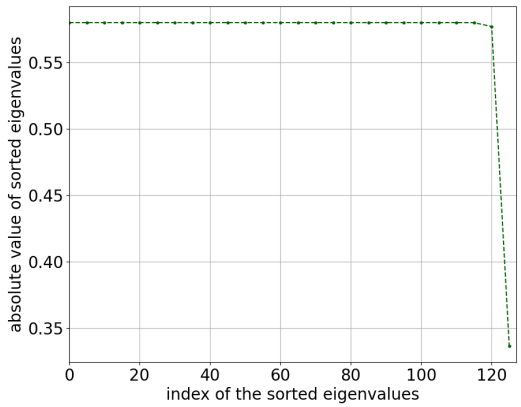

(a) Grid size = 128

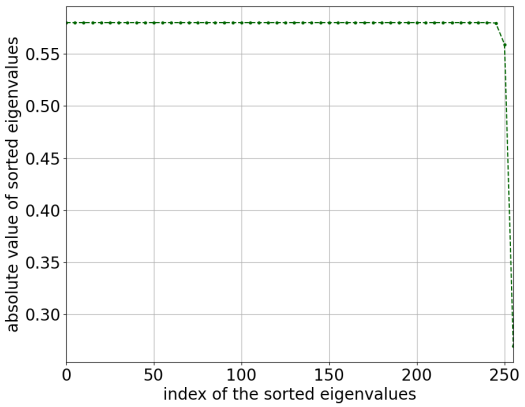

(b) Grid size = 256

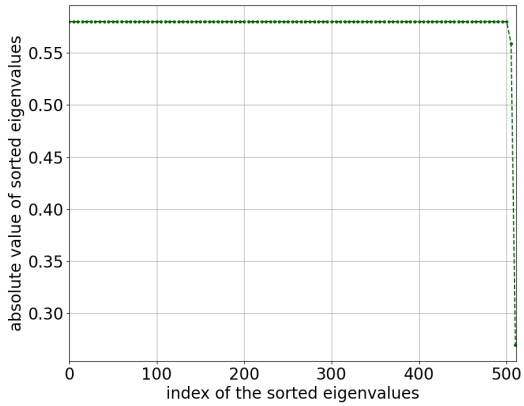

(c) Grid size = 512

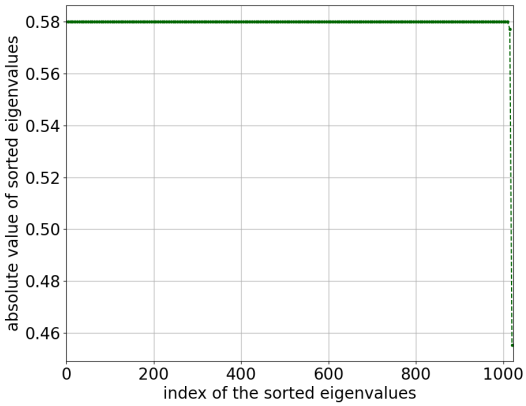

(d) Grid size = 1024

Figure 4.5: Eigenvalues for different values of grid size with fixed $M = 200$ for regularised Boussinesq−Whitham model. Regardless of increasing spatial resolution, the eigenvalues consistently stay away from zero for $M = 200$ in this case.

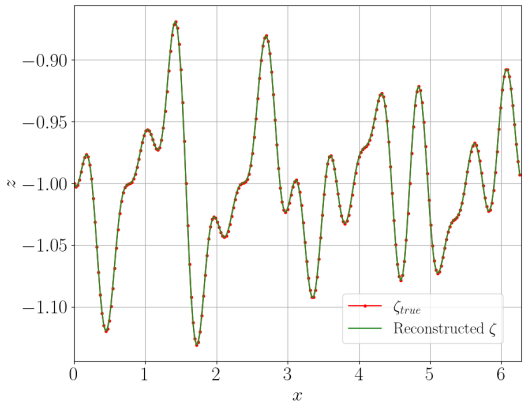

(a) Regularised Boussinesq model

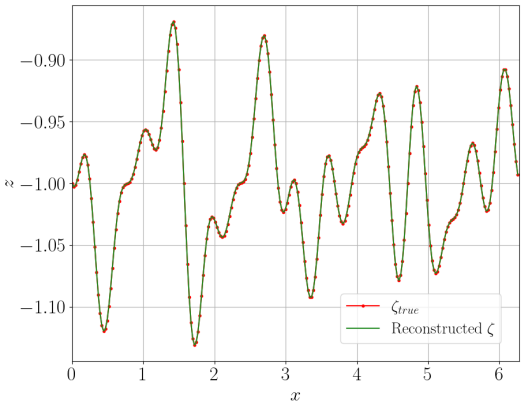

(b) Regularised Boussinesq−Whitham model

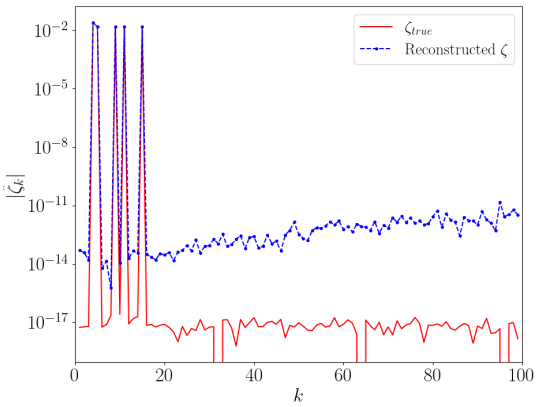

(c) Regularised Boussinesq model

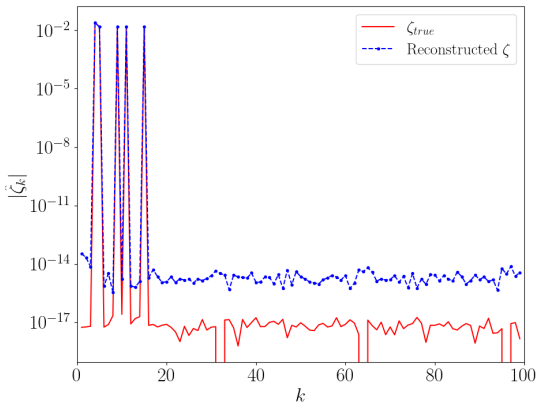

(d) Regularised Boussinesq−Whitham model

Figure 4.6: Reconstruction of multi-sine wave profile (4.24) for both the models. Top-left 4.6a and top-right 4.6b compares the true (solid green) and computed (red dots) bottom surfaces. Bottom-left 4.6c and bottom-right 4.6d depict mode by mode comparisons of the amplitude in Fourier space of the true (solid red line) and reconstructed (blue dots) solutions.

Therefore, the decay rate of the eigenvalues serves as a critical indicator of the data quality (data to be consistent with the model equations) required for achieving accurate bottom profile reconstructions.

$$\text{Multi-sine wave profile} \ : \quad \zeta = -0.12\sin(3x)\cos(2x)\sin(10x) + 0.05\sin(4x). \tag{4.24}$$

To assess our bottom profile reconstruction method, we conducted controlled experiments utilising simulated data extracted from forward simulations of the model equations (3.25-3.26). The bottom-profile, referred as "Multi-sine wave profile" is defined in equation (4.24). Figures 4.6 depict the reconstruction results for both the regularised Boussinesq and regularised Boussinesq−Whitham models. Comparison with the ground

truth (solid green line) reveals highly accurate recoveries, represented by the red lines with filled-circle markers in Figures 4.6a and 4.6b, for the regularised Boussinesq model and the regularised Boussinesq−Whitham model respectively. Figures 4.6c and 4.6d delve deeper into the accuracy comparison, where the absolute values of Fourier modes for both the models demonstrate minimal discrepancies between the true profile (solid red line) and the recovered profile (dashed blue line). The near-machine-precision errors achieved underscore the effectiveness of our method under ideal conditions.

For this recovery process, the data for η and q was generated using the numerical simulations of the forward problem (3.25-3.26). The initial condition used for the forward problem simulation are specified by equations (3.45-3.46) and the shallow-water model is solved numerically to obtain the solution (η, q). A critical step involved calculating the time derivative η_t, where we employed a fourth-order five-point finite-difference stencil in time for its inherent high accuracy. This choice ensures accuracy for η_t up to machine precision, equivalent to computing the right-hand side of equation (3.25). Leveraging data collected from 200 time points within the simulation (and thus $M = 200$ in the definition of B_M), we computed the left hand side and right hand side of the equation (4.22) and then solved this linear equation to determine ζ numerically.

We assess the accuracy of our reconstructed bottom-profile using two relative error metrics:

1. Overall depth error E_b: This measures the relative error in the total depth, including the baseline of $z = -1$ calculated as

$$\mathrm{E}_b = \frac{\|(1+\zeta_r) - (1+\zeta)\|_2}{\|1+\zeta\|_2}, \tag{4.25}$$

   where ζ_r is the reconstructed profile and ζ is the true profile.

2. Profile error E_p: This measures the relative error in the deviation from the baseline $z = -1$ calculated as

$$\mathrm{E}_p = \frac{\|\zeta_r - \zeta\|_2}{\|\zeta\|_2}. \tag{4.26}$$

When using data (η, η_t, q_x) consistent with the respective model equations, we achieve exceptional accuracy for the reconstructed bottom profile in Figure 4.6. The error values for this recovery are as follows:

Regularised Boussinesq model: $\mathrm{E}_b \approx 10^{-12}$ and $\mathrm{E}_p \approx 10^{-10}$.

Regularised Boussinesq−Whitham model: $\mathrm{E}_b \approx 10^{-12}$ and $\mathrm{E}_p \approx 10^{-10}$.

These extremely low error values demonstrate the impressive accuracy of our method. Utilising a second-order three-point stencil for calculating η_t also results in successful recovery but has a higher E_b value (around 10^{-8}) compared to the fourth-order stencil.

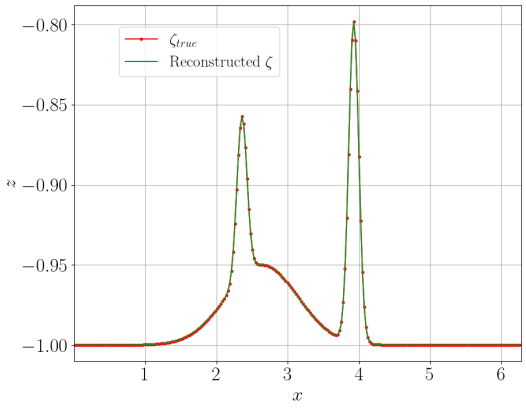

(a) Regularised Boussinesq model

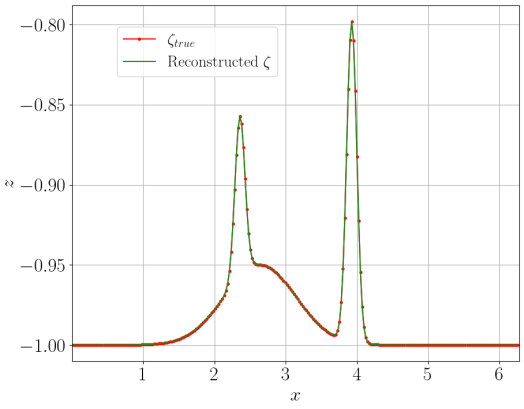

(b) Regularised Boussinesq−Whitham model

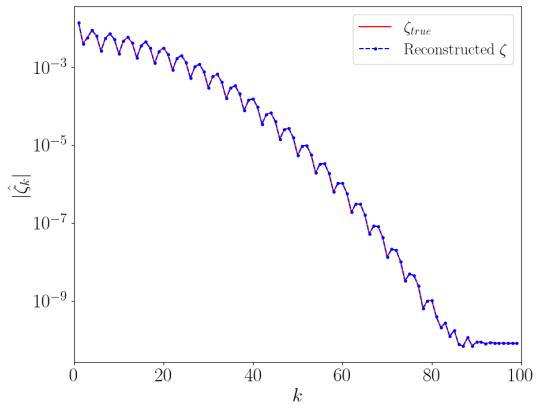

(c) Regularised Boussinesq model

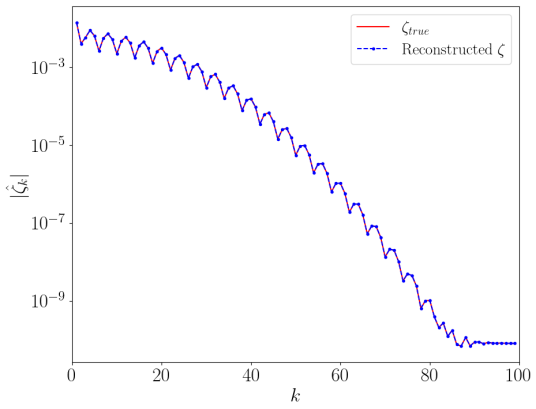

(d) Regularised Boussinesq−Whitham model

Figure 4.7: Reconstruction of localised bottom feature profile (4.27) for both the models. Top-left 4.7a and top-right 4.7b compares the true (solid green) and computed (red dots) bottom surfaces. Bottom-left 4.7c and bottom-right 4.7d depict mode by mode comparisons of the amplitude in Fourier space of the true (solid red line) and computed (blue dots) solutions.

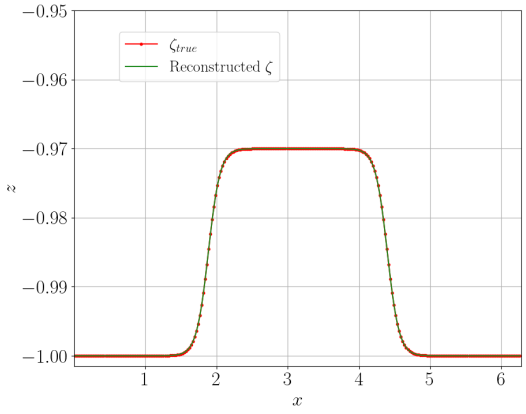

(a) Regularised Boussinesq model

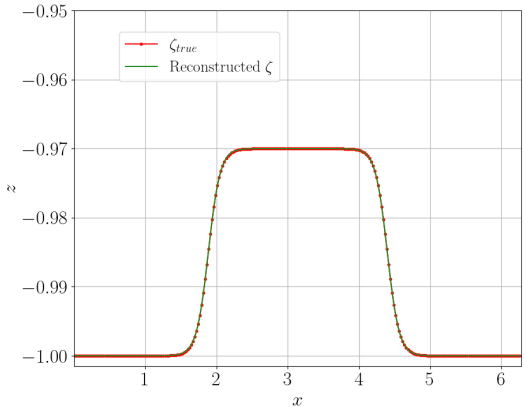

(b) Regularised Boussinesq−Whitham model

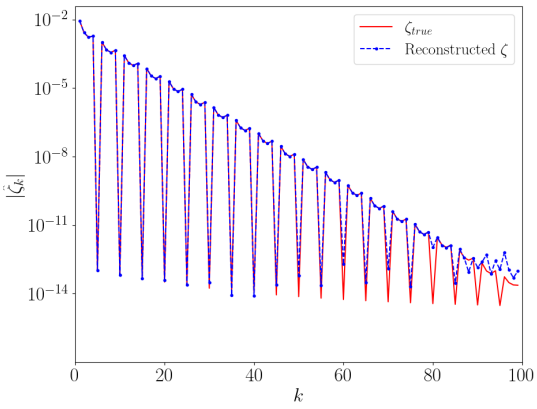

(c) Regularised Boussinesq model

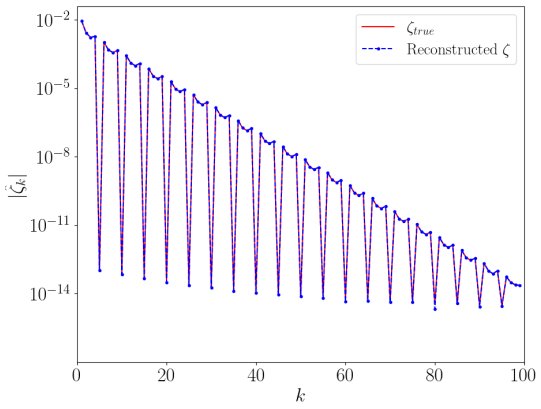

(d) Regularised Boussinesq−Whitham model

Figure 4.8: Reconstruction for sandbar profile (4.27) for both the models. Top-left 4.8a and top-right 4.8b compares the true (solid green) and computed (red dots) bottom surfaces. Bottom-left 4.8c and bottom-right 4.8d depict mode by mode comparisons of the amplitude in Fourier space of the true (solid red line) and computed (blue dots) solutions.

Additionally, we present examples showcasing the recovery of two types of bottom profiles:

$$\text{Localised bottom feature profile}: \quad \zeta = -0.1e^{-100(x-x_1)^2} - 0.05e^{-2(x-x_2)^2} - 0.2e^{-100(x-x_3)^2}, \tag{4.27}$$

$$x_1 = 3\pi/4,\ x_2 = 1.12x_1,\ x_3 = 5\pi/4.$$

$$\text{Sandbar profile}: \quad \zeta = -0.015\tanh(6(x-0.6\pi)) + 0.015\tanh(6(x-1.4\pi)), \tag{4.28}$$

- **Localised bottom feature profile:** The profile, defined in equation (4.27), is like a combination of two bumps on a flat surface. This profile was recovered with impressive accuracy by both the models (green versus red lines in Figure 4.7). Even individual elements in the frequency domain (bottom plots) closely match the true profile, further confirming the accuracy. The relative errors E_b and E_p around 10^{-11} and 10^{-9} for both models support these observations.

- **Sandbar profile:** Now consider a wider, smoother underwater ridge given by equation (4.28). Recovery for this profile is also impressive for both the models as shown in top-left and top-right of Figure 4.8 for both the models. Also, it shows that the regularised Boussinesq−Whitham model (bottom right) outperforms the regularised Boussinesq model (bottom left) in recovering this profile. This is because the reconstruction operator in case of regularised Boussinesq model is less effective, potentially introducing numerical errors (due to it having smaller eigenvalues). Nonetheless, both models achieve commendable accuracy, with E_b values around 10^{-14} and 10^{-12}, and E_p values around 10^{-12} and 10^{-10}, for regularised Boussinesq−Whitham model and regularised Boussinesq model respectively.

For both of these recoveries, we extract (η, q) data from numerical simulations of the respective model equations, utilising initial conditions $\eta_0 = 0.1\cos(x)$ and $q_0 = 0.1\sin(x)$. In conclusion, our findings show that both the models can achieve successful recovery when data from forward model is consistent with the model equations.

Sensitivity of Bottom-profile Reconstruction to q_x Errors: Our investigations show that even minor errors in the q_x, as low as 1% relative L^2-norm error, led to substantial errors in the reconstructed bottom-profile. This is illustrated by the yellow and cyan dashed lines in Figures 4.9. Note that the method for introducing error into q_x is explained in Remark 6 in Section 6.1. The relative depth errors (E_b) associated with these reconstructions ranged from 4% to 7% with even less than 1% L^2−norm relative-error in q_x, indicating considerable deviation from the true profiles. Despite the implementation of regularisation techniques, the method remains sensitive to the errors in q_x. This highlights the challenges in fully mitigating error propagation through regularisation alone.

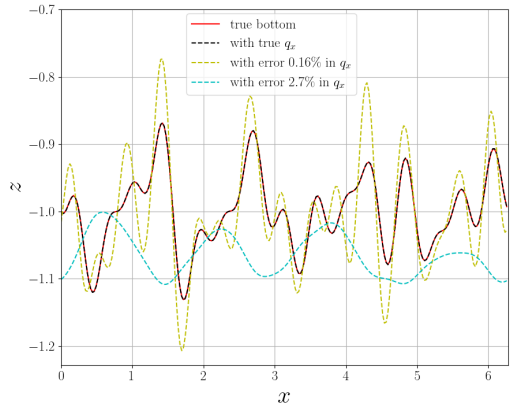

(a) Regularised Boussinesq model

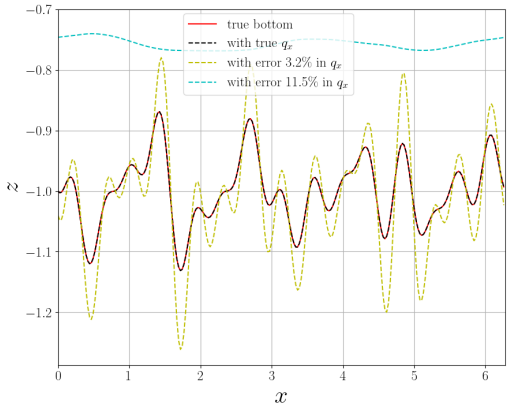

(b) Regularised Boussinesq−Whitham model

Figure 4.9: Reconstruction of multi-sine wave profile (4.24) for both the models using reconstruction equation (4.22) with an erroneous value for q_x with relative error percentages indicated in the legend. The construction of these inaccurate q_x profiles is explained in Section 6.1. Note even a small amount relative error can lead to inaccurate reconstruction. The error between the true profile (solid red line) and the reconstruction using the true q_x (dashed black line) is below machine precision.

For the regularised Boussinesq model, q_x errors exceeding a few percent were excluded from analysis due to the resulting reconstructions being too severely distorted to visualise effectively on a single plot. The regularised Boussinesq−Whitham model demonstrated greater robustness to q_x errors compared to the regularised Boussinesq model. This enhanced resilience can be attributed to the slower decay in the magnitude of its eigenvalues, suggesting better stability under perturbations.

Our exploration of a Tikhonov-based regularisation scheme was unsuccessful. These methods needed considerable tuning of the regularisation parameter which was particular to each bottom-profile and we were unable to find a systematic way to do so.

Chapter 5

VELOCIMETRY— THE OBSERVER MODEL

This chapter addresses the problem of inferring the surface velocity $q_x(x,t)$ for a dynamical system given the measured surface displacement function $\eta(x,t)$ and pre-specified bottom boundary profile $\zeta(x)$. It is crucial to acknowledge that assuming a priori knowledge of ζ contradicts the ultimate goal of determining ζ itself of this thesis. This chapter serves as an intermediate step, providing insights into q_x retrieval with a known ζ, while Chapter 6 will explore techniques for determining ζ and q_x simultaneously given only η.

5.1 The Observer Model for Velocimetry

In our observer design, we introduce $\tilde{\eta}$ and $\tilde{q}$ as the observer variables corresponding to the true solution η and q of the problem (3.25-3.26). We propose the following observer dynamics:

$$\tilde{\eta}_t = \omega^2\tilde{q} - \mathcal{P}\partial_x\big((\tilde{\eta}+\zeta)\,(\mathcal{P}\tilde{q}_x)\big) - \lambda(\tilde{\eta}-\eta), \tag{5.1}$$

$$\tilde{q}_t = -\tilde{\eta} - \frac{1}{2}\,(\mathcal{P}\tilde{q}_x)^2 - \nu(\tilde{\eta}-\eta), \tag{5.2}$$

where λ, ν are the observer parameters and ζ represents the known bottom boundary profile. Our goal is to recover the surface velocity $q_x(x,t)$. We aim to simulate equations (5.1-5.2) starting from any arbitrary initial condition for $\tilde{\eta}, \tilde{q}$ and our goal is that $\tilde{q}_x$ converges to q_x as $t \to \infty$. Hence, we will determine suitable choices for λ and ν such that $\tilde{q}_x \to q_x$ as $t \to \infty$.

We define the error functions associated with the surface displacement and surface velocity potential as $\eta^e = \tilde{\eta} - \eta$ and $q^e = \tilde{q} - q$ respectively. Furthermore, let $q_x^e = \tilde{q}_x - q_x$ denote the error function in the surface velocity. Then subtracting the shallow-water model equations (3.25-3.26) from the observer equations (5.1-5.2), we obtain the evolution

equation for the error functions:

$$\eta_t^e = -\lambda\eta^e + \omega^2 q^e - \mathcal{P}\partial_x\left(\zeta \mathcal{P} q_x^e\right) - \mathcal{P}\partial_x\left((\tilde{\eta}\mathcal{P}\tilde{q}_x - \eta\mathcal{P}q_x)\right), \tag{5.3}$$

$$q_t^e = -(1+\nu)\eta^e + \frac{1}{2}\left[(\mathcal{P}q_x)^2 - (\mathcal{P}\tilde{q}_x)^2\right]. \tag{5.4}$$

We now show that the linear constant coefficient parts of the above error equations (5.3-5.4) give rise to solutions that decay exponentially to zero as t tends to infinity when the observer parameters λ and μ are chosen appropriately.

Theorem 3. *For any positive number d, there exist real numbers λ and ν such that the solution to*

$$\eta_t^e = -\lambda\eta^e + \omega^2 q^e, \tag{5.5}$$

$$q_t^e = -(1+\nu)\eta^e, \tag{5.6}$$

with periodic boundary conditions satisfies

$$\|\eta^e\|_2 \leq Ce^{-dt}, \quad \|q_x^e\|_2 \leq Ce^{-dt},$$

where C is a constant that depends on the initial condition.

Proof. The equations (5.5-5.6) in Fourier space can be written as

$$\frac{d}{dt}\begin{bmatrix} \eta_k^e \\ q_k^e \end{bmatrix} = \begin{bmatrix} -\lambda & \omega^2(k) \\ -(1+\nu) & 0 \end{bmatrix}\begin{bmatrix} \eta_k^e \\ q_k^e \end{bmatrix} \quad \text{for all } k.$$

Note that $\omega^2(k)$ is zero if and only if $k = 0$ for both of our models. Therefore, we will solve for two cases differently: when $k = 0$ and when $k \neq 0$.

Case 1. $k = 0$ (zero wavenumber): The error system becomes:

$$\frac{d}{dt}\begin{bmatrix} \eta_0^e \\ q_0^e \end{bmatrix} = \begin{bmatrix} -\lambda & 0 \\ -(1+\nu) & 0 \end{bmatrix}\begin{bmatrix} \eta_0^e \\ q_0^e \end{bmatrix}.$$

The eigenvalues of the coefficient matrix are $-\lambda$ and 0. Solving the system using eigenfunctions:

$$\begin{bmatrix} \eta_0^e \\ q_0^e \end{bmatrix} = \begin{bmatrix} e^{-\lambda t} & \lambda e^{-\lambda t} \\ 1 + \nu\left(e^{-\lambda t} - 1\right)/\lambda & 1 \end{bmatrix}\begin{bmatrix} \eta_0^e(0) \\ q_0^e(0) \end{bmatrix}.$$

Thus, $\eta_0^e \to 0$ exponentially as $t \to \infty$ due to the negative exponential term, whereas q_0^e does not necessarily approach zero due to the constant term. However, this error remains bounded.

Case 2. $k \neq 0$ (non-zero wavenumber): The error system is:

$$\frac{d}{dt}\begin{bmatrix} \eta_k^e \\ q_k^e \end{bmatrix} = \begin{bmatrix} -\lambda & \omega_k^2 \\ -(1+\nu) & 0 \end{bmatrix}\begin{bmatrix} \eta_k^e \\ q_k^e \end{bmatrix}.$$

The characteristic equation of the coefficient matrix is:

$$x^2 + \lambda x + \omega_k^2(1+\nu) = 0.$$

Then the eigenvalues are:

$$\frac{-\lambda \pm \sqrt{\lambda^2 - 4\omega_k^2(1+\nu)}}{2}.$$

We desire exponential decay in the error functions. Ensuring a decay rate of $-\lambda/2$ requires the term $\sqrt{\lambda^2 - 4\omega_k^2(1+\nu)}$ to be a purely imaginary term. For both of our models, $\omega_k^2 > 0$ for $k \neq 0$, and it is increasing function of $|k|$. Therefore, we need to ensure that:

$$\lambda^2 - 4\omega_k^2(1+\nu) < 0.$$

This can be achieved by choosing an appropriate value for the observer parameter ν such that:

$$\nu > \begin{cases} \dfrac{\lambda^2}{4}\dfrac{1+\mu^2/2}{1+\mu^2/6} - 1 & \text{for regularised Boussinesq model (3.27)} \\ \dfrac{\lambda^2}{4}\dfrac{\mu}{\tanh(\mu)} - 1 & \text{for regularised Boussinesq}-\text{Whitham model (3.30)} \end{cases} \tag{5.7}$$

Denoting the purely imaginary term $\sqrt{\lambda^2 - 4\omega_k^2(1+\nu)}/2$ by ic_k for simplicity and setting $d = \lambda/2$, we can rewrite the eigenvalues as $-d + ic_k$ and $-d - ic_k$. Then, the solution of the error system in this case is given by:

$$\begin{bmatrix} \eta_k^e \\ q_k^e \end{bmatrix} = e^{-dt}\begin{bmatrix} \cos(c_k t) - (d/c_k)\sin(c_k t) & (d^2 + c_k^2/c_k(1+\nu))\sin(c_k t) \\ -((1+\nu)/c_k)\sin(c_k t) & \cos(c_k t) + (d/c_k)\sin(c_k t) \end{bmatrix}\begin{bmatrix} \eta_k^e(0) \\ q_k^e(0) \end{bmatrix}. \tag{5.8}$$

This demonstrates that we achieve a decay rate of d for all modes of η^e and all non-zero modes of q^e (and therefore all the modes of q_x^e has a decay date d). This implies exponential decay of the surface displacement and surface velocity errors to zero. □

Our analysis demonstrates that the chosen observer with appropriate parameters λ and ν achieves an exponentially fast decay rate (denoted as d) in the errors associated with surface displacement η and surface velocity q_x for the linear constant-coefficient model

(5.1-5.2). However, the analysis for $k = 0$ reveals that the error in velocity potential q does not exhibit the same exponential decay. We also note this more directly from the integral of equations (5.5-5.6):

$$\partial_t \int \eta^e = -\lambda \int \eta^e, \quad \partial_t \int q^e = -(1+\nu) \int \eta^e,$$

and observe that the mean mode of η^e vanishes exponentially, but the initial error in q^e is never eliminated. This implies that while the observer effectively recovers surface displacement and velocity information, it does not retrieve the full velocity potential.

From a physical standpoint, this limitation aligns with the practical interest in surface displacements and velocities rather than the velocity potential, the latter being a quantity that cannot be directly measured. Indeed recovering surface dynamics is often the primary goal in many applications.

5.2 Convergence of Linear Observer

In the previous section, we established exponential decay of errors for the constant-coefficient linear portion of equations (5.1-5.2), disregarding the term $\mathcal{P}\partial_x(\zeta\,\mathcal{P}q^e_x)$. While this term isn't constant-coefficient, it remains linear. We now demonstrate that the achieved error decay extends to the full linear system encompassing this term.

Theorem 4. *Let $\zeta \in H^1[0, 2\pi]$ and let (η^e, q^e) be a smooth solution to the linearised error equation*

$$\eta^e_t = \omega^2 q^e - \mathcal{P}\partial_x(\zeta\,\mathcal{P}q^e_x) - \lambda\eta^e, \tag{5.9}$$

$$q^e_t = -(1+\nu)\eta^e, \tag{5.10}$$

for the corresponding shallow-water model. If λ, ν are chosen so that the conclusion of Theorem 3 holds, then there exists $\epsilon > 0$ and $m > 0$ such that for all $\|\zeta\|_{H^1} \leq \epsilon$ we have

$$\|\eta^e(t)\|_2 + \|q^e_x(t)\|_2 \leq Ce^{-mt}, \quad \text{for all } t \geq 0,$$

where the constant C depends on the initial conditions $\eta^e(0), q^e(0)$.

Proof. Since $\|q^e_t(t)\|_2 = (1+\nu)\|\eta^e(t)\|_2$, to prove the theorem it suffices to show that

$$\|q^e_x(t)\|_2 \leq C_1 e^{-mt}, \quad \text{and} \quad \|q^e_t(t)\|_2 \leq C_2 e^{-mt}.$$

We first combine the equations for η^e and q^e into a single equation for q^e as follows:

$$q^e_{tt} + \lambda q^e_t + (1+\nu)\omega^2 q^e = (1+\nu)\mathcal{P}\partial_x(\zeta\mathcal{P}q^e_x).$$

Following the proof of Theorem 3 for a given $\lambda > 0$ we can find ν such that $\Omega_k := \sqrt{4(1+\nu)\omega_k^2 - \lambda^2}$ is a positive real number for all $k = \pm 1, \pm 2, \ldots$. Note that for either shallow-water wave model, Ω_k is a monotonically increasing function of k and $\Omega_k \to \infty$ as $k \to \infty$. It then follows that

$$q^e(t) = e^{-\lambda t/2} {\sum_{k=-\infty}^{\infty}}' e^{ikx} \left(e^{i\Omega_k t}\alpha_k + e^{-i\Omega_k t}\beta_k \right) + e^{-\lambda t/2}\alpha_0 + \beta_0$$
$$+ (1+\nu) \int_0^t e^{-\lambda(t-s)/2} {\sum_{k=-\infty}^{\infty}}' e^{ikx} \frac{\sin(\Omega_k(t-s))}{\Omega_k} \mathcal{F}_k \left[\mathcal{P}\partial_x(\zeta \mathcal{P} q_x^e(s)) \right] \, ds, \qquad (5.11)$$

where α_k, β_k are complex numbers related to the Fourier coefficients of the initial conditions. Differentiating the above expression in x and taking the L^2-norm we obtain

$$\|q_x^e(t)\|_2 \le e^{-\lambda t/2}(\|\alpha_x\|_2 + \|\beta_x\|_2) + \frac{1+\nu}{\Omega_1} \int_0^t e^{-\lambda(t-s)/2} \|\partial_x \mathcal{P}\partial_x(\zeta \mathcal{P} q_x^e(s))\|_2 \, ds. \qquad (5.12)$$

Recall that $\mathcal{P}$ maps L^2 elements into H^1. Hence if $q_x \in L^2$ then $\zeta \mathcal{P} q_x \in H^1$ by the algebra property for functions in H^1. Further recall that $\mathcal{P} : L^2 \to L^2$ is a bounded operator. Lastly, since $\mathcal{P}\partial_x : L^2 \to L^2$ is a bounded operator $\mathcal{P}\partial_x : H^1 \to H^1$ is also bounded. Using these we have

$$\|\partial_x \mathcal{P}\partial_x(\zeta \mathcal{P} q_x(s))\|_2 \le \|\mathcal{P}\partial_x(\zeta \mathcal{P} q_x(s))\|_{H^1} \le \frac{1}{\mu^j} \|\zeta \mathcal{P} q_x\|_{H^1} \le \frac{\|\zeta\|_{H^1}}{\mu^j} \|q_x\|_2,$$

where j depends on the shallow-water model under consideration. Thus we obtain

$$\|q_x^e(t)\|_2 \le e^{-\lambda t/2}(\|\alpha_x\|_2 + \|\beta_x\|_2) + \frac{(1+\nu)\|\zeta\|_{H^1}}{\Omega_1 \mu^j} \int_0^t e^{-\lambda(t-s)/2} \|q_x(s)\|_2 \, ds. \qquad (5.13)$$

Using Grönwall's inequality for the quantity $e^{\lambda t/2}\|q_x^e(t)\|_2$, we obtain

$$q_x^e(t)\|_2 \le (\|\alpha_x\|_2 + \|\beta_x\|_2) e^{-m_1 t}, \quad \text{where } m_1 = \frac{\lambda}{2} - \frac{(1+\nu)\|\zeta\|_{H^1}}{\Omega_1 \mu^j},$$

and hence if $\|\zeta\|_{H^1}$ is sufficiently small, $m_1 > 0$ and $\|q_x^e(t)\|_2$ decays exponentially in time.

The proof for exponential decay of $\|q_t^e(t)\|_2$ is similar. We first rewrite the expression for $q^e(t)$ in the following equivalent way

$$q^e(t) = e^{-\lambda t/2} {\sum_{k=-\infty}^{\infty}}' e^{ikx} \left(e^{i\Omega_k t}\alpha_k + e^{-i\Omega_k t}\beta_k \right) + e^{-\lambda t/2}\alpha_0 + \beta_0$$
$$+ (1+\nu) \int_0^t e^{-\lambda s/2} {\sum_{k=-\infty}^{\infty}}' e^{ikx} \frac{\sin(\Omega_k s)}{\Omega_k} \mathcal{F}_k \left[\mathcal{P}\partial_x(\zeta \mathcal{P} q_x^e(t-s)) \right] \, ds. \qquad (5.14)$$

This follows from the convolution identity

$$\int_0^t g(t-s)h(s)ds = \int_0^t g(s)h(t-s)ds \text{ for all sufficiently nice functions } g, h. \tag{5.15}$$

Differentiating in t leads to

$$\begin{aligned} q_t^e(t) = e^{-\lambda t/2} \sum_{k=-\infty}^{\infty}{}' e^{ikx} \left(e^{i\Omega_k t} \left(-\frac{\lambda}{2} + i\Omega_k \right) \alpha_k + e^{-i\Omega_k t} \left(-\frac{\lambda}{2} - i\Omega_k \right) \beta_k \right) \\ - \frac{\lambda}{2} e^{-\lambda t/2} \alpha_0 + (1+\nu) e^{-\lambda t/2} \sum_{k=-\infty}^{\infty}{}' e^{ikx} \frac{\sin(\Omega_k t)}{\Omega_k} \mathcal{F}_k \left[\mathcal{P}\partial_x (\zeta \mathcal{P} q_x^e(0)) \right] \\ + (1+\nu) \int_0^t e^{-\lambda s/2} \sum_{k=-\infty}^{\infty}{}' e^{ikx} \frac{\sin(\Omega_k s)}{\Omega_k} \mathcal{F}_k \left[\mathcal{P}\partial_x (\zeta \mathcal{P}\partial_x q_t^e(t-s)) \right] \, ds. \end{aligned} \tag{5.16}$$

Using the convolution identity in reverse for the last line leads to

$$\begin{aligned} q_t^e(t) = e^{-\lambda t/2} \sum_{k=-\infty}^{\infty}{}' e^{ikx} \left(e^{i\Omega_k t} \left(-\frac{\lambda}{2} + i\Omega_k \right) \alpha_k + e^{-i\Omega_k t} \left(-\frac{\lambda}{2} - i\Omega_k \right) \beta_k \right) \\ - \frac{\lambda}{2} e^{-\lambda t/2} \alpha_0 + (1+\nu) e^{-\lambda t/2} \sum_{k=-\infty}^{\infty}{}' e^{ikx} \frac{\sin(\Omega_k t)}{\Omega_k} \mathcal{F}_k \left[\mathcal{P}\partial_x (\zeta \mathcal{P} q_x^e(0)) \right] \\ + (1+\nu) \int_0^t e^{-\lambda (t-s)/2} \sum_{k=-\infty}^{\infty}{}' e^{ikx} \frac{\sin(\Omega_k (t-s))}{\Omega_k} \mathcal{F}_k \left[\mathcal{P}\partial_x (\zeta \mathcal{P}\partial_x q_t^e(s)) \right] \, ds. \end{aligned} \tag{5.17}$$

Estimating the L^2-norm we find

$$\|q_t^e(t)\|_2 \leq e^{-\lambda t/2} \left(\tilde{C} + \frac{(1+\nu)\|\zeta\|_\infty}{\Omega_1 \mu^j} \|q_x^e(0)\|_2 \right) + \frac{(1+\nu)\|\zeta\|_\infty}{\Omega_1 \mu^{2j}} \int_0^t e^{-\lambda (t-s)/2} \|q_t^e(s)\|_2 \, ds. \tag{5.18}$$

where $\tilde{C}$ is a constant depending on the initial conditions. Once again we appeal to Grönwall's inequality to deduce

$$\|q_t^e(t)\|_2 \leq C_2 e^{-m_2 t}, \quad \text{where } m_2 = \frac{\lambda}{2} - \frac{(1+\nu)\|\zeta\|_\infty}{\Omega_1 \mu^{2j}},$$

where C_2 depends on initial conditions (and also on other parameters in the problem). Since $\|\zeta\|_\infty \leq \|\zeta\|_{H^1}$, then for sufficiently small $\|\zeta\|_{H^1}$ we have $m_2 > 0$ and hence obtain the exponential decay of $\|q_t^e(t)\|_2$. Hence the conclusion of the theorem follows. □

For the sake of completeness we also present below a proof of Grönwall's inequality. The version below is slightly more general than the usual one and allows for a 'forcing term' so that the solution need not decay to zero. This more general version is attributed

to Zadiraka [63] in the literature and will be of particular use in Chapter 6.

Lemma 5. *(A simplified version of Zadiraka theorem [63]) Let $u(t)$ be a continuous function that satisfies*

$$|u(t)| \leq |u(0)|e^{-\alpha t} + \int_0^t e^{-\alpha(t-s)}(c|u(s)| + b)\,\mathrm{d}s, \tag{5.19}$$

where a, b, c are all positive constants then

$$|u(t)| \leq |u(0)|e^{-(\alpha-c)t} + \frac{b}{\alpha - c}(1 - e^{-(\alpha-c)t}). \tag{5.20}$$

Proof. Let's define $R(t)$ as follows:

$$R(t) = |u(0)|e^{-\alpha t} + \int_0^t e^{-\alpha(t-s)}(c|u(s)| + b)\,\mathrm{d}s. \tag{5.21}$$

Notice $R(0) = |u(0)|$. Differentiating $R(t)$ and using the inequality $|u(t)| \leq R(t)$, we get

$$R'(t) \leq (c - \alpha)R(t) + b.$$

Multiplying both sides by $e^{(\alpha-c)t}$:

$$e^{(\alpha-c)t}R'(t) \leq (c - \alpha)e^{(\alpha-c)t}R(t) + be^{(\alpha-c)t}.$$

Combining the left-hand side term with the first term on right-hand side, we obtain

$$\frac{d}{dt}\left(e^{(\alpha-c)t}R(t)\right) \leq be^{(\alpha-c)t},$$

which can also be written as

$$\frac{d}{dt}\left(e^{(\alpha-c)t}\left(R(t) - \frac{b}{\alpha - c}\right)\right) \leq 0.$$

Integrating from 0 to t and using fundamental theorem of calculus:

$$e^{(\alpha-c)t}\left(R(t) - \frac{b}{\alpha - c}\right) - R(0) + \frac{b}{\alpha - c} \leq 0.$$

Using $R(0) = |u(0)|$ and simplifying, we obtain

$$R(t) \leq \left(|u(0)| - \frac{b}{\alpha - c}\right)e^{-(\alpha-c)t} + \frac{b}{\alpha - c}.$$

Since $|u(t)| \leq R(t)$, the above inequality gives us the required inequality in equation (5.20). □

Remark. We acknowledge that the cited result from Zadiraka's work [63] typically includes the term $|u(0)|e^{-\alpha t}$ in the literature instead of $|u(0)|e^{-(\alpha-c)t}$. Despite extensive efforts, we were unable to locate the original reference for this variation or independently prove it. Therefore, for the purposes of this thesis, we have opted to utilise a simplified version of the theorem that we successfully proved in the Lemma 5 above. This simplified result, while not directly matching the quoted Zadiraka reference, allows us to proceed with the decay rate analysis within the current context as well as in Chapter 6.

Theorems 3 and 4 imply the observer parameters can be chosen such that the solution to the linear version of the error equations (5.1-5.2) converges exponentially to zero. Thus one can recover the surface velocity given surface displacement observations (and the bottom profile) using the linear observer equations (5.9-5.10). Interestingly, our numerical simulations based on the nonlinear observer equations (5.1-5.2) suggest that the error in the horizontal surface velocity q_x^e does vanish asymptotically in time and hence velocimetry seems possible using the full nonlinear observer model. This warrants further investigation, potentially through analytical techniques or more elaborate numerical experiments. Although we have not worked on proving the convergence rigorously in this thesis, we have shown the results from numerical experiments in Section 5.4.

5.3 Choosing the Observer Parameters

In the preceding section, we established exponential decay in the error terms η^e and q_x^e for certain values of λ and ν (for the linear error equation). In doing so, we assumed that the H^1 norm of the bottom profile was available. Moreover a large H^1 norm for the bottom profile required the observer parameter λ to be proportionately larger. Recall our remark from earlier (when the shallow-water models were derived) that the bottom profile ζ need not have zero-average. In other words, when attempting to reconstruct the bottom profile, we may not even know the average location of the bottom. As a result, H^1 norm of zeta may be large merely due to a large average depth. Thus to choose the observer parameters, we assume we are given some initial estimate of the bottom profile ζ_{init} so that $|\zeta - \zeta_{init}|_{H^1}$ is not too large while still ensuring the exponential decay we desire. Since ζ_{init} is for us to choose as per our convenience, we always take it to be a constant function of x.

Assuming a constant bottom surface $\zeta = \zeta_c$, we can rewrite the linear observer system (5.9-5.10) in terms of η^e, resulting in a second-order partial differential equation as follows:

$$\eta^e_{tt} + \lambda\eta^e_t + (1+\nu)(\omega^2\eta^e - \mathcal{P}\partial_x\big(\zeta_c\,(\mathcal{P}\eta^e_x)\big) = 0.$$

We seek solutions of the form e^{ikx+pt}, where p represents a parameter. This p must satisfy

the characteristic equation:

$$p^2 + \lambda p + (1+\nu)(\omega(k)^2 + k^2\mathcal{P}(k)^2\zeta_c) = 0.$$

Solving for p using the quadratic formula, we obtain two values:

$$p = -\frac{\lambda}{2} \pm \sqrt{\frac{\lambda^2}{4} - k^2(1+\nu)\left(\frac{\omega(k)^2}{k^2} + \zeta_c\mathcal{P}(k)^2\right)}.$$

For both models, the term $k^2\left(\omega(k)^2/k^2 + \zeta_c\mathcal{P}(k)^2\right)$ increases with k. To ensure an exponential decay, we want the term under the square root to be negative for all k, which simplifies to proving that the term under the square root is negative for $k = 1$. If $\zeta_c > 0$, the parameter choice for ν in equation (5.7) from Theorem 3 will suffice. Therefore, for a general surface bottom profile ζ, we should set the constant $\zeta_c = \min(0, \min(\zeta))$. As demonstrated in the previous section, we will have the decay rate of $-\lambda/2$ if we choose

$$(1+\nu) > \left.\frac{\lambda^2}{4(\omega(k)^2 + \zeta_c\mathcal{P}(k)^2)}\right|_{k=1}, \text{ where } \zeta_c = \min(0, \min(\zeta)). \tag{5.22}$$

In the next section, we will use numerical simulations to verify that this parameter selection leads to an effective decay rate for the full nonlinear problem as well.

5.4 Simulation Results

To investigate the time evolution of the observer model (5.1-5.2), we perform numerical simulations by coupling it with the original shallow-water model equations (3.25-3.26). This allows us to obtain the solution for surface displacement $\eta(x,t)$ needed by the observer. Note that we are using periodic boundary conditions. We utilise periodic boundary conditions throughout the simulation.

Simulation Details:

1. **Function Representation:** All relevant functions $\eta, q, \tilde{\eta}, \tilde{q}$, and bottom boundary are expressed by Fourier series with 256 grid points in the x-direction.

2. **Numerical Method:** A pseudospectral method with 2/3-method de-aliasing is employed to simulate the system of four equations.

3. **Time Integration Schemes:**

- **Shallow-Water Model:** A standard explicit fourth-order Runge-Kutta (RK4) scheme with a time step of $\Delta t = 10^{-3}$ (non-dimensional units) is used. The solution for η is recorded at each step.

- **Observer Model:** An RK4 scheme is used, but with a time step of $\Delta t = 2 \times 10^{-3}$. This accounts for the fixed rate 10^{-3} at which the η solution is provided to the observer. Since RK4 requires values at intermediate time steps, the larger time step (as compare to shallow-water model time-step) is necessary.

Recall we defined errors in velocity potential q^e and surface displacement η^e as the difference between the observer's solution ($\tilde{\eta}$ and $\tilde{q}$) and the solution from our shallow-water model (η and q). Figure 5.1 summarises the L^2 norms of these errors over time for both the regularised Boussinesq and regularised Boussinesq−Whitham models. In particular,

- Figures 5.1a and 5.1b show results for a multi-sine wave bottom profile defined by equation (4.24).
- Figures 5.1c and 5.1d present results for a localised feature bottom profile defined by equation (4.27).

These plots also include the error in velocity, $q_x^e = \tilde{q}_x - q_x$, and the predicted decay rate $\lambda/2$ based on our observer design.

In all experiments for this section, we used $\lambda = 6$ and $\nu = 14$, in alignment with the design suggested in equation (5.22). Remarkably, the errors in the full nonlinear observer problem closely align with the predicted decay rate. We speculate the chosen λ effectively counteracts potential error growth arising from nonlinearity. Consistent with expectations, the error in velocity potential q^e does not converge to zero.

The choice of bottom profile did not significantly affect the rate of error decay. However, the errors in surface displacement η and surface velocity q_x do not reach the machine precision level. The saturation value they always reach depends on how often data ($\eta(x,t)$) is recorded from the original model. Lower recording intervals (smaller Δt) lead to lower final errors, as shown in Figure 5.2.

For the simulations, we chose a time step of $\Delta t = 10^{-3}$ (non-dimensional units) for the shallow-water model equations. The observer model used a doubled time step 2×10^{-3} to account for the fixed-rate data supply from the original model and the RK4 scheme's intermediate time-step requirements. We also tested recording the original model solution less frequently (every m time steps), effectively giving the observer model a larger time step $2m\Delta t$. As shown in Figure 5.3, varying m had no significant qualitative impact. To ensure a fair comparison in the plots, we fixed the observer time step at 0.002 and adjusted the forward model's time step accordingly.

These simulations solidify a key finding: with a known bottom boundary ζ, recovering fluid velocity in shallow-water models from surface displacement measurements is achievable. Moreover, the accuracy of this recovered velocity depends on the frequency of measurements taken.

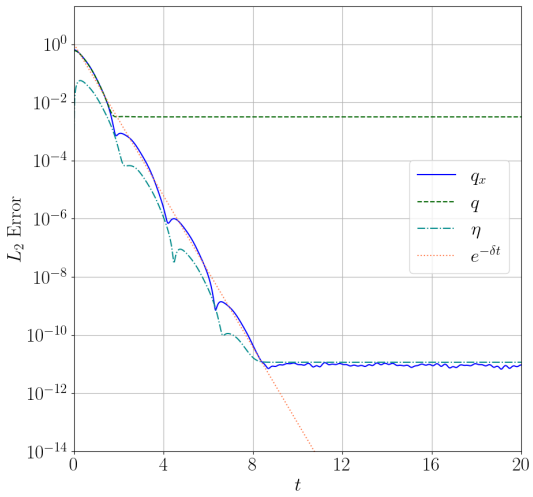

(a) Regularised Boussinesq model corresponding to multi-sine wave profile (4.24)

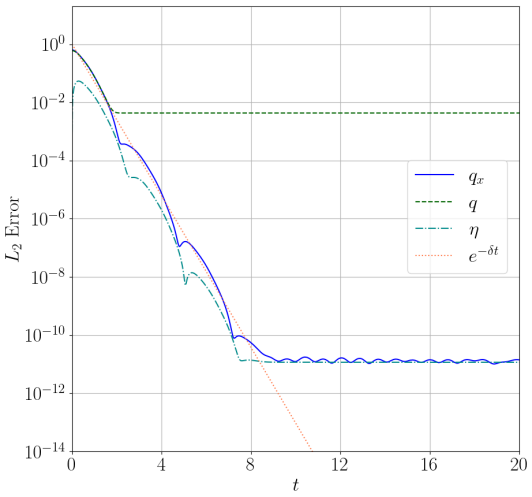

(b) Regularised Boussinesq−Whitham model corresponding to multi-sine wave profile (4.24)

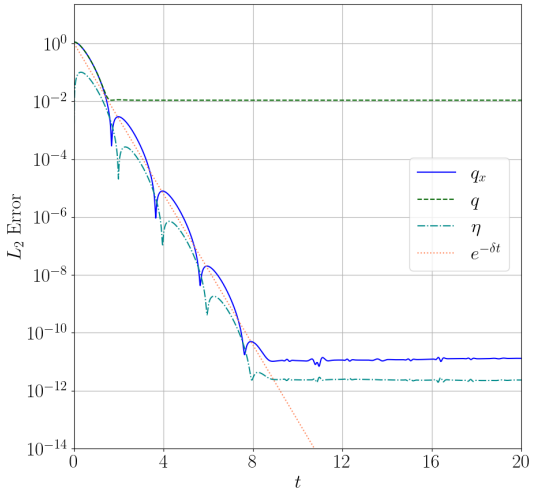

(c) Regularised Boussinesq model corresponding to localised bottom feature profile (4.27)

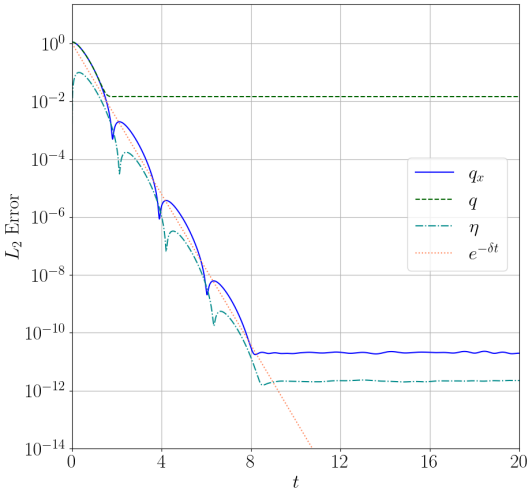

(d) Regularised Boussinesq−Whitham model corresponding to localised bottom feature profile (4.27)

Figure 5.1: Decay of error in solution for the observer model is illustrated for the multi-sine wave profile (4.24) in Figures 5.1a-5.1b and for the localised bottom feature profile (4.27) in Figures 5.1c-5.1d. Observer parameters are set to $\lambda = 6$ and $\nu = 14$, leading to a linear decay rate of $\lambda/2 = 3$, depicted as a dotted red line. The error in η (dash-dot cyan line) and q_x (solid blue line) within the full nonlinear observer problem closely aligns with the anticipated linear decay rate. Meanwhile, the error in q, shown as a dark green dashed line, stabilises at a nonzero value as expected.

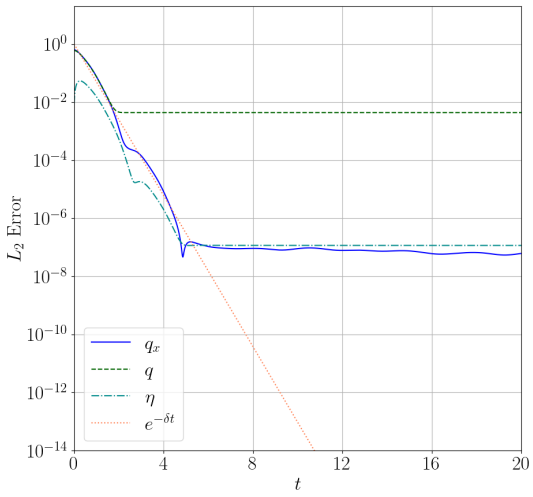

(a) time step $\Delta t = 0.01$

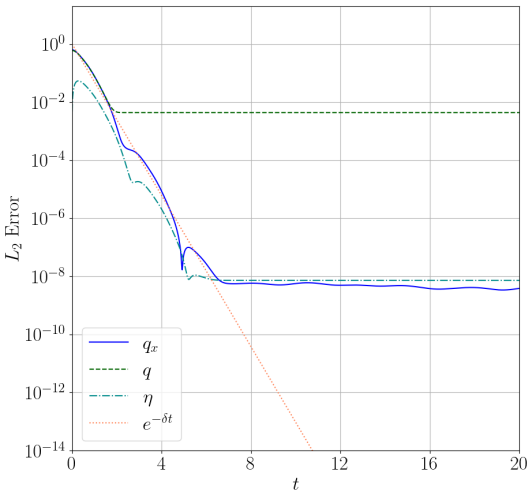

(b) time step $\Delta t = 0.005$

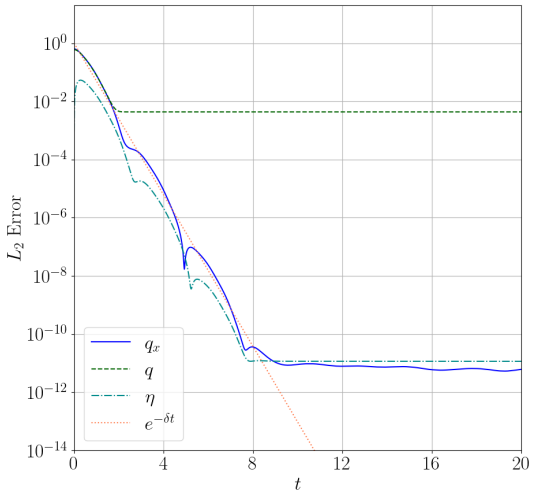

(c) time step $\Delta t = 0.001$

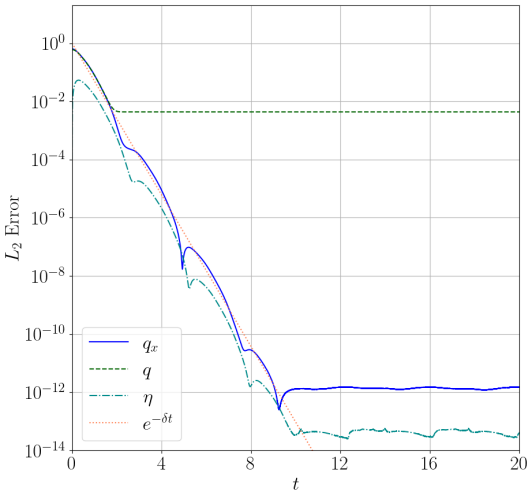

(d) time step $\Delta t = 0.0001$

Figure 5.2: Decay of error in solution for the observer model for the sandbar profile (4.28) in regularised Boussinesq−Whitham model with different value of Δt (frequent measurements of η data from original model). The final asymptotic-in-time errors for η and q_x is smaller when we take Δt smaller.

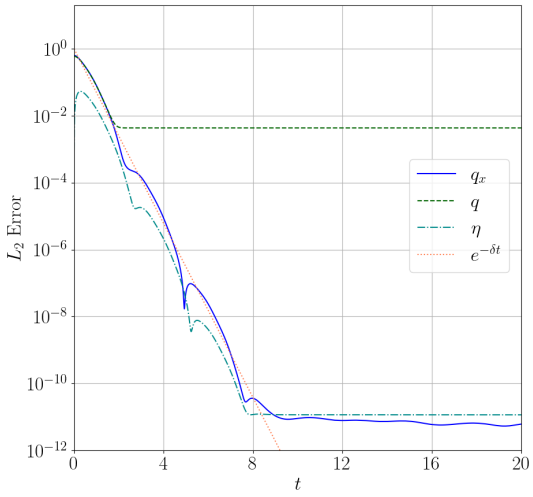

(a) $m = 1$

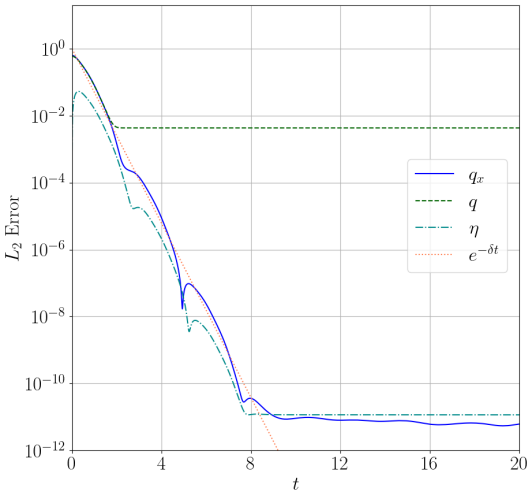

(b) $m = 2$

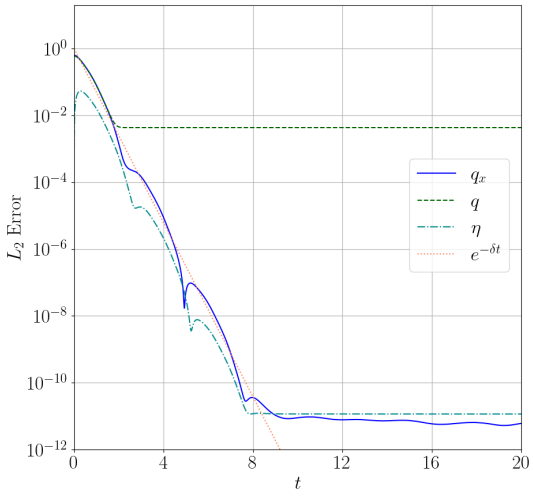

(c) $m = 4$

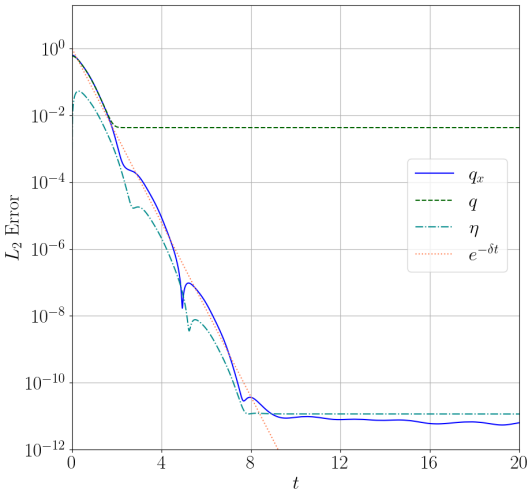

(d) $m = 5$

Figure 5.3: Decay of error in solution for the observer model for the sandbar profile (4.28) in regularised Boussinesq−Whitham model with the time step $2m\Delta t = 0.002$ for the observer model where Δt represent time step for forward model where $m = 1, 2, 4, 5$.

Chapter 6

SIMULTANEOUS RECOVERY OF VELOCITY AND BATHYMETRY

Building upon the concepts from Chapters 4 and 5, we can estimate both the fluid velocity q_x and bottom boundary ζ using surface measurements $\eta(x,t)$. To be precise, we assume we have access to the surface displacement η at each spatial location x and at particular discrete times t_j.

In the next section, we introduce our proposed algorithm for bottom profile reconstruction and then in Section 6.2, we present numerical evidence that the method works as desired.

6.1 The Reconstruction Algorithm

Here is a breakdown of the algorithm steps:

1. **Input and Initial Guess:**

   (a) Assume that the input is true surface displacement data $\eta(x,t)$

   (b) Make a reasonable initial guess for the bottom boundary $\tilde{\zeta}$, which is assumed to be a constant value, i.e., $\tilde{\zeta}(x) = \zeta_c$.

2. **Observer Model Simulation:**

   (a) Pick a small number ϵ such that $\epsilon \ll \mu^2$ where $\mu = 2\pi h/L$ is the shallowness parameter. Based on the error analysis from the previous section, select the observer parameters λ and ν that satisfy the following conditions:

$$\frac{1+\nu}{\lambda} = \epsilon, \quad \text{and} \quad (1+\nu) > \left.\frac{\lambda^2}{4(\frac{\omega(k)^2}{k^2} + \zeta_c \mathcal{P}(k)^2)}\right|_{k=1}.$$

Note the second condition above ensures the error in the observer model decays which we have demonstrated in equation (5.22). The motivation for the first condition is given in the Section 6.3.

(b) Time evolve the observer model

$$\tilde{\eta}_t = \omega^2 \tilde{q} - \mathcal{P}\partial_x\big((\tilde{\eta} + \zeta)\,(\mathcal{P}\tilde{q}_x)\big) - \lambda(\tilde{\eta} - \eta),$$
$$\tilde{q}_t = -\tilde{\eta} - \frac{1}{2}\,(\mathcal{P}\tilde{q}_x)^2 - \nu(\tilde{\eta} - \eta),$$

with these parameters (using any reasonable initial condition; we employ trivial initial conditions) untill the predicted error $e^{-\lambda t/2}$ is sufficiently small.

3. **Data Collection:**

(a) Record the estimated velocity $\tilde{q}_x$ at various points in time (for a large number of time instances say 200).

(b) Simultaneously compute and record the values of η_t (say using finite differences in time) at these points.

4. **Reconstruction Step:** Use the collected data η, η_t and $\tilde{q}_x$ at various times in the reconstruction equation

$$\sum_{j=1}^{M} \left[\mathcal{P}q_x^{(j)}\,\mathcal{P}^2\partial_x^2\left(\mathcal{P}q_x^{(j)}\,\zeta^*\right)\right] = -\sum_{j=1}^{M}\left[\mathcal{P}q_x^{(j)}\,\mathcal{P}\partial_x\left(\eta_t^{(j)} - \omega^2 q^{(j)} + \mathcal{P}\partial_x\left(\eta^{(j)}\,\mathcal{P}q_x^{(j)}\right)\right)\right],$$

to recover the bottom boundary.

Our proposed method reconstruct the underwater bottom profile from surface measurements in a single step. We emphasise: we do not iterate the above steps. This is crucial because iterative approaches, which involve repeated refinement of the estimate, can lead to inaccuracies. Inverting the matrix in left hand of equation (4.22) is ill-conditioned, meaning small errors can snowball during the process. This causes both the estimated water velocity and the reconstructed bottom profile to become increasingly inaccurate.

Remark 6. To ensure accurate reconstruction, the estimated velocity from the observer problem needs to be reliable. This is why choosing the parameters λ and ν in the observer model is critical. The requirements on λ and ν imply that λ cannot be too large. Indeed, λ is typically less than or equal to ϵ. Hence, despite the fact that we were free to choose almost any λ in the observer problem, when attempting to reconstruct the bottom profile, we cannot impose too large a decay rate on the error; the surface displacement must be assimilated slowly into the observer equations so that the resulting velocity is accurate.

Recall Section 4.2.1 presents an example (Figure 4.9) where the bottom boundary reconstruction was shown from erroneous q_x values. In this case, the velocity values $\tilde{q}_x$ used were obtained from an observer problem (with an estimated $\tilde{\zeta}$) using "large" values of λ, violating the conditions discussed above. These large λ values introduced significant errors into the estimated velocity, and therefore resulting in poor reconstruction of the bottom boundary profile.

6.2 Example Reconstruction

In Figures 6.1, 6.2, and 6.3, we present the outcomes of applying our algorithm to recover the bottom profiles (4.24) ,(4.28), and (4.27) respectively. To achieve this, we utilise surface displacement data obtained from simulations of the model shallow-water equations (3.25-3.26) for both the regularised Boussinesq and regularised Boussinesq−Whitham models. In both cases, we set the shallowness parameter $\mu = 1$, corresponding to a fluid aspect ratio of $h/L \sim 0.16$. Subsequently, we employe the solution $\eta(x,t)$ from these shallow-water models to simulate the respective observer model equations (5.1-5.2) for both the models. The details for the numerical simulation of the observer model are the same as those discussed in Section 5.4. The observer parameters for all the examples in this section are $\lambda = 1/100$, $\nu = -1 + \lambda^2$, ensuring a linear decay rate of $\delta = \lambda/2$. These observer parameters satisfy the conditions outlined in the algorithm presented in Section 6.1.

In the process of reconstructing the profiles (4.24) and (4.28), as shown in Figures 6.1 and 6.2, we initiate the shallow-water model with the initial condition defined by equations (3.45-3.46) using a value of $a = 0.0525$. For the observer model, the initial condition for the surface displacement is the same as the one in equation 3.45, but we set the initial velocity potential to zero. Initial guess considered for the bottom boundary for all the examples in this section is $1 + \zeta_{init}(x) = -0.75$, corresponding to $\zeta_c = -0.25$. The relative error E_b, calculated using equation (4.25), in this initial estimate of the bottom boundary is approximately 25% or 24% for the bottom profiles given in equation (4.24) and equation (4.28) respectively. If we calculate in terms of E_p as defined in equation

Regularised Boussinesq model

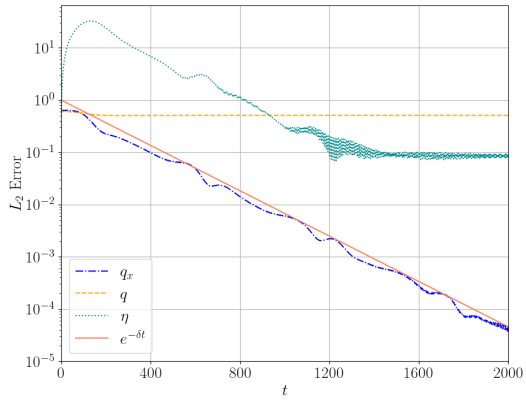

(a) Error decay in observer model with guessed bottom $\lambda = 1/100$, $\nu = -1 + \lambda^2$

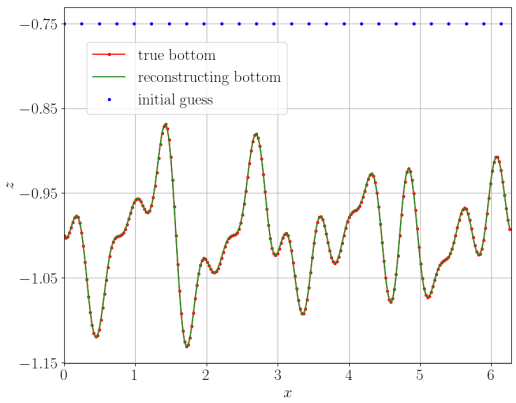

(c) Reconstruction profile

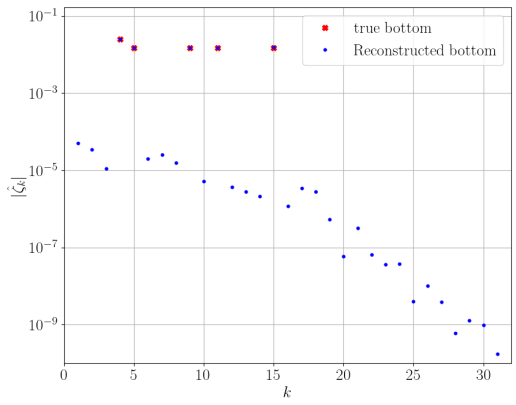

(e) Comparison of Fourier amplitudes $|\hat{\zeta}_k|$ of true profile
and reconstruction profile.

Regularised Boussinesq−Whitham model

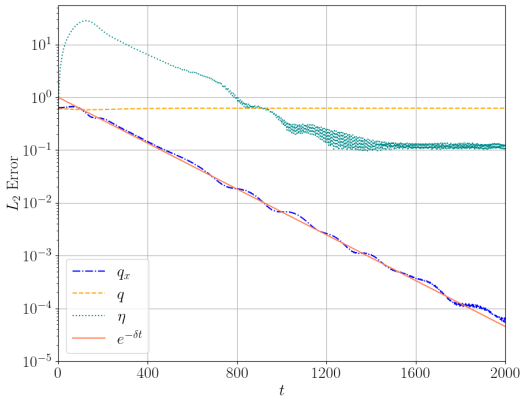

(b) Error decay in observer model with guessed bottom $\lambda = 1/100$, $\nu = -1 + \lambda^2$

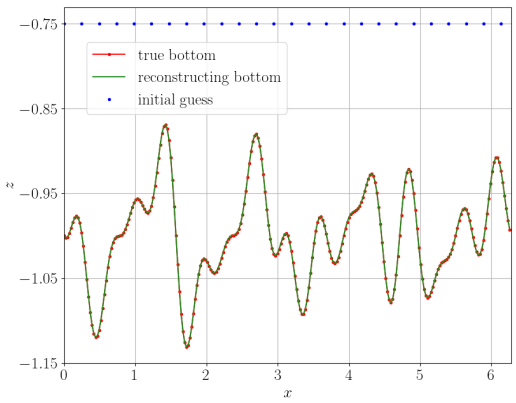

(d) Reconstruction profile

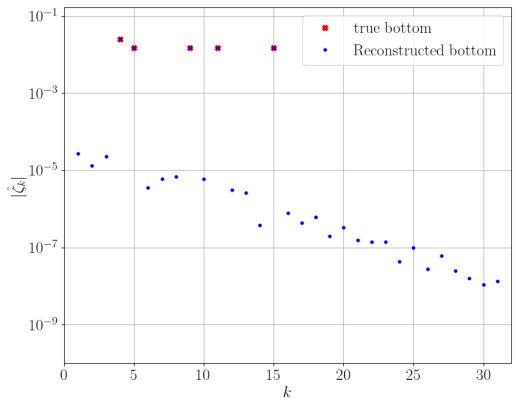

(f) Comparison of Fourier amplitudes $|\hat{\zeta}_k|$ of true profile
and reconstruction profile.

Figure 6.1: Final reconstruction for wavy bottom profile (equation 4.24). Figures on left hand side are for regularised Boussinesq model and Figures on right hand side are for regularised Boussinesq−Whitham model.

Regularised Boussinesq model

Regularised Boussinesq−Whitham model

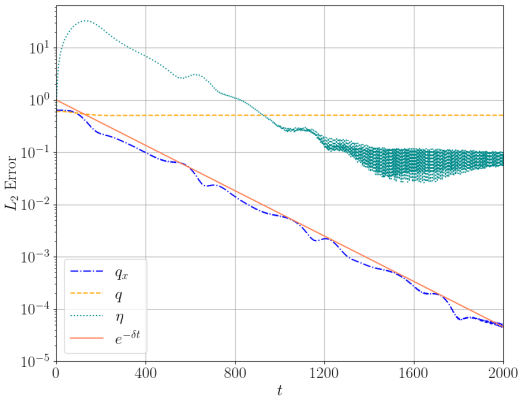

(a) Error decay in observer model with guessed bottom $\lambda = 1/100$, $\nu = -1 + \lambda^2$

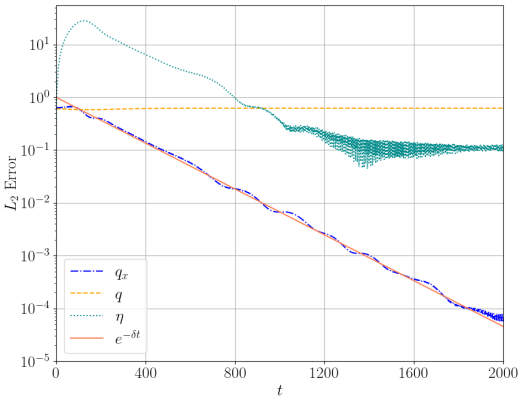

(b) Error decay in observer model with guessed bottom $\lambda = 1/100$, $\nu = -1 + \lambda^2$

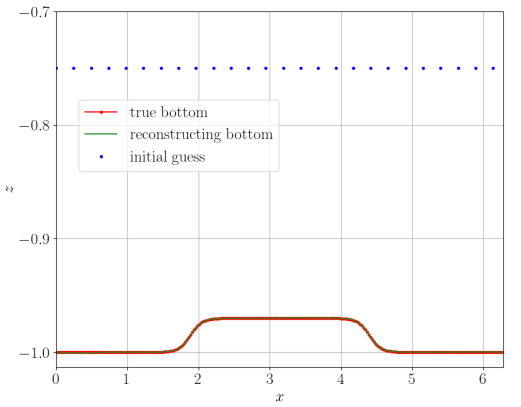

(c) Reconstruction profile

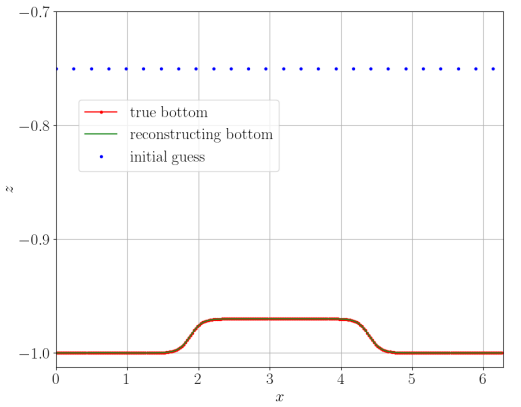

(d) Reconstruction profile

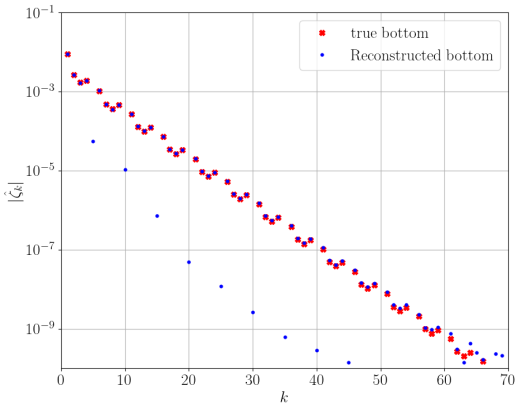

(e) Comparison of Fourier amplitudes $|\hat{\zeta}_k|$ of true profile
and reconstruction profile

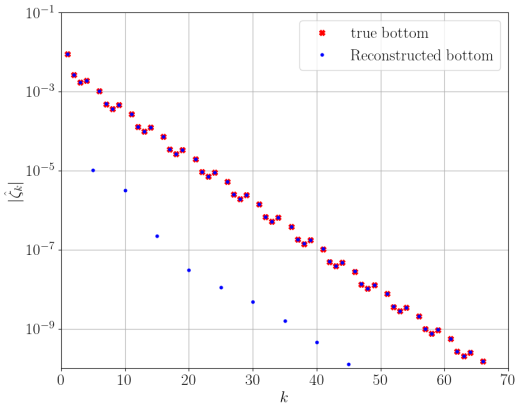

(f) Comparison of Fourier amplitudes $|\hat{\zeta}_k|$ of true profile
and reconstruction profile

Figure 6.2: Final reconstruction for sandbar bottom profile (equation 4.28). Figures on left hand side are for regularised Boussinesq model and Figures on right hand side are for regularised Boussinesq−Whitham model.

Regularised Boussinesq model

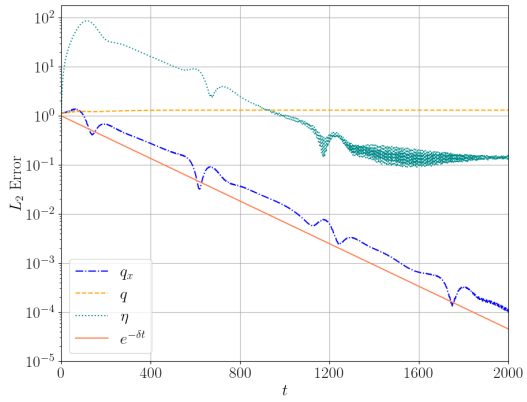

(a) Error decay in observer model with guessed bottom $\lambda = 1/100$, $\nu = -1 + \lambda^2$

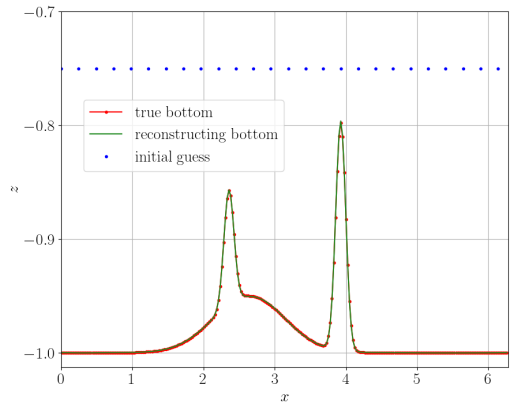

(c) Reconstruction profile

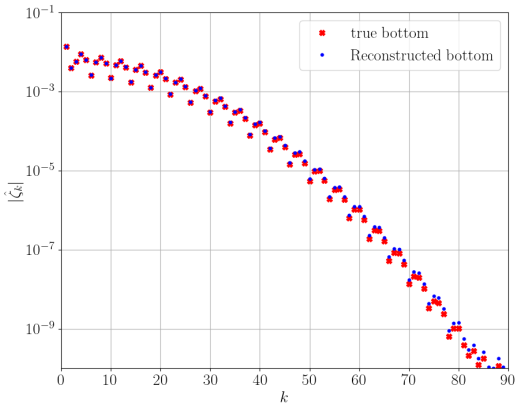

(e) Comparison of Fourier amplitudes $|\hat{\zeta}_k|$ of true profile
and reconstruction profile

Regularised Boussinesq−Whitham model

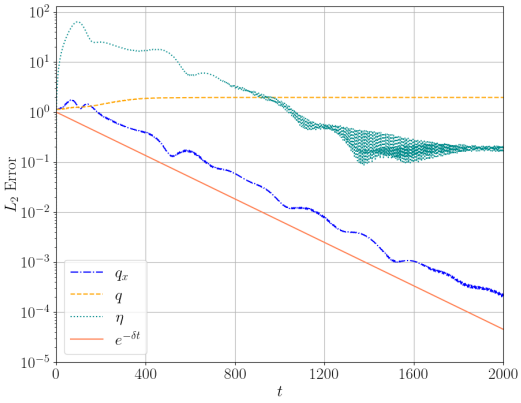

(b) Error decay in observer model with guessed bottom $\lambda = 1/100$, $\nu = -1 + \lambda^2$

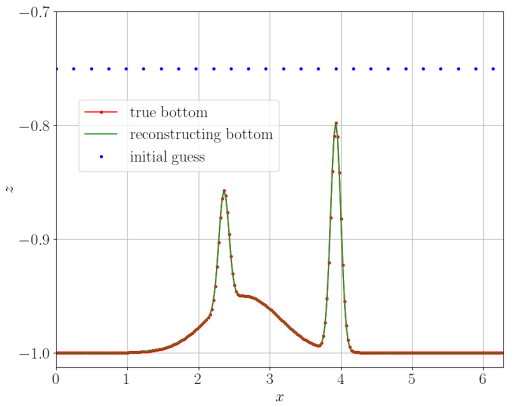

(d) Reconstruction profile

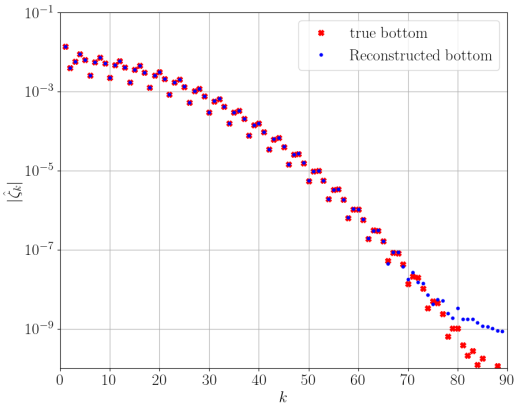

(f) Comparison of Fourier amplitudes $|\hat{\zeta}_k|$ of true profile
and reconstruction profile

Figure 6.3: Final reconstruction for localised feature bottom profile (equation 4.27). Figures on left hand side are for regularised Boussinesq model and Figures on right hand side are for regularised Boussinesq−Whitham model.

(4.25), this translates to an error of over 460% and 1300% for multi-sine wave profile (4.24) and sandbar profile (4.28) respectively. However, despite these seemingly significant errors in the initial bottom-profile estimates, the relative error in the reconstructed bottom boundary values for both profiles converged to around 10^{-4} for regularised Boussinesq and order of 10^{-5} for regularised Boussinesq−Whitham. In terms of E_p, these correspond to highly accurate reconstructions of 99.5% and 99.9% for multi-sine wave profile (4.24) and 99% and 99.8% for sandbar profile (4.28), for regularised Boussinesq and regularised Boussinesq−Whitham model respectively. Interestingly, we observe that the error in the initial guess for the bottom-profile does not significantly impact the recovery process, as long as we could sufficiently reduce the error in the estimated velocity $\tilde{q}_x$. In all our examples, a relative error of 10^{-4} in the estimated velocity (measured using the L^2-norm) proved adequate for achieving accurate results.

In the process of reconstructing the localised bottom feature profile (4.27), as depicted in Figure 6.3, we initiate the shallow-water model with the following initial conditions: $\eta = 0.1\cos(x)$ and $q = 0.1\sin(x)$. For the observer model, we set the initial condition for the surface displacement as $\eta = 0.1\cos(x)$, while initialising the velocity potential to zero. Our initial assumption for the bottom boundary led to a relative error E_b and E_p, as computed using equation (4.25), of approximately 23% and 580% respectively. However, despite the seemingly significant initial error in the bottom boundary estimate for the localised bottom feature profile (4.27), the relative error in the reconstructed bottom boundary values converge to an order of 10^{-4} for both the regularised Boussinesq and regularised Boussinesq−Whitham models. In terms of E_p, these correspond to highly accurate reconstructions of 99.2% and 99.7%, respectively, for this reconstruction.

As depicted in Figures 6.1a, 6.1b, 6.2a, 6.2b, 6.3a, and 6.3b, the error in the velocity consistently follows the expected linear rate of decay. In contrast, the error in the surface displacement stabilises at a level around 10^{-2}. It's worth noting that the surface displacement in the observer model is not a crucial component for the reconstruction algorithm because we can use the data given for surface displacement in the reconstruction algorithm. Consequently, the relatively higher level of error in this aspect is not a cause for concern. The observer model runs until reaching a non-dimensional time of 2000 units.

Turning our attention to Figures 6.1c, 6.1d, 6.2c, 6.2d, 6.3c, and 6.3d, it becomes evident that the reconstructed profile aligns so closely with the true profile that visual differentiation is virtually impossible. In Figures 6.1e, 6.1f, 6.2e, 6.2f, 6.3e, and 6.3f, we observe the absolute values of Fourier modes for the reconstruction profile represented by blue dots, and the Fourier modes for the true bottom profile denoted by red crosses. In cases where red dots are not visible for any value of k, the corresponding Fourier mode for the true profile is effectively zero. This visualisation demonstrates our ability to accurately recover all the high-frequency modes.

In summary, our proposed algorithm effectively reconstructs the bottom boundary for both shallow-water wave models and various bottom profiles, even when initiated from a relatively inaccurate initial estimate.

6.3 Error Estimates

This section tackles the two-step reconstruction method for estimating both fluid velocity q_x and bottom boundary ζ using surface measurements $\eta(x,t)$ and an initial guess for the bottom boundary ζ_c. Our main goal is to motivate the choices made in the reconstruction algorithm, specifically those pertaining to the observer parameters. We delve into error analysis in three parts. First, we derive an error estimate specific to the reconstruction step. Then, we repeat this process for the observer problem. Finally, by combining these individual error estimates, we arrive at suitable choices for the observer model parameters (λ and ν) that ensure the effectiveness of the two-step reconstruction method. The entire discussion here is limited to the linear error equation for velocimetry. However as the numerical results indicate, the reconstruction algorithm works for the full nonlinear case as well.

Error Estimate in Reconstruction Step

Let's denote the true values of surface displacement, surface potential, and bottom boundary as η, q, and ζ respectively. We use $\tilde{\eta}$, $\tilde{q}$, and ζ^* to represent the current estimates of these functions. The errors in these estimates are defined as $\eta^e = \tilde{\eta} - \eta$, (surface displacement error), $q^e = \tilde{q} - q$ (velocity potential error), and $\zeta^e = \zeta^* - \zeta$ (bottom boundary error). According to the discussion in Chapter 4, we could determine ζ if we had the true values for η, η_t, and q. However, in reality, during reconstruction, we typically have the true η and η_t, but only an estimated q (obtained from the observer problem with some amount of error). Therefore, we write down equation (4.11) while incorporating the true values for η and η_t but employing the current estimate ($\tilde{q}$) for velocity potential:

$$(\mathcal{P}\tilde{q}_x)\partial_x^2\mathcal{P}^2(\tilde{\zeta}\mathcal{P}\tilde{q}_x) = -(\mathcal{P}\tilde{q}_x)\partial_x\mathcal{P}\left(\eta_t - \omega^2\tilde{q} + \mathcal{P}\partial_x(\eta\mathcal{P}\tilde{q}_x)\right). \tag{6.1}$$

Here, $\tilde{\zeta}$ represents our best estimate for the bottom boundary, not the true value. Substituting the true dynamical equation (3.25) for η into equation (6.1) and manipulating terms, we arrive at the equation:

$$(\mathcal{P}\tilde{q}_x)\partial_x^2\mathcal{P}^2(\tilde{\zeta}\mathcal{P}\tilde{q}_x) = -(\mathcal{P}\tilde{q}_x)\partial_x\mathcal{P}\left(\omega^2 q - \mathcal{P}\partial_x\left((\eta+\zeta)\mathcal{P}q_x\right) - \omega^2\tilde{q} + \mathcal{P}\partial_x(\eta\mathcal{P}\tilde{q}_x)\right).$$

Adding and subtracting ζ_{true} in the last term on right-hand side, we get

$$\begin{aligned}(\mathcal{P}\tilde{q}_x)\partial_x^2\mathcal{P}^2(\tilde{\zeta}\mathcal{P}\tilde{q}_x) &= -(\mathcal{P}\tilde{q}_x)\partial_x\mathcal{P}\left(\omega^2 q - \mathcal{P}\partial_x\left((\eta+\zeta)\mathcal{P}q_x\right) - \omega^2\tilde{q} + \mathcal{P}\partial_x((\eta+\zeta-\zeta)\mathcal{P}\tilde{q}_x)\right),\\ &= (\mathcal{P}\tilde{q}_x)\partial_x\mathcal{P}\left(\omega^2 q^e + \mathcal{P}\partial_x\left((\eta+\zeta)\mathcal{P}q_x^e\right) + \mathcal{P}\partial_x\left(\zeta\mathcal{P}\tilde{q}_x\right)\right).\end{aligned}$$

Rearranging terms, we have

$$(\mathcal{P}\tilde{q}_x)\,\mathcal{P}^2\partial_x^2\big((\mathcal{P}\tilde{q}_x)\,\zeta^e\big) = (\mathcal{P}\tilde{q}_x)\,\mathcal{P}\partial_x\big(\omega^2 q^e - \mathcal{P}\partial_x\left((\mathcal{P}q_x^e)\,(\eta+\zeta)\right)\big). \tag{6.2}$$

This equation relates the error in our bottom boundary estimate ζ^e to the error in the estimated velocity potential q^e. Notably, the equation's coefficients (and the reconstruction operator B) depend on our current estimate for velocity potential $\tilde{q}$. Here η is the true surface displacement.

However, as discussed in Chapter 5, the error in velocity potential q_e typically does not decay to zero during the observer problem simulation. Only the error in the velocity q_x^e exhibits decay. Therefore, we can treat the right-hand side operator in the equation (6.2) as an operator acting on q_x^e. The next step is to analyse the right-hand side of the equation for both the models.

For regularised Boussinesq model (3.27), we have

$$\begin{aligned}\|\mathcal{P}\partial_x\big(\omega^2 q^e - \mathcal{P}\partial_x\left((\mathcal{P}q_x^e)\,(\eta+\zeta)\right)\big)\|_2 &\le \|\mathcal{P}\partial_x\omega^2 q^e\|_2 + \|\mathcal{P}^2\partial_x^2\big((\eta+\zeta)\,(\mathcal{P}q_x^e)\big)\|_2,\\ &\le \left\|\frac{k^2}{1+\mu^2k^2/2}\left(\frac{1+\mu^2k^2/6}{1+\mu^2k^2/2}\right)k\hat{q}^e\right\|_2\\ &\quad + \left\|\frac{k^2}{(1+\mu^2k^2/2)^2}\mathcal{F}\left[(\eta+\zeta)(Pq_x^e)\right]\right\|_2,\\ &\le \frac{1}{\mu^2}\left(2+\|\eta+\zeta\|_\infty\right)\|q_x^e\|_2.\end{aligned} \tag{6.3}$$

Here, we leverage the definitions of $\mathcal{P}$ and ω^2 in Fourier space from equation (3.27) and the inequality $1/(1+\mu^2k^2/2) \le 1$. Furthermore, we have assumed that the infinite norm of both the true surface displacement η and the true bottom boundary ζ are bounded. This justifies our use of $\|\eta+\zeta\|_\infty \le \infty$.

Similarly, for the regularised Boussinesq−Whitham model (3.30), we have

$$\begin{aligned}\|\mathcal{P}\partial_x\big(\omega^2 q^e - \mathcal{P}\partial_x\left((\mathcal{P}q_x^e)\,(\eta+\zeta)\right)\big)\|_2 &\le \|\mathcal{P}\partial_x\omega^2 q^e\|_2 + \|\mathcal{P}^2\partial_x^2\big((\eta+\zeta)\,(\mathcal{P}q_x^e)\big)\|_2,\\ &\le \|\mathcal{P}\partial_x\omega^2 q^e\|_2 + \|\eta+\zeta\|_\infty\|\mathcal{P}^2\partial_x^2\big((\mathcal{P}q_x^e)\big)\|_2, \quad (6.4)\\ &\le \frac{1}{\mu^2}\|k\tanh(\mu k)\hat{q}^e\|_2 + \frac{1}{\mu^2}\|\eta+\zeta\|_\infty\|q_x^e\|_2,\\ &\le \frac{1}{\mu^2}\left(1+\|\eta+\zeta\|_\infty\right)\|q_x^e\|_2. \quad (6.5)\end{aligned}$$

Similar to the previous case, we use the definitions of $\mathcal{P}$ and ω^2 specific to this model (3.30) and the fact that $\|\tanh(\mu k)\|_2 \leq 1$.

Interestingly, both the models lead to a similar bound with a factor of $1/\mu^2$ in right-hand side. While it might seem like increasing μ would improve reconstruction by reducing the error bound, this is not entirely true. The operator on the left-hand side of the equation (6.2) also have the same factor of $1/\mu^2$. As discussed in Chapter 4, the reconstruction operator can be inverted stably only when eigenvalues are well separated from the origin. However, increasing μ significantly ($\mu \gg 1$) makes the eigenvalues of the left-hand side operator smaller. Therefore, while a larger μ reduces the bound on the right-hand side, it simultaneously makes the left-hand side operator less invertible. This ultimately hinders the reconstruction process. In conclusion, there's a trade-off when choosing the value of μ. Additionally, the solutions to the shallow-water models approximate those of the full water-wave equations only when μ is small.

Fortunately, due to the shallow-water approximation and the no-island condition, we can assume bounded values for $\|\eta\|_\infty$ and $\|\zeta\|_\infty$ (both less than or equal to 1). This limits the quantity $2 + \|\eta + \zeta\|_\infty$ in both cases to a maximum of 4.

The specific form of the operator $\mathcal{P}$ plays a crucial role in achieving boundedness. In the case of the regularised Boussinesq model (3.27), the chosen form of $\mathcal{P}$ allows us to treat the combined operator $\mathcal{P}\partial_x\omega^2$ as bounded on q_x. This highlights the importance of selecting models with compatible forms of ω^2 and $\mathcal{P}$ for effective error analysis and reconstruction. For more details, look at the remark given below.

Our current analysis focuses on error bounds for a single time instance. Extending this analysis to the minimisation problem given by equation (4.21 requires obtaining time-uniform estimates. This translates to ensuring that the observer-model velocity estimate $\tilde{q}_x$ is sufficiently accurate over a period of time, given the true surface displacement η and its time derivative η_t. Here, sufficiently accurate refers to the levels of accuracy required in the examples discussed in Section 4.2.1. While we haven't provided rigorous bounds on this required accuracy, it would likely involve analysing the spectrum of the operator on the left-hand side of equation (6.1) as a function of $\tilde{q}_x$.

Remark. Note that for regularised Boussinesq model (3.27),

$$\omega^2(k) = \frac{1 + \frac{(\mu k)^2}{6}}{1 + \frac{(\mu k)^2}{2}} k^2,$$

is an unbounded operator on q. Since $\mathcal{P}$ in this case is $1/\left(1 + (\mu k)^2/2\right)$ which makes $\mathcal{P}\partial_x\omega^2$ a bounded operator on q_x. This form of $\mathcal{P}$ helps us to make it a bounded operator on q_x. If it was of different form, we might have not been able to get the bound. Also, if we considered a linear dispersion relation that included surface tension effects, we would require even greater smoothing from $\mathcal{P}$. Thus the selection of the model is important in

reconstruction of the bottom boundary problem. The compatibility of the forms of the ω^2 and $\mathcal{P}$ is crucial.

Error Estimate in Velocimetry Step

We recall the initial guess for the bottom boundary is a constant profile ($\tilde{\zeta}(x) = \zeta_c$), leading to an initial error given by $\zeta^e = \zeta_c - \zeta$. We consider the linear shallow-water model satisfied by η and q:

$$\eta_t = \omega^2 q - \mathcal{P}\partial_x\big(\zeta \mathcal{P} q_x\big), \tag{6.6}$$

$$q_t = -\eta. \tag{6.7}$$

The corresponding observer linear equations satisfied by the current estimates $\tilde{\eta}$ and $\tilde{q}$ with the bottom profile $\tilde{\zeta} = \zeta_c$ is given by

$$\tilde{\eta}_t = \omega^2 \tilde{q} - \mathcal{P}\partial_x\big(\zeta_c \mathcal{P} \tilde{q}_x\big) - \lambda(\tilde{\eta} - \eta), \tag{6.8}$$

$$\tilde{q}_t = -\tilde{\eta} - \nu(\tilde{\eta} - \eta). \tag{6.9}$$

We now derive the equation satisfied by the errors in surface displacement and surface velocity. This linear error equation depends on the error in the bottom profile ζ^e:

$$\eta^e_t = \omega^2 q^e - \lambda \eta^e - \mathcal{P}\partial_x\big(\,(\zeta^e + \zeta)\,\mathcal{P}\tilde{q}_x\big) + \mathcal{P}\partial_x\big(\zeta \mathcal{P} q_x\big),$$
$$q^e_t = -(1+\nu)\eta^e.$$

To further simplify the equation, we can add and subtract the term $\mathcal{P}\partial_x\big(\zeta^e \mathcal{P} q_x\big)$ from the first equation, leading to the error equations of the form:

$$\eta^e_t = \omega^2 q^e - \lambda \eta^e - \mathcal{P}\partial_x\big((\mathcal{P} q^e_x)\,(\zeta + \zeta^e)\big) - \mathcal{P}\partial_x\big((\mathcal{P} q_x)\,\zeta^e\big), \tag{6.10}$$

$$q^e_t = -(1+\nu)\eta^e. \tag{6.11}$$

The observer problem aims to minimise the errors η^e and q^e_x. However, achieving complete error elimination is not possible due to the presence of a forcing term $\mathcal{P}\partial_x\big((\mathcal{P} q_x)\zeta^e\big)$ in the error equation (6.10). Note that the strength of the forcing term is directly proportional to the error in ζ.

By taking the time derivative of equation (6.11) and substituting the value of η^e_t from equation (6.10), we obtain a single equation describing the error dynamics:

$$q^e_{tt} + \lambda q^e_t + (1+\nu)\left(\omega^2 q^e - \mathcal{P}\partial_x\big((\mathcal{P} q^e_x)\,(\zeta + \zeta^e)\big)\right) = (1+\nu)\mathcal{P}\partial_x\left((\mathcal{P} q_x)\,\zeta^e\right), \tag{6.12}$$

where $\zeta + \zeta^e = \zeta_c$ is a constant. For the homogeneous part of the equation, we can

consider solutions of the form e^{ikx+pt} where p satisfies the quadratic equation:

$$p^2 + \lambda p + (1+\nu)(\omega(k)^2 + \zeta_c\, k^2 \mathcal{P}(k)^2) = 0.$$

Two solutions of this equation are

$$-\frac{\lambda}{2} \pm \frac{1}{2}\sqrt{\lambda^2 - 4(1+\nu)(\omega^2 + \zeta_c k^2 \mathcal{P}^2)}. \tag{6.13}$$

As established in Theorem 3, achieving an appropriate decay rate for the error necessitates a negative term under the square root in the solution given by equation (6.13) of the homogeneous part of the error equation. This translates to the following condition:

$$(1+\nu) > \left.\frac{\lambda^2}{4(\omega(k)^2 + \zeta_c\, k^2 \mathcal{P}(k)^2)}\right|_{k=1}. \tag{6.14}$$

With this condition satisfied, the solution for p in the homogeneous part can be written as:

$$p^{\pm} = -\lambda/2 \pm i\Omega_k,$$

where Ω_k is a non-zero real number for all non-zero wavenumbers (i.e., $|k| > 0$). Using Duhamel's principle, we can express the general solution for the non-homogeneous error equation (6.12) incorporating the solution for the homogeneous part:

$$\begin{aligned} q^e = e^{-\frac{\lambda}{2}t} \sum_{k=-\infty}^{\infty}{}' e^{ikx} \left(e^{i\Omega_k t}\alpha_k + e^{-i\Omega_k t}\beta_k\right) + e^{-\lambda t}\alpha_0 + \beta_0 \\ + \int_0^t (1+\nu) e^{-\frac{\lambda}{2}(t-s)} \left(\sum_{k=-\infty}^{\infty}{}' e^{ikx} \frac{\sin(\Omega_k(t-s))}{\Omega_k} \mathcal{F}_k \left[\mathcal{P}\partial_x\big((\mathcal{P}q_x)\,\zeta^e\big)\right]_k \right) ds. \end{aligned}$$

Here, the values of α_k, β_k depend on the Fourier coefficients of the initial data, and the prime on the summation indicates that the term with $k = 0$ is excluded.

We recall that the error in q is influenced by the forcing term, which is proportional to ζ^e (the error in the bottom boundary estimate). Since we are interested in q^e_x, we can estimate it by taking the derivative in x of the above equation and then estimating the 2-norm:

$$\|q^e_x\|_2 \le e^{-\frac{\lambda}{2}t}(\|\alpha_x\|_2 + \|\beta_x\|_2) + \left(\sup_t \|\mathcal{P}\partial_x^2\big((\mathcal{P}q_x)\,\zeta^e\big)\|_2\right) \int_0^t (1+\nu) e^{-\frac{\lambda}{2}(t-s)} ds.$$

Employing a version of Zadiraka's Theorem 5 with $c = 0$, we obtain the following expression for the long-time error on q_x:

$$\|q^e_x\|_2 \sim 2\frac{1+\nu}{\lambda} \sup_t \|\mathcal{P}\partial_x^2\big((\mathcal{P}q_x)\,\zeta^e\big)\|_2. \tag{6.15}$$

We can analyse the long-time behaviour based on the specific model. If $q_x \in L^2$ for all times, then $\sup_t \|\mathcal{P}q_x\|_\infty$ is bounded due to the regularising nature of the operator $\mathcal{P}$. As $t \to \infty$, we get:

$$\|q_x^e\|_2 \leq \frac{4(1+\nu)}{\lambda\mu^2}\|\zeta^e\|_2 \sup_t \|\mathcal{P}q_x\|_\infty. \tag{6.16}$$

For regularised Boussinesq−Whitham model, we can not do exactly the same way because $\mathcal{P}\partial_x$ is not smooth in this case. However, if we impose additional regularity on ζ^e, the long-time error bound in q_x is given by

$$\|q_x^e\|_2 \sim 2\frac{1+\nu}{\mu\lambda} \sup_t \|\partial_x\big((\mathcal{P}q_x)\,\zeta^e\big)\|_2. \tag{6.17}$$

Both the models exhibit similar scaling with respect to the observer parameters λ and ν. Intuitively, increasing λ might seem beneficial for reducing the long-term error in q_x^e. However, we must consider the relationship between λ and ν given in equation (6.14). This equation indicates that $1+\nu$ is directly proportional to λ . From the expressions above in equations (6.16-6.17), the error in q_x^e is also directly proportional to $1+\nu$. Therefore, while increasing λ might lead to a lower error bound initially, it also increases the value of ν, which counteracts the initial gain and ultimately impacts the error q_x^e. To ensure a sufficiently small $\|q_x^e\|$, we need to minimise the value of $(1+\nu)/\lambda$.

The long-time behaviour of the q_x^e error has been estimated for the linear equations (6.10-6.11). These estimates depend on the regularity of the initial data and the regularity of the error term ζ^e.

We anticipate a similar error estimate to hold for the nonlinear equations (5.1-5.2) as long as λ is sufficiently large. This ensures it can overcome any potential growth in the solution. The nonlinear terms in these equations are Lipschitz functions for η and q_x in L^2. Our numerical solutions further support this notion by demonstrating the decay rate of the error in q_x for nonlinear models as well.

Combining both the estimates

In order to reconstruct the bottom boundary, it is crucial to improve the error estimates of the final bottom-profile. Here, we denote the initial guess for the bottom-profile by ζ_c, therefore the initial error in bottom profile is given by $\zeta_{init}^e = \zeta_c - \zeta$ and the the final reconstructed profile is denoted by ζ^* and thus the final error is calculated as $\zeta_{final}^e = \zeta^* - \zeta$. Our objective is to ensure that final error ζ_{final}^e smaller than the initial error ζ_{init}^e. For the regularised Boussinesq model: using equations (6.2) and (6.3), we have

$$\|(\mathcal{P}\tilde{q}_x)\partial_x^2\mathcal{P}^2(\tilde{\zeta}\mathcal{P}\tilde{q}_x)\|_2 \leq \frac{1}{\mu^2}\left(2+\|\eta+\zeta\|_\infty\right)\|\mathcal{P}\tilde{q}_x\|_\infty\|q_x^e\|_2.$$

Now using equation (6.16) and the fact that $\|2+\eta+\zeta\|_\infty \leq 4$, we get

$$\|(\mathcal{P}\tilde{q}_x)\partial_x^2\mathcal{P}^2(\tilde{\zeta}\mathcal{P}\tilde{q}_x)\|_2 \leq \frac{16}{\mu^4}\frac{(1+\nu)}{\lambda}\|\zeta^e_{init}\|_2\,\|\mathcal{P}\tilde{q}_x\|_\infty \sup_t \|\mathcal{P}q_x\|_\infty. \tag{6.18}$$

Due to our non-dimensional scaling and the the type of initial conditions we are using for our simulations, $|\tilde{q}_x|$ and $|q_x|$ are typically less than 1. Thus, the inequality (6.18) shows that to ensure the small error in the final estimated bottom profile, we need to make sure that the coefficient of $\|\zeta^e_{init}\|_2$ is as small as possible and we have to choose λ and ν in such a way that we can minimise the term $(1+\nu)/\lambda$.

While the proof for the regularised Boussinesq model is straightforward, the regularised Boussinesq−Whitham model presents a challenge. As discussed earlier, the technical difficulty lies in the term $\mathcal{P}\partial_x$, which is only bounded and not smooth. So we cannot obtain the same estimate without requiring additional regularity on the true bottom profile ζ. Nevertheless, our simulations show that a similar estimates holds for regularised Boussinesq−Whitham as well.

Chapter 7

CONCLUSIONS

This work establishes the feasibility of simultaneously recovering the bottom boundary profile and velocities in the context of dispersive shallow-water models using solely surface wave elevation measurements (η). Notably, the aspect ratios (h/L) for which accurate bathymetric reconstruction is achieved are an order of magnitude larger compared to prior studies [58]. This is a significant improvement over the method of [58].

Furthermore, the research demonstrates the efficacy of velocimetry, the estimation of velocities, in Boussinesq-type shallow-water models. Accurate velocity estimates are achievable with a known bottom boundary profile. Interestingly, the observer framework employed here provides reasonable velocity estimates even when the bottom profile is unknown.

It is crucial to note that the ability to recover both the bottom boundary and velocity is not contingent upon a specific shallow-water model. The results suggest the possibility of extending this approach to a broader class of models based on the properties of the pseudo-differential operators ω^2 and $\mathcal{P}$. While our work demonstrates promising results, ocean depth measurement remains a sensitive process. Carefully selecting parameters within the observer framework is critical.

Note that all our simulations were conducted for a single spatial dimension. The shallow-water model can easily be generalised to two spatial dimensions and so does then the whole approach put forward in this thesis. Additionally, the time-reversibility of the model allows for back and forth nudging technique [8, 7] with limited data records of $\eta(x,t)$. However, adapting the reconstruction algorithm for real-world applications involving non-periodic data poses a challenge. Non-periodic boundaries introduce mass flux across the lateral boundaries, requiring reformulation of the associated DNO and the Hamiltonian framework. Addressing these issues to handle non-periodic data remains an important area for future work.

We conclude by emphasising the crucial, yet implicit, role of model selection in the entire reconstruction process. While the regularised Boussinesq model offered advantages for estimating key quantities, it did not possess the rapid decay of eigenvalues of the linear

operator in equation 4.22. The regularised Boussinesq−Whitham model, on the other hand, had this rapid decay, but presented challenges in verifying certain estimates and necessitated stricter assumptions about the bottom-profile regularity.

The reduction to the shallow-water regime played a significant role in simplifying the design of the observer and reconstruction algorithm. Ultimately, the choice of model hinges on our understanding and interpretation of the data, coupled with our assumptions regarding the true bottom boundary profile. However, as noted in [43], for a shallow-water model to accurately represent the full water-wave equations, these two factors might not be entirely independent.

Our work highlights the interdependence between the mathematical properties of these equations, particularly the interplay between the dispersion relation (ω^2) and the regularisation term ($\mathcal{P}$). This interdependence suggests that certain models might be inherently better suited for accurate reconstruction compared to others.

We hope that the combination of clear estimates and the numerical simulations presented in this thesis have provided the valuable insights into the complexities of this challenging inverse problem.

Bibliography

[1] M. J. Ablowitz, A. S. Fokas, and Z. H. Musslimani. On a new non-local formulation of water waves. *Journal of Fluid Mechanics*, 562:313–343, 2006.

[2] M.J. Ablowitz. *Nonlinear dispersive waves: asymptotic analysis and solitons*, volume 47. Cambridge University Press, 2011.

[3] P. Aceves-Sánchez, A.A. Minzoni, and P. Panayotaros. Numerical study of a nonlocal model for water-waves with variable depth. *Wave Motion*, 50(1):80–93, 2013.

[4] A. Apte, D. Auroux, and M. Ramaswamy. Variational data assimilation for discrete Burgers equation. *Electronic Journal of Differential Equations (EJDE)[electronic only]*, 19:15–30, 2010.

[5] A. Apte, D. Auroux, and M. Ramaswamy. Observers for compressible Navier–Stokes equation. *SIAM Journal on Control and Optimization*, 56(2):1081–1104, 2018.

[6] D. Auroux. Several data assimilation methods for geophysical problems. *Indian Journal of Pure and Applied Mathematics*, 37:41–58, 2006.

[7] D. Auroux and J. Blum. Back and forth nudging algorithm for data assimilation problems. *Comptes Rendus Mathematique*, 340(12):873–878, 2005.

[8] D. Auroux and J. Blum. A nudging-based data assimilation method for oceanographic problems: the Back and Forth Nudging (BFN) algorithm. *Nonlinear Processes in Geophysics*, 15:305–319, 2008.

[9] D. Auroux and S. Bonnabel. Symmetry-based observers for some water-tank problems. *IEEE Transactions on Automatic Control*, 56(5):1046–1058, 2011.

[10] J.J. Becker, D.T. Sandwell, W.H.F. Smith, J. Braud, B. Binder, J.L. Depner, D. Fabre, J. Factor, S. Ingalls, S.H. Kim, et al. Global bathymetry and elevation data at 30 arc seconds resolution: Srtm30_plus. *Marine Geodesy*, 32(4):355–371, 2009.

[11] T. B. Benjamin and P. J. Olver. Hamiltonian structure, symmetries and conservation laws for water waves. *Journal of Fluid Mechanics*, 125:137–185, 1982.

[12] J. P. Boyd. *Chebyshev and Fourier spectral methods*. Dover Publications Inc., Mineola, NY, 2001.

[13] J. Brown. *The ocean basins: Their structure and evolution*. Elsevier, 2013.

[14] R. Camassa, D. D. Holm, and C. D. Levermore. Long-time effects of bottom topography in shallow water. *Physica D: Nonlinear Phenomena*, 98(2-4):258–286, 1996.

[15] J.D. Carter, E. Dinvay, and H. Kalisch. Fully dispersive boussinesq models with uneven bathymetry. *Journal of Engineering Mathematics*, 127:1–14, 2021.

[16] B. Chapron, F. Collard, and F. Ardhuin. Direct measurements of ocean surface velocity from space: Interpretation and validation. *Journal of Geophysical Research: Oceans*, 110(C7), 2005.

[17] I. M. Cohen and P. K. Kundu. *Fluid Mechanics*. Elsevier, 2004.

[18] R. Coifman and Y. Meyer. Nonlinear harmonic analysis and analytic dependence. *Pseudo-Differential Operators and Applications*, 43(71-78):12, 1985.

[19] R. R. Coifman and Y. Meyer. Nonlinear harmonic analysis and analytic dependence. pages 71–78. American Mathematical Society Providence, RJ, 1985.

[20] M. D. Collins and W. A. Kuperman. Inverse problems in ocean acoustics. *Inverse Problems*, 10:1023–1040, 1994.

[21] W. Craig and C. Sulem. Numerical simulation of gravity waves. *Journal of Computational Physics*, 108:73–83, 1993.

[22] A.G. Davies and A.D. Heathershaw. Surface-wave propagation over sinusoidally varying topography. *Journal of Fluid Mechanics*, 144:419–443, 1984.

[23] R. G. Dean and R. A. Dalrymple. *Water wave mechanics for engineers and scientists*. World Cientific Publishing Company, Singapore, 2010.

[24] P. J. Dellar and R. Salmon. Shallow water equations with a complete coriolis force and topography. *Physics of fluids*, 17(10):106601, 2005.

[25] E. Dinvay. On well-posedness of a dispersive system of the Whitham–Boussinesq type. *Applied Mathematics Letters*, 88:13–20, 2019.

[26] E. Dinvay, D. Dutykh, and H. Kalisch. A comparative study of bi-directional Whitham systems. *Applied Numerical Mathematics*, 141:248–262, 2019.

[27] L. Evans. *Partial differential equations*. American Mathematical Society, Providence, RI, 1998.

[28] L. C. Evans. Partial differential equations. *Graduate studies in mathematics*, 19(2), 1998.

[29] M. A. Fontelos, R. Lecaros, J.C. López, and J. H. Ortega. Bottom detection through surface measurements on water waves. *SIAM Journal on Control and Optimization*, 55(6):3890–3907, 2017.

[30] L. Gorman, A. Morang, and R. Larson. Monitoring the coastal environment; part iv: mapping, shoreline changes, and bathymetric analysis. *Journal of Coastal Research*, pages 61–92, 1998.

[31] S. Grilli. Depth inversion in shallow water based on nonlinear properties of shoaling periodic waves. *Coastal Engineering*, 35:185–209, 1998.

[32] J. Grue. Nonlinear water waves at a submerged obstacle or bottom topography. *Journal of Fluid Mechanics*, 244:455–476, 1992.

[33] P. Guyenne and D. P. Nicholls. A high-order spectral method for nonlinear water waves over moving bottom topography. *SIAM Journal on Scientific Computing*, 30:81–101, 2007/08.

[34] C. Heining and M. Sellier. Flow domain identification in three-dimensional creeping flows. *Physics of Fluids*, 29(1):012107, 2017.

[35] B. Hu and D. P. Nicholls. The domain of analyticity of Dirichlet-Neumann operators. *Proceedings of the Royal Society of Edinburgh Section A: Mathematics*, 140:367–389, 2010.

[36] V. M. Hur and A. K. Pandey. Modulational instability in a full-dispersion shallow water model. *Studies in Applied Mathematics*, 142(1):3–47, 2019.

[37] J. A. Johannessen, B. Chapron, F. Collard, V. Kudryavtsev, A. Mouche, D. Akimov, and K-F Dagestad. Direct ocean surface velocity measurements from space: Improved quantitative interpretation of envisat asar observations. *Geophysical Research Letters*, 35(22), 2008.

[38] S. Kar and A. Guha. Ocean bathymetry reconstruction from surface data using hydraulics theory. *Physics of Fluids*, 30(12):121701, 2018.

[39] T. Kato. *Perturbation theory for linear operators*, volume 132. Springer Science & Business Media, 2013.

[40] J. A. Koslow. Seamounts and the ecology of deep-sea fisheries: The firm-bodied fishes that feed around seamounts are biologically distinct from their deepwater

neighbors—and may be especially vulnerable to overfishing. *American Scientist*, 85(2):168–176, 1997.

[41] E. Kunze and S. G. L. Smith. The role of small-scale topography in turbulent mixing of the global ocean. *Oceanography*, 17(1):55–64, 2004.

[42] D. Lannes. Well-posedness of the water-wave equations. *Journal of the American Mathematical Society*, 18:605–654, 2005.

[43] D. Lannes. *The water waves problem: mathematical analysis and asymptotics*, volume 188. American Mathematical Society, 2013.

[44] D. Luenberger. An introduction to observers. *IEEE Transactions on Automatic Control*, 16(6):596–602, 1971.

[45] N. Mori, T. Takahashi, T. Yasuda, and H. Yanagisawa. Survey of 2011 tohoku earthquake tsunami inundation and run-up. *Geophysical Research Letters*, 38(7), 2011.

[46] D. P. Nicholls. Traveling water waves: spectral continuation methods with parallel implementation. *Journal of Computational Physics*, 143:224–240, 1998.

[47] D. P. Nicholls and M. Taber. Joint analyticity and analytic continuation of Dirichlet-Neumann operators on doubly perturbed domains. *Journal of Mathematical Fluid Mechanics*, 10:238–271, 2008.

[48] D. P. Nicholls and M. Taber. Detection of ocean bathymetry from surface wave measurements. *European Journal of Mechanics-B/Fluids*, 28(2):224–233, 2009.

[49] P. J. Olver. Conservation laws of free boundary problems and the classification of conservation laws for water waves. *Transactions of the American Mathematical Society*, 277:353–380, 1983.

[50] C. Piotrowski and J. Dugan. Accuracy of bathymetry and current retrievals from air-borne optical time-series imaging of shoaling waves. *IEEE Transactions on Geoscience and Remote Sensing*, 40:2606–2618, 2002.

[51] W. H. F. Smith and D. T. Sandwell. Bathymetric prediction from dense satellite altimetry and sparse shipboard bathymetry. *Journal of Geophysical Research: Solid Earth*, 99(B11):21803–21824, 1994.

[52] W. H.F. Smith and D. T. Sandwell. Conventional bathymetry, bathymetry from space, and geodetic altimetry. *Oceanography - The Oceanography Society*, 17(1):8–23, 2004.

[53] E. D. Sontag. *Mathematical control theory: deterministic finite dimensional systems*, volume 6. Springer Science & Business Media, 2013.

[54] J. J. Stoker. *Water waves: The mathematical theory with applications*, volume 36. John Wiley & Sons, 1992.

[55] M. I. Taroudakis and G. Makrakis. *Inverse Problems in Underwater Acoustics*. Springer-Verlag, New York, 2001.

[56] L. N. Trefethen. *Spectral methods in MATLAB*. Society for Industrial and Applied Mathematics (SIAM), Philadelphia, PA, 2000.

[57] V. Vasan. *Some boundary-value problems for water waves*. University of Washington, 2012.

[58] V. Vasan and B. Deconinck. The inverse water wave problem of bathymetry detection. *Journal of Fluid Mechanics*, 714:562–590, 2013.

[59] A. B. Watts, B. Tozer, H. Harper, B. Boston, D. J. Shillington, and R. Dunn. Evaluation of shipboard and satellite-derived bathymetry and gravity data over seamounts in the northwest pacific ocean. *Journal of Geophysical Research: Solid Earth*, 125(10):e2020JB020396, 2020.

[60] S. Wu. Global wellposedness of the 3-D full water wave problem. *Inventiones mathematicae*, 184:125–220, 2011.

[61] C. Wunsch. Inverse problems, inverse methods, and inverse models. 2019.

[62] S. B. Yoon. Propagation of distant tsunamis over slowly varying topography. *Journal of Geophysical Research: Oceans*, 107(C10):4–1, 2002.

[63] K.V. Zadiraka. Issledoavanie nereguljarnogo vozmuscennyh differencial'nyh uravenii. *Voprosy teorii i istorii differencial'nyh uravenii, Kiev*, 1968.

[64] V. E. Zakharov. Stability of periodic waves of finite amplitude on the surface of a deep fluid. *Zhurnal Prikladnoi Mekhaniki i Tekhnicheskoi Fiziki*, 8:86–94, 1968.